Design, manufacturing, and experimental analysis of additively fabricated metamaterials with a pantographic substructure

vorgelegt von

M. Sc.

Gregor Ganzosch

an der Fakultät V – Verkehrs- und Maschinensysteme

der Technischen Universität Berlin

zur Erlangung des akademischen Grades

Doktor der Ingenieurwissenschaften

– Dr.-Ing. –

genehmigte Dissertation

Promotionsausschuss:

Vorsitzender: Prof. Dr.-Ing. Utz von Wagner

Gutachter: Prof. Dr. rer. nat. Wolfgang H. Müller

Gutachter: Prof. Dr.-Ing. habil. Dr. h. c. Holm Altenbach

Tag der wissenschaftlichen Aussprache: 23. Dezember 2021

Berlin 2022

– dla kochanej rodzinki –

Abstract

Due to the rapid developments in the field of additive manufacturing technologies in the recent past, the cost-effectively manufacturing of complex, small scaled components became possible. These demanding components mostly consist of multiple substructures on the micro- or macroscale. Based on the inner substructure (microscale), a special desired global deformation behavior can be triggered (macroscale). These structures are often referred to as mechanical metamaterials in literature. A very promising example of such a metamaterial is the so-called pantographic structure, which consists of two orthogonal arrays of beams connected by internal cylinders (pivots). In order to manufacture a metamaterial with a pantographic substructure, a parametrized, computer-aided design model was developed and used to produce differently sized specimens made of at least four different materials (Polylactide, Epoxy resin, Polyamide, Aluminum) by means of four different additive manufacturing technologies (Fused Deposition Modeling, Stereolithography, Selective Laser Melting, Direct Metal Laser Sintering). These specimens have been investigated experimentally in quasi-static extension, shearing, and torsion tests, evaluated by digital image correlation. All pantographics show a non-linear, resilient deformation behavior. By means of digital image correlation three-dimensional deformations (such as the buckling in shearing tests) could be captured and determined quantitatively. Based on these measurements, new (higher) material parameters have been determined by means of an inverse analysis and a higher gradient model has been evaluated.

Zusammenfassung

Durch den rapiden Entwicklungsfortschritt der letzten Jahre im Bereich der additiven Fertigung ist es möglich geworden, die kompliziertesten Bauteilstrukturen mit kleinsten Geometrien kosteneffizient und in ausreichend guter Qualität herzustellen. Diese höchst anspruchsvoll zu fertigenden Bauteile bestehen meist aus mehreren Substrukturen auf der Mikro- oder Makroskala. Basierend auf der inneren Geometrie (Mikroskala), kann ein speziell gewünschtes, globales Verformungsverhalten eingestellt werden (Makroskala). Diese Strukturen werden in der Literatur meist als mechanische Metamaterialien bezeichnet. Ein vielversprechendes Beispiel eines solchen Metamaterials ist die so genannte pantograpische Struktur, die aus zwei Ebenen mit jeweils senkrecht zueinander periodisch angeordneten Balken besteht, die durch Zylinder miteinander verbunden sind. Um dieses Metamaterial mit pantographischer Substruktur herzustellen, wurde ein parametrisiertes, rechnerunterstütztes Model entwickelt, mit dessen Hilfe in vier unterschiedlichen additiven Fertigungsverfahren (Schmelzschichtung, Stereolithographie, Selektives Laserschmelzen, Direktes Metall-Lasersintern) Proben unterschiedlichster Größe aus mindestens vier verschiedenen Materialien (Polymilchsäure, Epoxid-Harz, Polyamid, Aluminiumlegierung) hergestellt wurden. Diese Proben wurden experimentell in quasi-statischen Zug-, Scher- und Torsionsversuchen untersucht und mittels digitaler Bildkorrelation evaluiert. Alle Pantographen zeigen ein nicht-lineares, widerstandsfähiges Verformungsverhalten. Mit Hilfe der digitalen Bildkorrelation konnten auch drei dimensionale Verformungen (wie beispielsweise das Beulen in Scherversuchen) aufgenommen und quantitativ bestimmt werden. Basierend auf diesen Messungen wurden durch Anwendung einer inversen Analyse neue (höhere) Materialparameter bestimmt und ein höheres Gradientenmodell validiert.

List of publications and copyright notice

This cumulative dissertation is composed of four publications:

[1]: **Gregor Ganzosch, Francesco dell'Isola, Emilio Turco, Tomasz Lekszycki, and Wolfgang H. Müller: Shearing tests applied to pantographic structures. *Acta Polytechnica CTU Proceedings*, 7:1–6, 2017.** Status: *"published"* under the Creative Commons License Attribution 4.0 International (CC BY 4.0) - `https://creativecommons.org/licenses/by/4.0/`; Users are allowed to read, download, copy, distribute, print, search, or link to the full texts of the articles in this journal without asking for prior permission from the publisher or the author (`https://ojs.cvut.cz/ojs/index.php/APP/about/editorialPolicies`).

DOI: https://doi.org/10.14311/APP.2017.7.0001

[2]: **Gregor Ganzosch, Klaus Hoschke, Tomasz Lekszycki, Ivan Giorgio, Emilio Turco, and Wolfgang H. Müller. 3D-measurements of 3D-deformations of pantographic structures. *Technische Mechanik,* 38(3):233–245, 2018.** Status: *"published"* under the Creative Commons License Attribution-ShareAlike 4.0 International (CC BY-SA 4.0) - `https://creativecommons.org/licenses/by-sa/4.0/`; The authors hold and retain the copyright of their papers (`http://journals.ub.uni-magdeburg.de/ubjournals/index.php/techmech/about`).

DOI: https://doi.org/10.24352/UB.OVGU-2018-031

[3]: **Emilio Barchiesi, Gregor Ganzosch, Christian Liebold, Luca Placidi, Roman Grygoruk, and Wolfgang H. Müller. Out-of-plane buckling of pantographic fabrics in displacement-controlled shear tests: experimental results and model validation. *Continuum Mechanics and Thermodynamics,* 31(1):33–45, 2019.** Status: *"published"* and reprinted by permission from Springer Nature Customer Service Centre GmbH (Copyright Clearance Center, License Number 4914151342018): Springer Nature, Continuum Mechanics and Thermodynamics, Out-of-plane buckling of pantographic fabrics in displacement-controlled shear tests: experimental results and model validation, Emilio Barchiesi, Gregor Ganzosch, Christian Liebold, Luca Placidi, Roman Grygoruk, and Wolfgang H. Müller, 2019.

DOI: https://doi.org/10.1007/s00161-018-0626-x

[4]: **Gregor Ganzosch, Christina Völlmecke, Emilio Barchiesi, and Wolfgang H. Müller. The making and testing of FDM and SLA printed pantographic**

sheets. ***Elasticity and Anelasticity,*** **Moscow State Univ. Publ., 57—66, 2021.** Status: *"published"*. The authors own their preprints (`https://www.elibrary.ru/item.asp?id=47390305&pff=1`).

ISBN: 978-5-19-011626-7

Contents

1 Introduction and motivation

With the advances in rapid prototyping technologies the design and manufacturing of complex structures made of promising materials became possible in the recent past. In fact the small scale fabrication of taylor-made structures became more affordable than ever [5]. Customized structures, whose peculiar and very exotic (mechanical) properties, *e.g.*, high stiffness or large deformation, depend strongly on the microscopic constituents and therefore on the inner substructure [6, 7, 8, 9], are known as architectured materials or metamaterials [10, 11, 12, 13]. A very promising example of such a fabricated metamaterial is the Pantographic Structure (PS) [6, 5, 14, 15]. This structure can be described as a metamaterial with a repeated substructure consisting of different inner parameters, see Fig. 1: two orthogonal arrays of beams are connected by internal cylinders, so-called pivots. By varying those inner parameters on the microscale, a special wanted mechanical response of the metamaterial on the macroscale can be adjusted [16, 17, 18, 19], *e.g.*, by triggering large deformations or auxetic deformation behaviors [20, 21]. Regularly, such extraordinary structures are manufactured and tested for special technical applications. The theoretical description and modeling of such a structure is mostly considered after designing and testing prototypes. But for PSs quite the

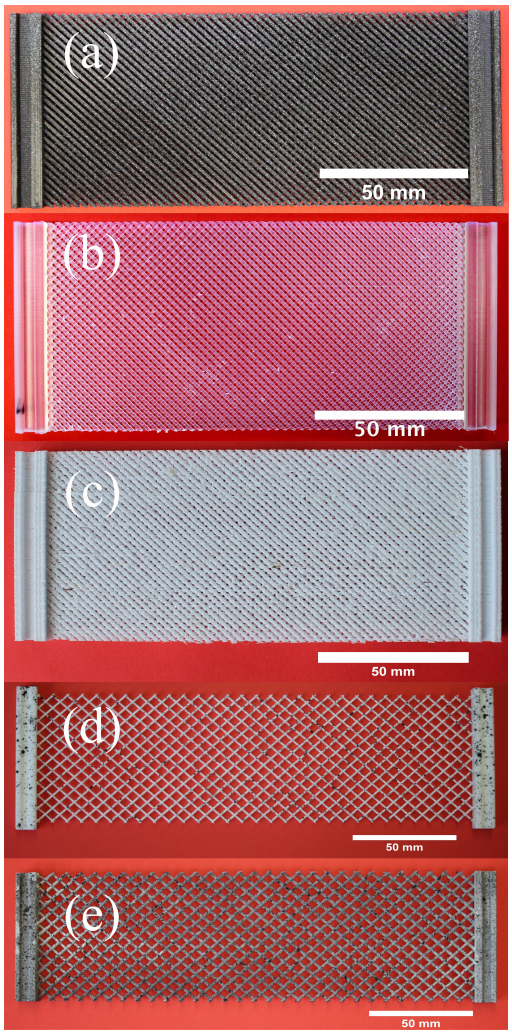

Figure 1: Examples of metamaterials with differently sized pantographic (sub)structures made of polylactide (a), epoxy resin (b), polyethylenterephthalat+glycol (c), polyamide (d), and aluminum (e).

opposite happened. Based on the analysis of underlying equations and by formulating constitutive laws, a structure showing promising properties like large elastic deformation and low dissipation loss had to be invented and manufactured [22, 23, 7, 24, 15, 5].

Furthermore, in order to apply such a custom-made metamaterial in a particular technical application, a forecast of its deformation characteristic and mechanical performance can be crucial in the field of engineering. An opportunity to achieve such a prediction is to make use of the Finite Element Method (FEM). Typically, in a classical numerical simulation, which is based on the Cauchy-Boltzmann continuum, a very fine mesh is required. This is also the case for a PS with its inner substructure on the microscale. Unfortunately, this results in very high computational costs, due to the high number of unknowns. However, by means of a higher gradient theory, which is a very active part in the research field of generalized continuum theories, and a homogenization of such a discrete structure, an equivalent Cauchy-Boltzmann continuum is obtained and can overcome these limitations [6, 25, 16]. The research of such non standard mathematical models, which "smear" out a discrete field, has been ongoing for at least over one hundred years [26, 27]. In the specific case of PSs the theoretical background came up more than twenty years ago [28, 29] describing a PS as a second gradient continua [30, 31, 32].

However, new material parameters appear in the novel constitutive laws. These have to be interpreted and determined quantitatively – this is the main reason to perform experiments [33, 34, 35, 36, 37, 38, 39, 12, 13]. In order to determine these newly introduced parameters, different kinds of experimental set-ups, *e.g.*, quasi-static/dynamic extension, shearing, or torsion tests, have to be performed [10, 2, 17, 18, 3, 40, 4]. Based on specific loading and boundary conditions, the determination of different unknown parameters can be achieved. In order to understand further the effect of manufacturing parameters, *e.g.*, slicing strategies or alignment orientations influence the inner parameters of the substructure, on the macroscopic mechanical deformation behavior, different slicing, alignment and positioning schemes during 3D prototyping have to be taken into account, respectively [41, 42, 43]. Consequently, based on the combination of the material and the additive manufacturing method, a different deformation behavior can be triggered, *e.g.*, a small or large (elastic) deformation.

Therefore, this work concentrates on the design, the manufacturing, the modeling, and the testing of the deformation behavior of metamaterials with differently sized pantographic substructures. PSs are designed by making use of a parametrized Computer-Aided Design (CAD) model, before being additively manufactured layer by layer by means of four different prototyping technologies:

- Fused Deposition Modeling (FDM),
- Stereolithography (SLA),
- Selective Laser Sintering (SLS),
- Direct Metal Laser Sintering (DMLS).

Examples of PSs made of different materials such as Polylactide Acid (PLA), Epoxy Resin (ER), Polyethylenterephthalat+Glycol (PETG), Polyamide (PA), and Aluminum (ALU) are given in Fig. 1. Based on the new material parameters, which have to be determined by means of an inverse analysis, the experimental set-up has to be developed and installed. Mainly quasi-static conditions have been taken into account in

- uniaxial extension tests,
- shearing tests, and
- torsion tests.

In order to evaluate experimental results qualitatively as well as quantitatively in an appropriate way, two-dimensional and three-dimensional Digital Image Correlation (DIC) is chosen. With this non-invasive optical measurement technique one is able to calculate displacements and strains on the outer surface of the metamaterial in real time. Results are compared with classical FEM calculations based on the Cauchy-Boltzmann continuum for small deformations as well as with second-gradient model calculations for large deformations adapted from [44]. With this experimental work a valuable contribution to the very promising research field of mechanics of metamaterials is carried out as further investigations and design/modeling approaches will rely on the determined material parameters. Moreover, by making the entire experimental data available for public, material parameters are provided for further investigations with the aim to achieve a better understanding of the exotic deformation behavior of pantographic sheets.

2 Materials and methods

The macroscopic deformation behavior of a metamaterial depends strongly on the architecture of its inner substructure. Based on preliminary investigations of the Italian research group headed by Prof. Francesco dell'Isola [6, 5, 13, 12], rapid prototyping technology was suggested to manufacture this kind of structures. By combining such complex inner geometries with well-known materials from 3D-printing, the aim of manufacturing such a structure, which is able to undergo resilient deformation behavior in the large elastic regime for example, became possible in the recent past [6, 14, 12, 13, 9]. In order to collect fundamental data gained by experiments, differently sized samples made of different materials have been considered in this work. Furthermore, based on determined material parameters, a classification of metamaterials with pantographic substructures can be performed, *e.g.*, by means of the well-known Ashby-charts [45, 46, 47]. However, in order to achieve these aims, new PSs have to be designed and manufactured.

In this section the fundament on which this work is built will be explained in more detail: the technical design and the parametrized method used to establish PSs by means of a commercial CAD tool will be pointed out in Subsect. 2.1. Four different manufacturing techniques and their corresponding raw materials, which are used to fabricate PS, will be explained in more detail in Subsect. 2.2. Due to the fact that each 3D-printer needs another raw material, at least four different materials were chosen to manufacture PSs. Furthermore, experimental set-ups with different loading and boundary conditions as well as different measurement methods are presented in Subsect. 2.3. The material modeling and the inverse analysis will be discussed in the last Subsect. 2.4.

2.1 Design of pantographic structures

In order to trigger the substructure's ability to perform resilient or large deformations, the quality and accuracy of the specimen's geometries and dimensions have to be adequate. This requires, besides an optimal manufacturing strategy, a detailed CAD model of the specimen. In Fig. 2 the CAD model of a PS generated by means of the commercial software Siemens NX 12 (Siemens Digital Industries Software, Berlin, Germany) is depicted. To achieve a flexible design of differently sized samples, a special parametrized model of the metamaterial's substructure was developed. An example of a

metameterial with a pantographic substructure and the schematic of a unit cell with its inner parameters is shown in Fig. 3. In contrast to a degrading modeling strategy, which

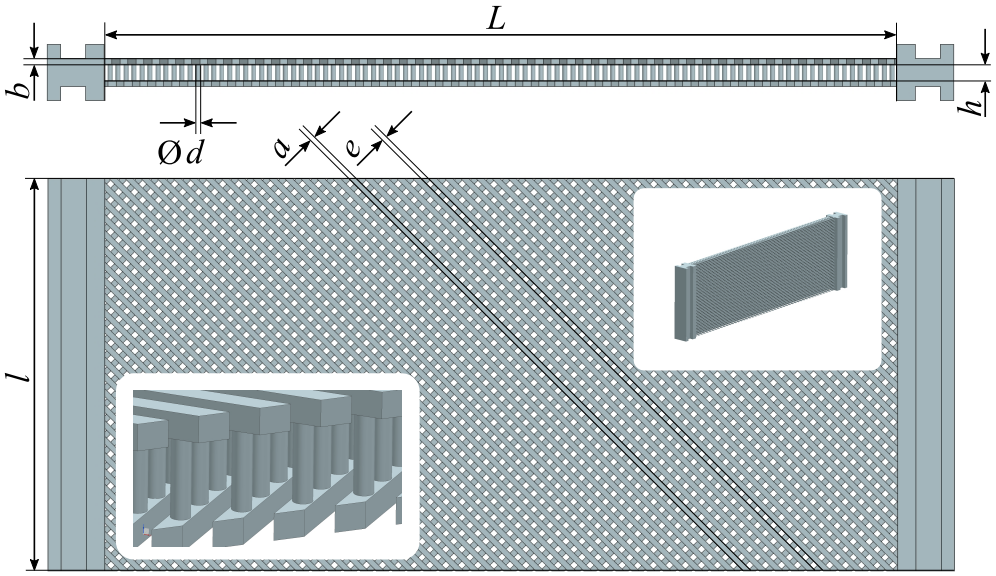

Figure 2: Different views of the CAD model of a pantographic sheet and its substructure with geometric parameters: a is the width of a beam, b is the height of a beam, $\varnothing d$ is the diameter of a pivot/cylinder, h is the height of a pivot/cylinder, e is the distance between two beams, l is the total height of the specimen, and L is the length of the specimen excluding the mounting areas. The periodic pattern of beams and the arrangement of cylinders is clearly visible.

is more powerful for special geometries like free-form surfaces, an additive modeling strategy was chosen. Because of the periodicity of the inner substructure of PS, the additive method is more straightforward: By introducing dependencies of the geometric parameters with respect to each other, differently sized specimens can be generated from only one CAD model, *e.g.*, by manipulating the main parameter, here the height of the beam b, on which all other inner parameters depend. A main advantage of this method lies in the possibility to change the inner parameters in an uncomplicated and efficient way when different sizes are required, *e.g.*, if the same specimen should be investigated with a different diameter of an inner cylinder/pivot $\varnothing d$. Notice that not only the inner parameters of the substructure have been investigated, *i.e.*, parameters a, b, $\varnothing d$, h, and e, but also the influence of the outer dimensions, *i.e.*, parameters L, l, and t on the deformation behavior have been taken into account in the fourth publication [4]. Specimens A, B, and C shown in Fig. 1 have a different length-to-height ratio ($L/l = 2$) than specimens D and E ($L/l = 3$) for example.

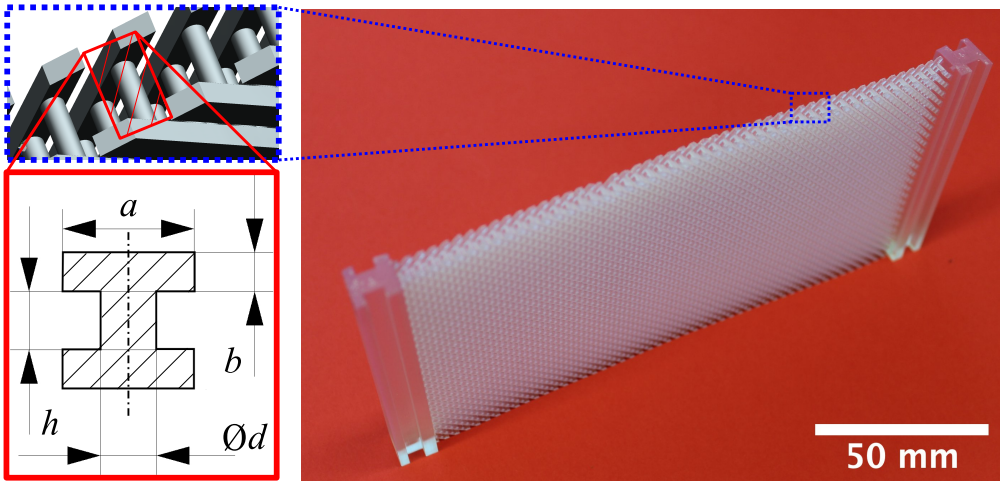

Figure 3: Pantographic structure made from transparent epoxy resin. CAD view of the inner substructure at the border region (blue box). A schematic of the cross-section of a Unit Cell (UC) on the substructure is shown in the lower left corner (red box). Parameters of UC correspond to parameters from Fig. 2: a is the width of a beam, b is the height of a beam, $\varnothing d$ is the diameter of a pivot/cylinder, and h is the height of a pivot/cylinder.

Obviously, this length-to-height ratio has a huge impact on the deformation behavior (because of the higher number of the "free-hanging" beams caused by different boundary conditions resulting in higher elastic deformation) and is going to be discussed further in detail in Sect. 5. An overview of all parameters (two outer and five inner parameters) of a PS is given in Table 1.

Description	Outer Parameter	Inner Parameter
Total sample length	L	-
Total sample height	l	-
Total sample depth	$t = 2b + h$	-
Beam width	-	a
Beam height	-	b
Distance between two beams	-	e
Pivot height	-	h
Pivot diameter	-	$\varnothing d$

Table 1: Inner parameters (a, b, e, h, and $\varnothing d$ on the substructure) and outer parameters (L, l, and t on the macroscale) of a PS corresponding to parameters from Figs. 2/3.

2.2 Additive manufacturing of pantographic structures

To ensure the best quality of specimens, which consist of complex sub-geometries, manufacturing techniques of high precision are essential. Therefore, rapid prototyping technologies are used to manufacture PSs additively. The focus lies on four different additive manufacturing technologies:

- Fused Deposition Modeling (FDM) by means of the commercial 3D-printer Ultimaker 3 Extended (Ultimaker B.V., Geldermalsen, Netherlands) located at the Institute of Mechanics, Technische Universität Berlin, Germany.
- Stereolithography (SLA) by means of the commercial 3D-printer Form 2 (Formlabs GmbH, Berlin, Germany) located at the Institute of Mechanics, Technische Universität Berlin, Germany.
- Selective Laser Sintering (SLS) by means of the commercial 3D-printer EOS Formagia P 100 (EOS GmbH, Krailling, Germany) located at the Institute of Mechanics and Printing, University of Technology Warsaw, Poland.
- Direct Metal Laser Sintering (DMLS) by means of the commercial 3D-printer EOS M 400 (EOS GmbH, Krailling, Germany) located at the Fraunhofer Ernst-Mach-Institute, Freiburg, Germany.

Each kind of 3D-printer needs another input of raw material:

- Polylactide (PLA) and Polyethylenterephthalat+Glycol (PETG) are used in FDM,
- Epoxy Resin (ER) in SLA,
- Polyamide (PA) in SLS,
- Aluminum (ALU) and heat treated aluminum (ALU-H) in DMLS.

Manufacturing methods and their process chains as well as material properties are introduced in the following subsections.

2.2.1 Fused deposition modeling

Fused Deposition Modeling (FDM), also known as Fused Filament Fabrication (FFF), is an additive manufacturing technology. Generally speaking, it melts and extrudes thermoplastic filament (raw material) layer by layer (bottom-up procedure) onto a horizontal, rectangle plane, the so-called printing platform, *i.e.*, here a heated glass

plate. One may say that this printing procedure is comparable to a regular paper-ink-printer with an additional degree of freedom in a third (vertical) direction in space. To ensure adhesion between the sample and the glass plate so that the specimen stays in place, and in order to reduce residual stresses on the interface between the printing platform and the printed specimen, the glass plate is heated up above the glass transition temperature of the raw material, *e.g.*, for PLA a temperature of around 60°C is required. In this work the commercial FDM-printer Ultimaker 3 Extended (Ultimaker B.V., Geldermalsen, Netherlands) produced batches of PSs made of PLA (Ultimaker B.V., Geldermalsen, Netherlands) and PETG (Material 4 Print GmbH \& Co. KG, Bad Oeynhausen, Germany). The printer and its printing area are depicted in Fig. 4.

(a) 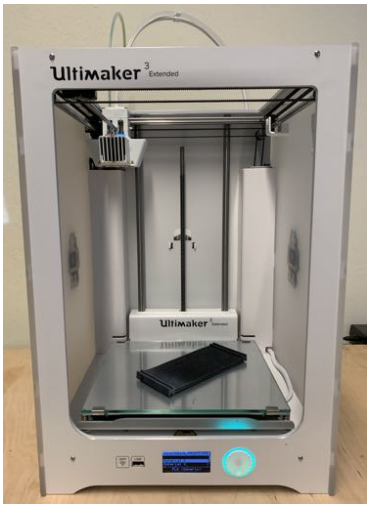

(b) 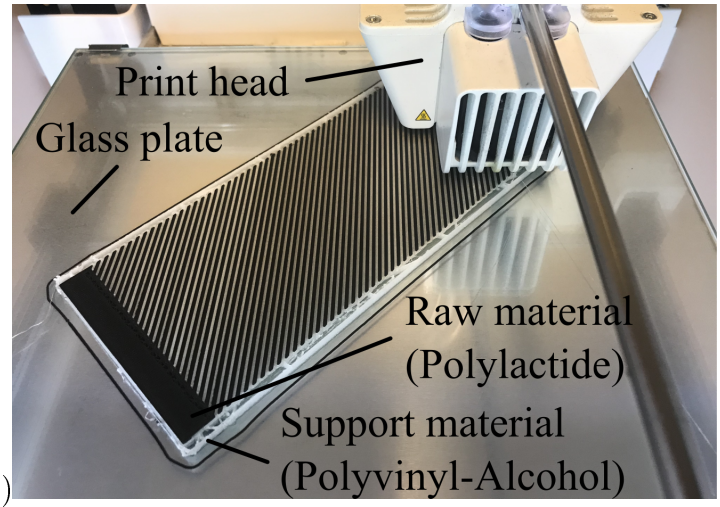

Figure 4: (a) Front-view of the Ultimaker 3 Extended FDM-printer; (b) horizontally aligned PS made from PLA during FDM print: a support structure made of polyvinylalcohol (white) is used to enable the print of undercuts. The printhead applies material layer by layer by means of a bottom-up procedure. PLA is black and support structure PVA is white.

Despite its comparatively low resolution and accuracy, a major advantage of this printer lies in the possibility to manufacture complex PS by printing two materials simultaneously. Two print-cores enable the print of free hanging beams made from the main material underpinned by support structures made from another material: The main material is PLA or PETG and the support structure is made of Polyvinyl-Alcohol (PVA, Ultimaker B.V., Geldermalsen, Netherlands).

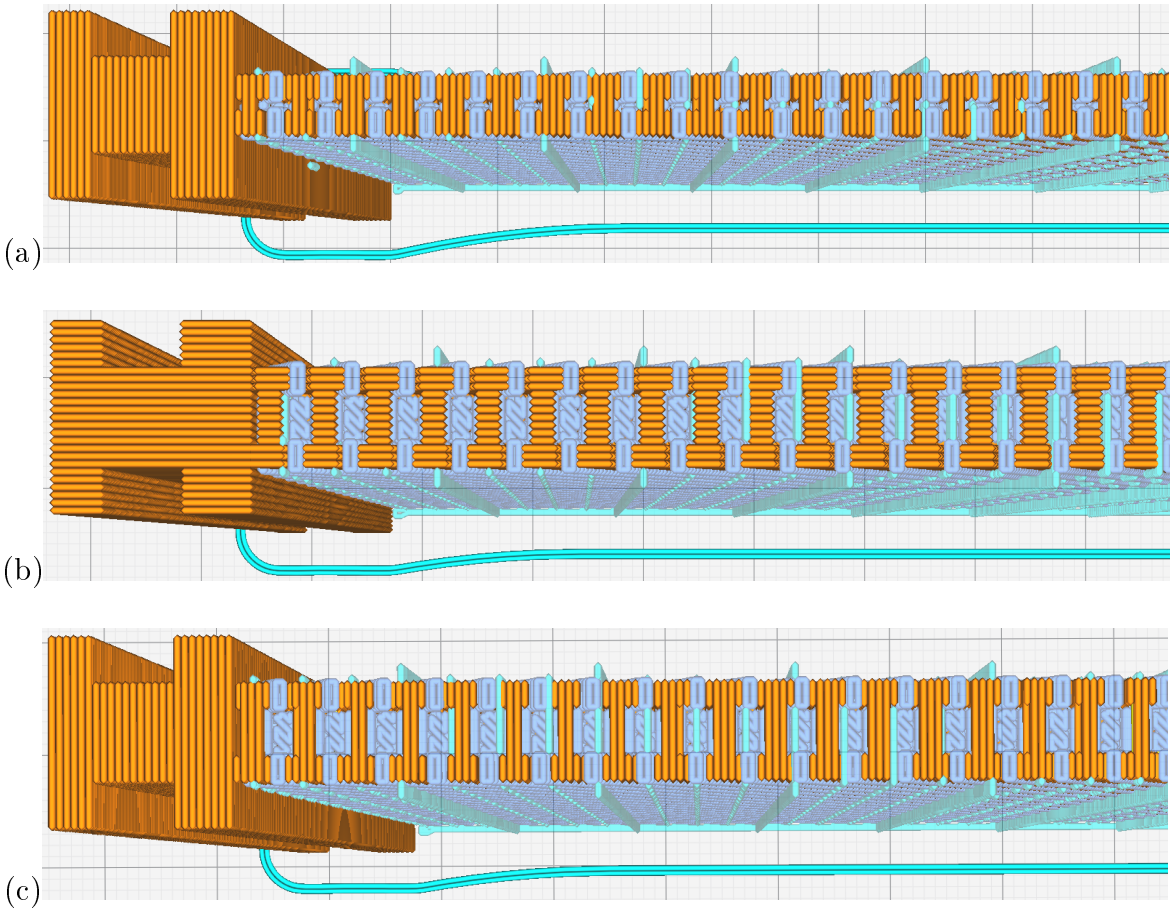

Figure 5: Top-view of slicing-schematics of upright-printed PETG-specimens using three different slicing strategies [43]: (a) printing direction of $g = 90°$ with respect to the lateral plane and a pivot-height of $h = 1$ mm; (b) printing direction of $g = 0°$ with respect to the lateral plane and pivot-height of $h = 3$ mm; (c) printing direction of $g = 90°$ with respect to the lateral plane and a pivot-height of $h = 3$ mm. Support structure is blue and raw material is orange.

An example of such a support structure is given in Fig. 5, which also shows different slicing strategies generated by means of the device's dedicated open-source software Cura (Ultimaker B.V., Geldermalsen, Netherlands). It should also be mentioned that besides printing temperature or printing velocity, the printing directions of the samples, see Fig. 5, have a significant impact on the deformation behavior [42, 43].

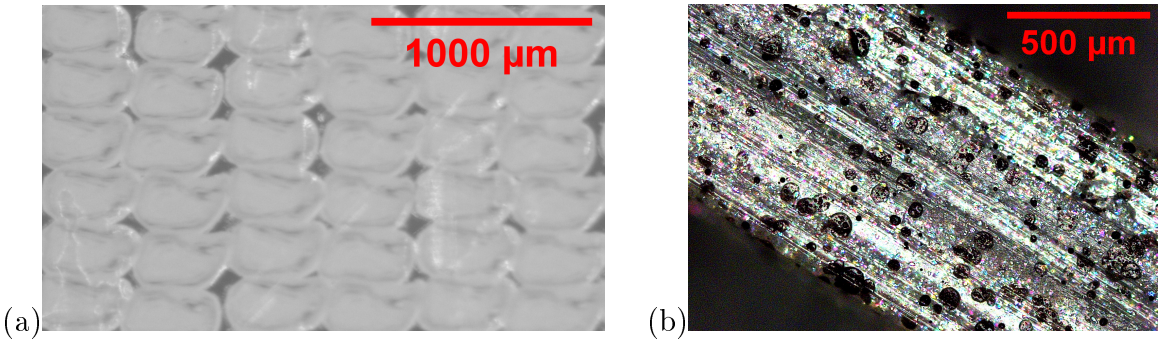

Figure 6: Microstructure of PS made of PETG (a) and PLA (b) after FDM print; (a) cross-section of a PETG extension sample shows imperfections between printing layers; (b) top-view of a PLA beam shows a homogenous surface with axial layer orientation (speckle pattern necessary for DIC-measurements, see Subsect. 2.3 for more details).

Furthermore, by investigating the microstructure intensively, see Fig. 6, some inhomogeneities, which can be easily identified especially in Fig. 6(a), suggest a direct influence of the overlay parameter set in the slicing software on the deformation behavior. Notice that the alignment of the specimen, *e.g.*, horizontal or vertical, see middle of Fig. 7, has also a huge influence on the printing direction and therefore on the global deformation behavior. These phenomena will be further discussed in Sect. 5.

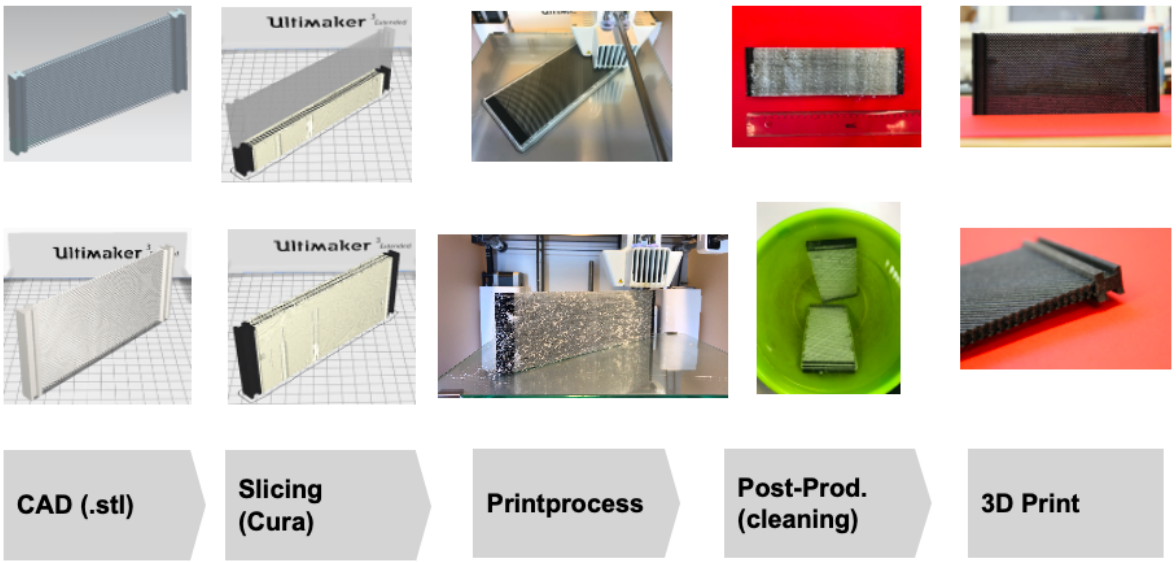

Figure 7: Process-chain of FDM-manufactured PSs: design, slicing, printing, cleaning, and quality check.

The process-chain of a FDM-printed metamaterial based on a pantographic substructure is very complex and shown in Fig. 7 for a PLA specimen. After designing and slicing, the proper printing procedure starts (middle of Fig. 7). Another important step is the post-production procedure: support structures have to be removed and the specimen has to be cleaned non-invasively afterwards with polypropylene. This can be achieved by making use of water-soluble materials, in our case PVA. Each specimen had to be drowned in water for at least 24 hours. Nevertheless, humidity changes the material characteristics. The linkage of the inner polymer chains on the microscale is not able to repel water. To overcome these limits, specimens had to be dehumidified for another 24 hours. By looking at the process chain of the manufacturing procedure it becomes plausible that a lot of factors influence the global deformation behavior of such a metamaterial. Therefore it is very important to manufacture each specimen batch following the same manufacturing protocol in order to make a comparison of different specimen possible. The FDM printing parameters as well as the raw material parameters of PETG, PLA, and PVA are summarized in Table 2.

Printing parameters	**FDM-PETG**	**FDM-PLA**	**FDM-PVA**
Layer thickness	0.2 mm	0.1 mm	0.1 mm
Layer width	0.4 mm	0.4 mm	0.4 mm
Print speed	55 mm/s	50 mm/s	35 mm/s
Initial layer speed	40 mm/s	15 mm/s	20 mm/s
Print acceleration	4000 mm/s^2	4000 mm/s^2	4000 mm/s^2
Printing temperature	250 °C	210 °C	225 °C
Printing temperature initial layer	255 °C	215 °C	230 °C
Initial Printing temperature	230 °C	200 °C	215 °C
Final printing temperature	240 °C	195 °C	210 °C
Bed temperature	70 °C	60 °C	60 °C
Material properties	**PETG**	**PLA**	**PVA**
Filament diameter	2.85 mm	2.85 mm	2.85 mm
Specific mass density	1.27 g/cm^3	1.24 g/cm^3	1.23 g/cm^3
(Ultimate) tensile strength	(53) MPa	45.6 MPa	78 MPa
Elongation at failure	70%	5.2%	9.9%
Tensile modulus	-	2346.5 MPa	3860 MPa
Flexural modulus	2150 MPa	3150 MPa	-
Melting temperature	200–230 °C	145–160 °C	163 °C

Table 2: FDM printing parameters and material parameters of PETG (Material 4 Print GmbH & Co. KG, Bad Oeynhausen, Germany), PLA (Ultimaker B.V., Geldermalsen, Netherlands) and PVA (Ultimaker B.V., Geldermalsen, Netherlands) obtained from manufacturers.

2.2.2 Stereolithography

In contrast to FDM, Stereolithography (SLA – also known as Stereo-Lithographic Addition) uses a light beam to cure a liquid photopolymer resin, *i.e.*, here Epoxy Resin (ER) which is stored in a translucent tank, layer by layer by means of an inverted upside-down procedure onto a horizontal printing platform. While the platform is being immersed in the liquid in the ER-tank, a laser spot is hardening the resin mixture. A spindle enables an additional degree of freedom in a third (vertical) direction in space. Between each layer a wiper is used to clean the translucent plane and to mix the liquid components. In order to reduce residual stresses in the specimens at the interface between sample surface and printing platform, a support structure is applied. The commercial SLA-printer Form 2 (Formlabs GmbH, Berlin, Germany) is used to produce PSs made of transparent/translucent epoxy resin (V4-FLGPCL0/RS-F2-GPCL-04, Formlabs GmbH, Berlin, Germany). The slicing procedure is taken out by the device's dedicated open-source software PreForm (Formlabs GmbH, Berlin, Germany). The printer and its printing area are depicted in Fig. 8.

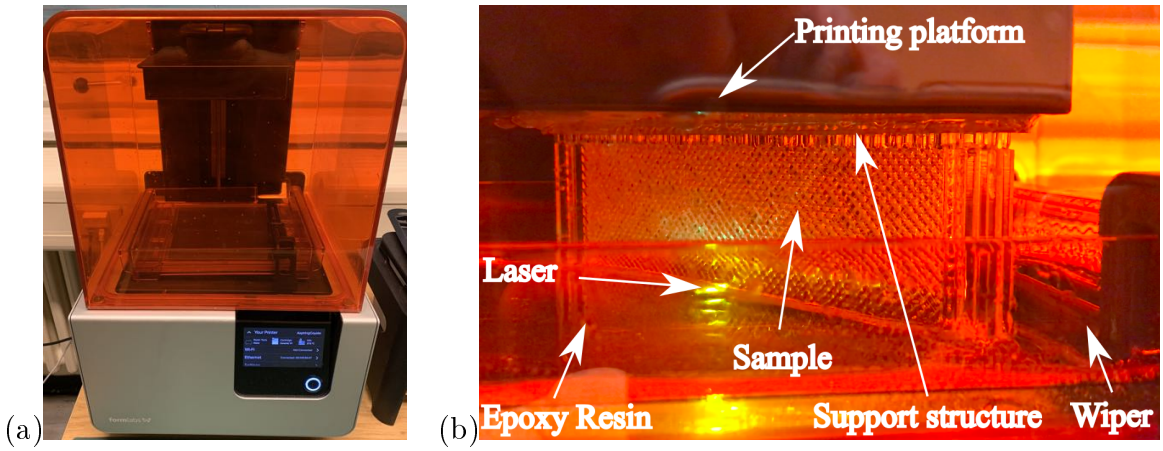

Figure 8: (a) Front-view of the Form 2 SLA-printer; (b) vertically aligned PS made of epoxy during print: a support structure, which is made of the same material as the specimen, epoxy resin (as seen between printing platform and specimen), is used to enable a stress-free print at about 38 °C. The laser-spot (yellow light) hardens the raw material layer by layer by means of an inverted upside-down procedure. The epoxy resin itself is transparent.

With the highest resolution and accuracy (25–100 µm) this SLA-printer enables the manufacturing of exotic geometries with very fine details as shown in Fig. 8. Printing directions and alignments influence the material/deformation behavior [42, 43]. This

Printing parameters	**SLA**
Layer thickness	0.1 mm
Laser diameter	0.14 mm
Laser output power	250 mW
Print temperature	35 °C
Initial Printing temperature	30 °C
Material properties	**ER**
Specific mass density	1.15–1.2 g/cm^3
Ultimate tensile strength	65 MPa
Elongation at failure	6.2%
Tensile modulus	2800 MPa
Flexural modulus	2200 MPa

Table 3: SLA printing parameters and material parameters of cured ER obtained from manufacturer (Formlabs GmbH, Berlin, Germany), post-cured with 1.25 mW/cm^2 of 405 nm LED light for 60 minutes at 60 °C in Form Cure (Formlabs GmbH, Berlin, Germany).

phenomenon will be further discussed in Sect. 5. The SLA printing parameters as well as the material parameters of ER are summarized in Table 3.

The process-chain of a SLA-printed metamaterial based on a pantographic substructure made of ER is depicted in Fig. 10. After designing and slicing, the proper printing procedure starts (middle of Fig. 10). The vertical alignment of the specimen minimizes the need of support structures resulting in less material costs and lower printing time. During post-production procedure, the specimen has to be cleaned in the Form Wash (Formlabs GmbH, Berlin, Germany) for 20 minutes in a polypropylen bath before the support structure was removed mechanically, see Fig. 11(a). To strengthen the inner polymer chains on the molecular-scale, specimens had to be cured for 60 minutes at 60 °C in the Form Cure (Form-

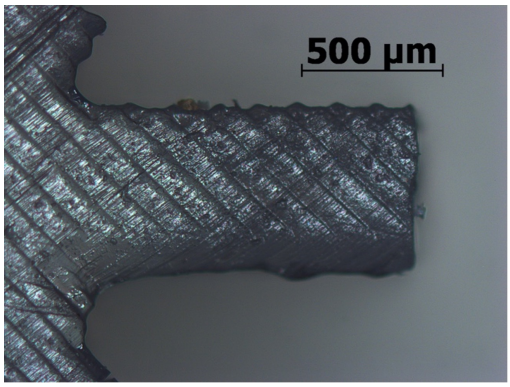

Figure 9: Microstructure of a broken epoxy beam after a quasi-static extension test. An angle of 45° with respect to the printing layers in the broken area indicates a brittle material behavior (see Sect. 5 and [4]).

labs GmbH, Berlin, Germany) at 405 nm wavelength, see Fig. 11(b). Every ER-specimen has been manufactured following the same protocol in order to make a comparison possible.

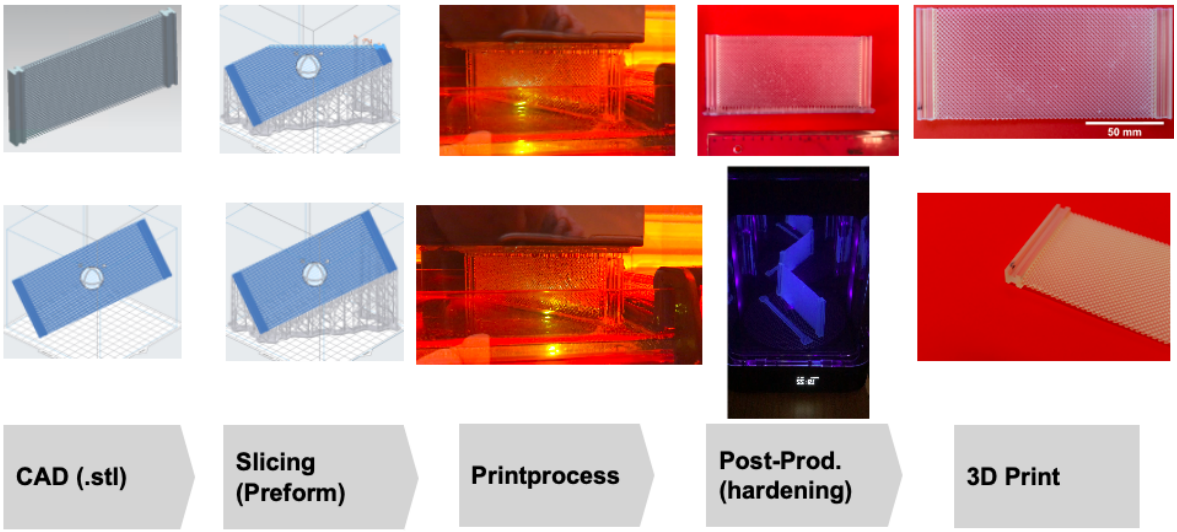

Figure 10: Process-chain of SLA-manufactured PSs: design, slicing, printing, cleaning, and quality check.

(a) (b)

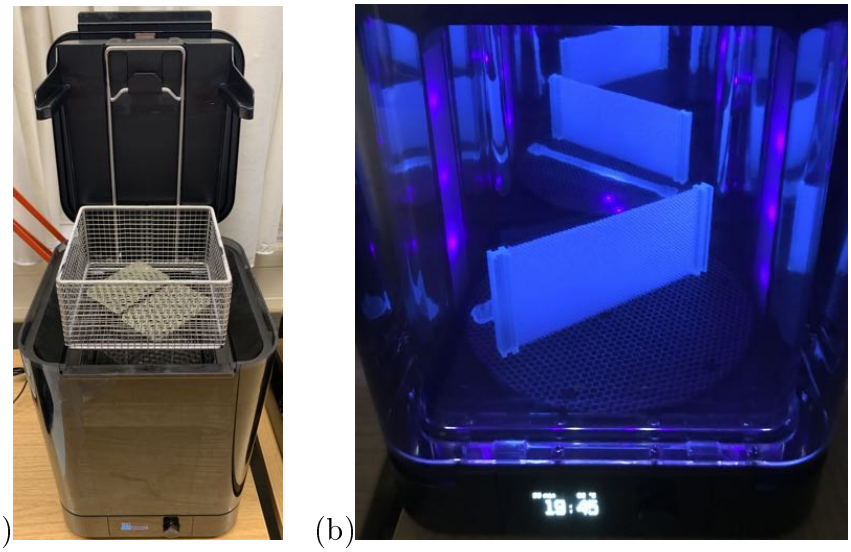

Figure 11: (a) Cleaning-station Form Wash (Formlabs GmbH, Berlin, Germany); (b) Curing-station Form Cure (Formlabs GmbH, Berlin, Germany).

2.2.3 Selective laser sintering

Selective Laser Sintering (SLS) fuses polymer powder layer by layer by means of a laser beam under inert gas atmosphere. A schematic is shown in figure in Fig. 12. After applying a thin layer of powder onto the construction platform, a laser beam is sintering the powder at predefined points in the first layer. The platform is then lowered and another layer of powder is applied with the help of a wiper and shaker. Again, the material is heated to allow a connection of the layers. This process is repeated until the sample is finished. After printing is completed, all specimens must cool down slowly (about 10 hours) and have to be finished by means of a high pressure cleaner. The commercial software Magics RP (Materialise, Leuven, Belgium) was used to prepare files as input for the printer EOS Formagia P 100 (EOS GmbH, Krailling, Germany) located at University of Technology Warsaw, Institute of Mechanics and Printing, Warsaw, Poland.

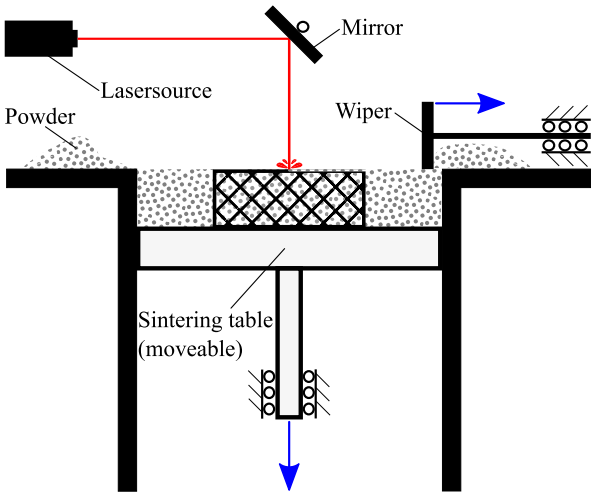

Figure 12: Schematic of selective laser sintering.

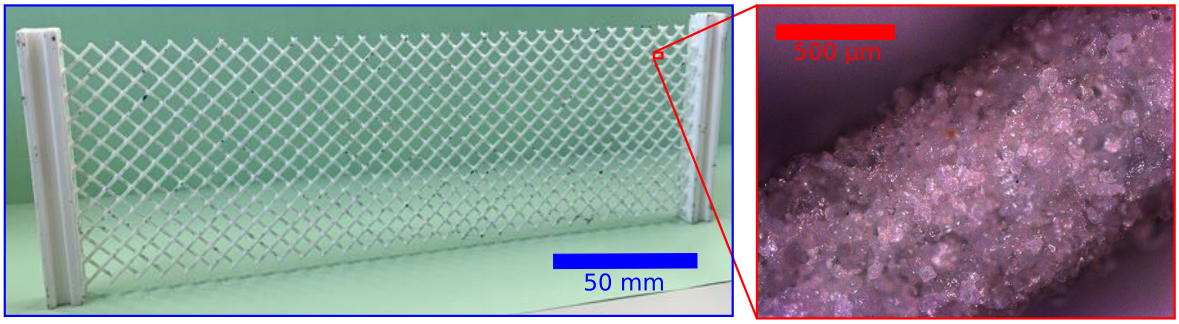

Figure 13: SLS-printed pantograph made of polyamide and its microstructure of a pantographic beam. Unassociated powder particles on the outer surface are clearly visible.

Polyamide powder (PA 2200, EOS GmbH, Krailling, Germany) with an average grain size of 56 µm was used as the precursor material. In contrast to FDM and SLA no

support structures are required which leads to lower material costs. The large assembly space in the printer allows a higher number of specimen batches to be printed at the same time resulting in a higher productivity rate in comparison with FDM and SLA. Another advantage is that no sophisticated post-production is required after cleaning. Nevertheless, the stiffness of SLA-printed specimen could not be reached with this technique. Furthermore, surfaces are rather rough resulting in lower accuracy compared with SLA, see Fig. 13. The porous microstructure and a low print-resolution of about 100–200 µm affect the quality and therefore the deformation behavior of the specimen as shown in [2]. Indeed, asymmetric out-of-plane movements have been measured for the PA sample during shearing tests and are discussed in Sect. 5. An overview of the used printing and material parameters is given in Table 4.

Printing parameters	**SLS**
Layer thickness	0.1–0.12 mm
Laser diameter	0.42 mm
Laser type	CO2 (30 W)
Material properties	**PA**
Specific mass density	0.45 g/cm^3
Tensile strength	48 MPa
Elongation at failure	24%
Tensile modulus	1700 MPa
Flexural modulus	1500 MPa
Melting temperature	176 °C

Table 4: SLS printing parameters and material parameters of PA obtained from manufacturer (PA 2200, EOS GmbH, Krailling, Germany).

2.2.4 Direct metal laser sintering

Direct Metal Laser Sintering (DMLS), also known as Selective Laser Melting (SLM) or Laser Powder Bed Fusion (LPBF), melts metal powder layer by layer by means of a focused laser jet. A protective atmosphere (Nitrogen) is used to avoid oxygen contamination. This technique follows the same procedure as the one described for SLS in the in the previous Subsect. 2.2.3 in Fig. 12. An EOS M 400 device (EOS GmbH, Krailling, Germany) was used to produce aluminum specimens made from AlSi10Mg metal powder (EOS GmbH, Krailling, Germany) with a generic particle size of about 25–70 µm and a 1 kW laser source.

In comparison to the plastic process, for the metal fabrication a special support structure and a complicated laser exposure strategy, elaborated by Fraunhofer EMI, Freiburg, Germany, was employed in order to avoid thermal distortions due to the higher energy input (for details see [2]). The specimens were positioned at a special angle with regard to the building direction in order to minimize the cross-sectional area of exposure in the layer wise process. This very angle was also chosen in a way such that the arrangements of beams and pivots ensured self-supporting. The mounting area was also supported. A contour based arrangement of laser tracks was used to minimize transient deviations of the energy input due to the inertia in the optical scanning system, see [2]. That approach fits the geometric characteristic of the slender beams in the best known way. A batch of aluminum specimens after production is shown in Fig. 14.

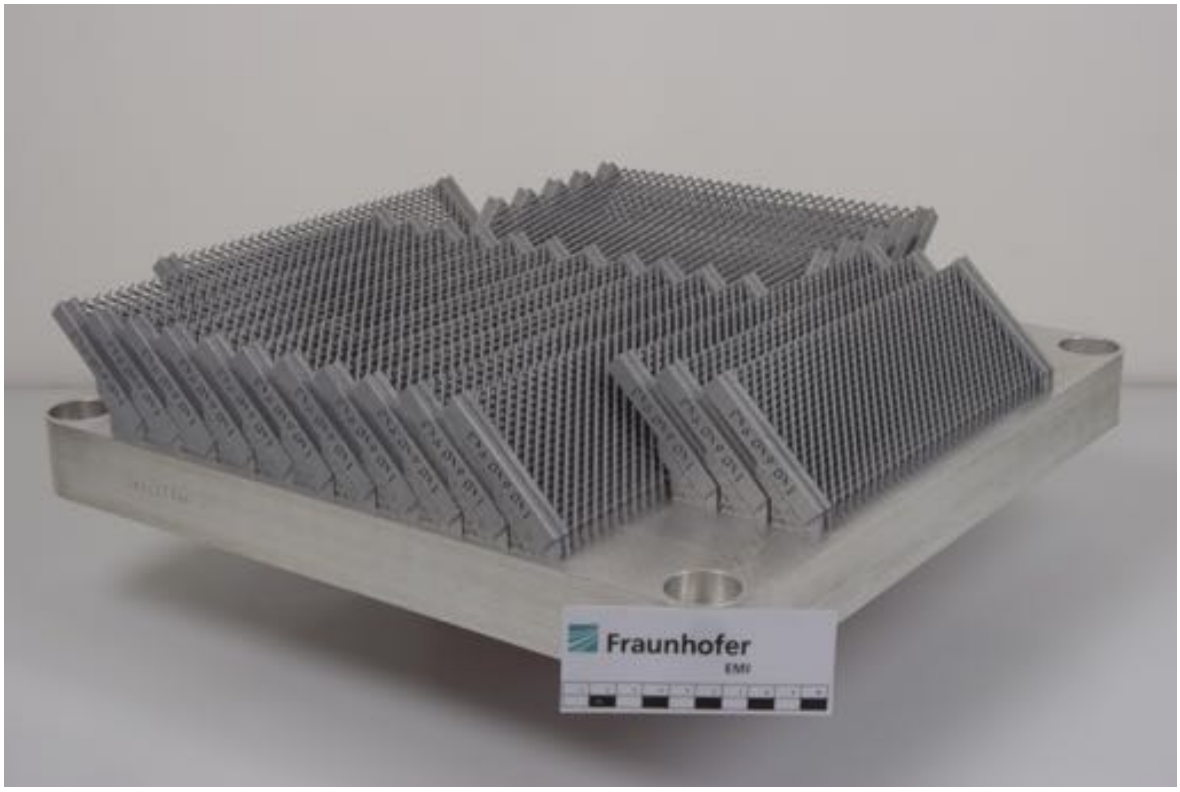

Figure 14: Batch of twenty DMLS-manufactured PSs made from AlSi10Mg powder, manufactured at Fraunhofer EMI, Freiburg, Germany.

Prior to support removal and separation from the building plate, a stress relief heat treatment (2 h at 300 °C) was employed for this configuration. Hence, the deviations due to thermal stresses were prevented. The heat treatment also results in ductile behavior of the material in comparison to the as-built properties [2]. By looking at the

meso-scale of a DMLS-manufactured specimen, which is shown in Fig. 15, irregularities at the surface can be identified. Even after heat treatment these heterogeneities remain and surely influence the deformation behavior.

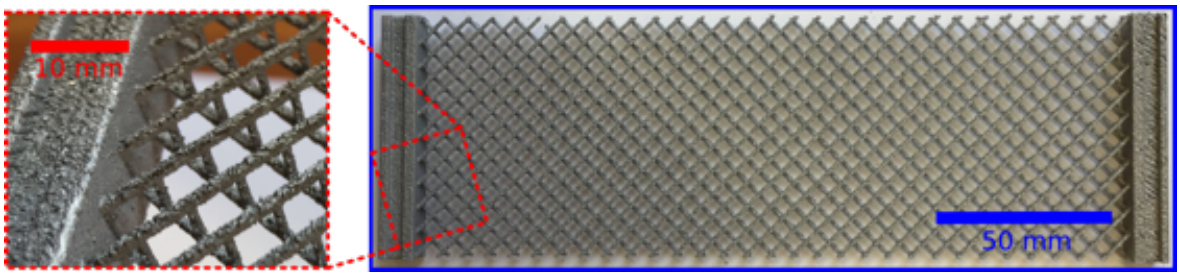

Figure 15: Front-view of a DMLS-manufactured pantograph (blue box) made of untreated ALU (AlSi10Mg) and a zoom-view on the mesoscale (red box). Inhomogeneity and porosity on the surface can be identified.

The schematic in Fig. 16 visualizes some of the main reasons for failures on the microscale in pantographic sheets which occur during the testing.

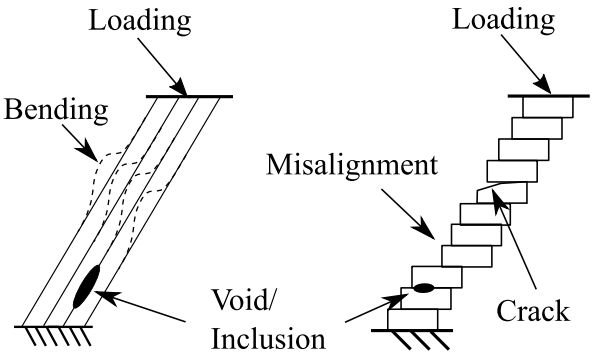

Figure 16: Schematic of layer by layer printed structures on the mesoscale while loading.

Based on different manufacturing problems, like insufficient printing strategies, *e.g.*, low melting/hardening temperatures or velocities, or unpredictable changes in the manufacturing environment, *e.g.*, wind/vibrations or air humidity, respectively, some of these imperfections, such as voids/inclusions/cracks or misalignments, can occur. Hence, finding the balance between an optimal input, *e.g.*, time effort, and output, *e.g.*, manufacturing procedure that is sufficient enough to guarantee a good quality of the specimens, became a major challenge in this work. Overviews of DMLS-printing parameters as well as heat treated ALU-H-material parameters and untreated ALU-material parameters are given in Table 5.

Printing parameters	**DMLS-ALU**	**DMLS-ALU-H**
Layer thickness	0.09–0.1 mm	0.09–0.1 mm
Laser diameter	0.09 mm	0.09 mm
Laser type	Yb-Faserlaser (1 kW)	Yb-Faserlaser (1 kW)
Material properties	**ALU**	**ALU-H**
Specific mass density	2.67 g/cm^3	>2.67 g/cm^3
Tensile strength	380–400 MPa	300 MPa
Elongation at failure	2–3%	5%
Tensile modulus	70–75 GPa	60–70 GPa
Melting temperature	570 °C	570 °C

Table 5: DMLS printing parameters and material parameters of ALU and heat treated ALU-H (for 2 h at 300°C) obtained from manufacturer (AlSi10Mg, EOS GmbH, Krailling, Germany).

2.3 Experimental set-ups

Quasi-static, uniaxial extension tests, shearing tests, and torsion tests have been established in order to determine new material parameters of pantographic sheets by means of an inverse analysis. With the focus to improve the quality of experimental results, reproducible tests have been designed. Furthermore, four different raw materials have been chosen with the aim to also allow mechanical interpretations of the deformed samples caused by the structure and not only by the material. In addition, various sample sizes and different testing procedures were taken into account requesting special adjusted set-up configurations, *e.g.*, mountings, measurement units, camera-systems *etc.*: On the one hand, pantographics made of different materials and geometries require different loading and boundary conditions, *e.g.*, aluminum samples need higher loads than the plastic ones. On the other hand, three-dimensional deformation movements, so-called out-of-plane movements, occur during shearing and torsion tests and have to be measured. Hence, experiments have been carried out at two different locations:

- Extension and shearing tests (two-dimensional deformations) have been carried out at the Department of Continuum Mechanics and Material Theories at Technische Universität Berlin, Germany. 2D-DIC was included to measure displacement on the in-plane deformed surfaces of pantographic sheets by means of the commercial single-lens reflex camera Canon 1000D (Canon Inc., Tokyo, Japan).
- Shearing and torsion tests (three-dimensional deformations) have been carried out at the Biomechanics Lab at Julius Wolff Institute at Charité Berlin, Germany.

3D-DIC was included to measure displacements and out-of-plane movements on the pantographs outer surfaces by means of the commercial optical measurement device Q-400 (Dantec Dynamics GmbH, Ulm, Germany).

2.3.1 Digital image correlation

As seen in [1], out-of-plane deformations can not be captured by standard measuring devices. Nevertheless, out-of-plane movements can be recorded by means of a non-invasive measurement technology: DIC is a non-contact optical technique to measure deformation on almost any surface [48, 49, 50].

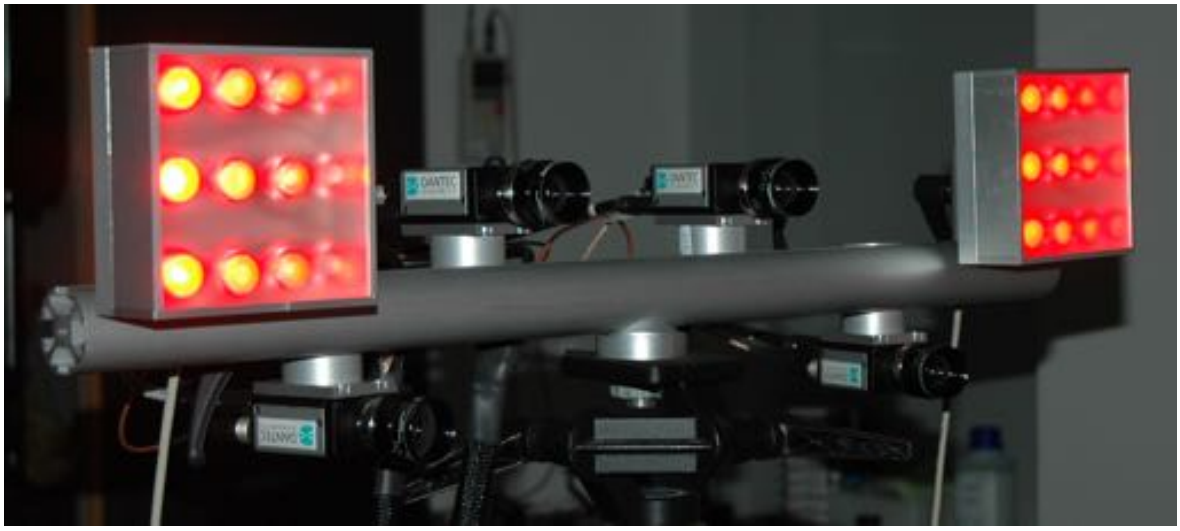

Figure 17: Dantec Q-400 measurement device (Dantec Dynamics GmbH, Ulm, Germany) consisting of four cameras and two illumination units is used to record the 3D-out-of-plane-movements in the lab of Julius Wolff Institute, Charité, Berlin, Germany.

This full-field image analysis method tracks grey value patterns in small local neighborhoods of digital images resulting in the determination of displacements/strains of an object under load in real time, see Fig. 20. The principle of 3D-DIC is as follows: at least two cameras are focused on the same object from different perspectives, see Fig. 17. The entire field of view is divided into so-called facets as shown in Figs. 18(b)/20. These facets consist of many pixels, mostly square subset of pixels, and follow the so-called speckle pattern during loading as shown in Fig. 18(b).

To ensure correct separations of the facets and because of lack of structure and contrast, a speckle pattern has to be sprayed on the sample's surface by means of an airbrush system and acrylic-based waterproof ink (Molotow One4All, Feuerstein GmbH, Lahr, Germany) as shown in Fig. 18(a). Furthermore, before measurements can be carried out, a complex calibration procedure has been performed by the aid of a calibration panel, see Fig. 19. After calibrating the intrinsic parameters, *i.e.*, focal length, image sensor format, principal point, and lens distortion, and after calibrating the extrinsic parameters, *i.e.*, translation vector and rotation matrix, by means of the chess-like calibration panel under different points of view, an optimization residual of $r = 0.0809$ was achieved (recommendation of the manufacturer Dantec Dynamics GmbH, Ulm, Germany, is less than $r_{\mathrm{M}} \leq 0.3$–0.5). The position of each point on the object can be calculated by making use of a special transformation algorithm based on the grey values of the facets, see Dantec Dynamics GmbH, Ulm, Germany, and [51]:

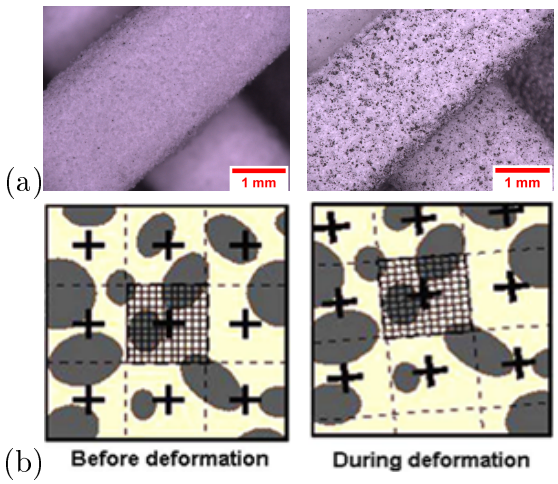

Figure 18: (a) Pantograph before and after speckle pattern painting; (b) overlap of facets which consist of subsets of pixels on the speckle pattern [49]. Pattern in the facets move during deformation.

$$G_t(x_t, y_t) = g_0 + g_1 \cdot G(x, y) \ , \tag{1}$$

$$x_1 = a_0 + a_1 \cdot x + a_2 \cdot y + a_3 \cdot x \cdot y \ , \tag{2}$$

$$y_1 = a_4 + a_5 \cdot x + a_6 \cdot y + a_7 \cdot x \cdot y \ , \tag{3}$$

with $G(x, y)$ as the grey value of a pixel with the coordinate x and y in the reference state, g_0 and g_1 as illumination parameters, and a_0–a_7 as affine transformation parameters. Within the correlation algorithm the difference $\Sigma\,[G_T(x_T, y_T) - G(x, y)]^2$ of these patterns is minimized at a certain time T. Based on these results the displacements can be calculated. For more details see [51, 49]. As previously described, a correlation in three dimensions is made possible by the usage of more than one camera. It is therefore possible to show the change in depth of a tilted, rotated, or translated surface. This is

necessary for the correct interpretation of non-planar deformations, especially during shearing tests, and is a big advantage in contrast to previous investigations which are based on 2D-DIC [38, 1, 18].

The mobility of the 3D-DIC system is another advantage to other common measurement methods such as ultrasonic, electronic speckle pattern interferometry, or computer tomography [49]. It can be built up in a different location in the lab or with a different set-up within minutes which enables a smooth adjustment to unpredictable circumstances, which – as we all know – always happen during novel experiments. Note that unlike glued strain gauge elements, the non-contact method in DIC is very beneficial. In general, strain gauges make direct contact to the sample surface by using a thin layer of glue, which affects the surface movement of the sample and falsifies the results. Besides it is very fragile to changes in temperature. This can also be avoided by using DIC.

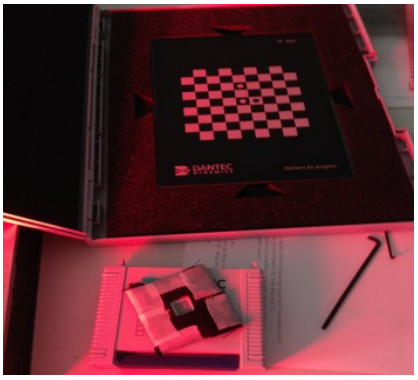

Figure 19: Used calibration target Al-11-BMB 9x9 (Dantec Dynamics, Ulm, Germany).

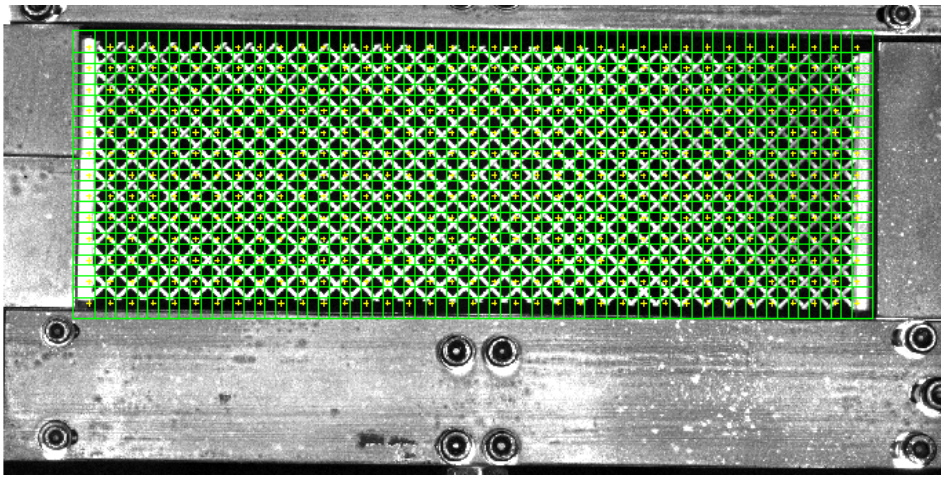

Figure 20: Raw data of a PA sample before shear deformation gained by Istra 4D correlation software (Dantec Dynamics, Ulm, Germany). Green boxes represent the facet mask. Yellow points represent the center points of the facets. A quadratic facet size is 57 × 57 pixels. Grid spacing is 37 pixels so that a facet overlay of 20 pixels could be achieved. 3D-residuum of 1.65 pixels was calculated with an accuracy of 0.2 pixels and a grey value residuum of 20.

2.3.2 Extension and shearing tests – 2D-digital image correlation

A testing device MTS Tytron 250 (MTS Systems Corporation, Eden Prairie MN, USA) controlled by the device's dedicated software Stationsmanager V 3.14 was used during displacement-controlled, quasi-static extension and shearing tests at the Institute of Mechanics, Department of Continuum Mechanics and Material Theories at Technical University in Berlin, Germany. Fig. 21 shows the schematics of the extension and shearing experiments. Because of the limitation of the testing device to apply movement only in horizontal direction, samples for shearing tests have been rotated with an angle of 90° with respect to the samples investigated in extension tests. Furthermore, new steel-mountings have been designed, manufactured and installed into the attachments of the testing device. This way shear-displacement was enabled. Extension test of a PETG sample and shearing test of a PLA sample are presented in Fig. 22. The reaction force R_{eng} was measured by the device's integrated load cell attached to the fixed clamping. This load cell is able to record axial forces in a range of $F = \pm 250$ N with an accuracy of $\Delta F = \pm 25$ mN.

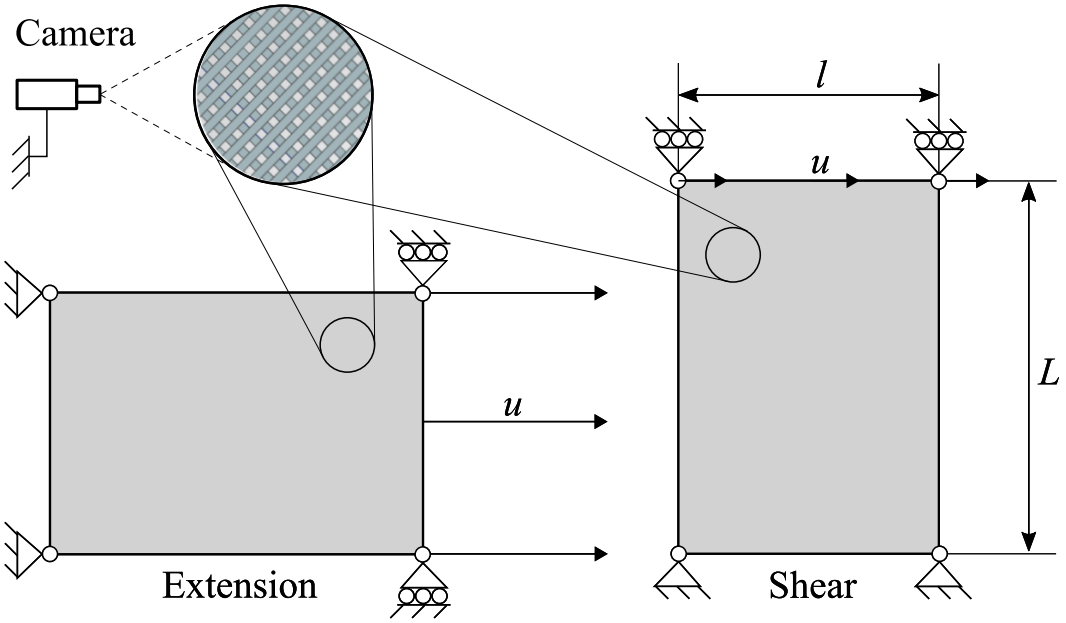

Figure 21: Schematic of displacement-controlled extension test (left) and shearing test (right). Detail-view shows periodically aligned beams of the inner structure with an angle of 90° with respect to each other. A camera is recording the planar deformation of the whole specimen. Prescribed displacement is given by u, the length of the sample by L, and the height of the sample by l being consistent with the nomenclature listed in Table 1.

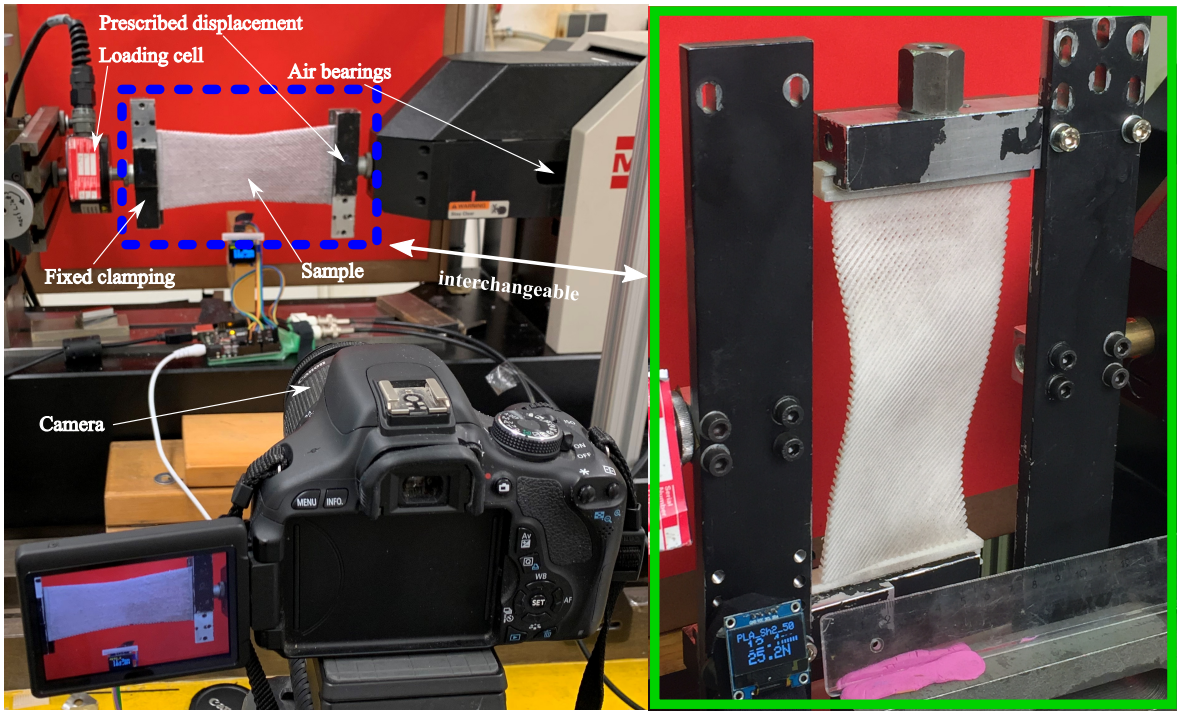

Figure 22: Set-up of displacement-controlled extension test performed on a PETG sample (blue box) and set-up of shearing test performed on a PLA sample (green box): loading cell is fixed in the left clamping jaw while displacement u is imposed horizontally by the right clamping jaw. By manipulating the interchangeable mounting adaptors an easy switch between the test set-ups is possible.

Both, extension-displacement $u_{\text{ext.}}$ and shear-displacement u_{shear}, were imposed horizontally with a loading rate of $v = 15$ mm/min. Experiments were performed displacement-controlled using a DC-linear servomotor in combination with a spindle with an accuracy in the µm range. Displacement was measured and monitored by an integrated encoder unit. Additionally, a picture was taken every two seconds by means of a commercial Canon EOS 1000D camera with a resolution of 4272 × 2848 pixels. The open-source-softwares ImageJ 1.50i (NIH, Bethesda, USA) and GOM Correlate 2017 (GOM GmbH, Braunschweig, Germany) were used to evaluate image data by means of 2D-DIC. Fig. 23 shows exemplary the planar deformation of a PS made of PETG during an extension test evaluated by 2D-DIC by means of GOM Correlate 2017 [43]. Notice that almost frictionless movements could be achieved by making use of an air-film-bearing. External vibration was avoided by using a massive substructure and by arranging the system horizontally.

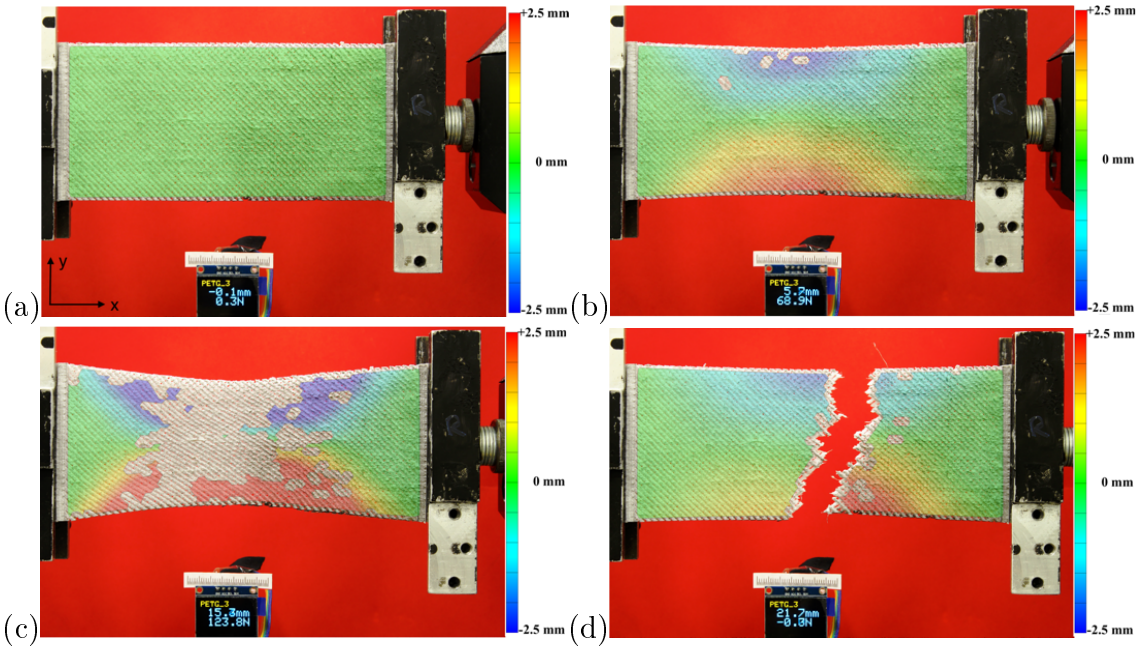

Figure 23: Overlapping picture-sequence during extensional deformation of PETG sample [43], validated by 2D-DIC (vertical displacement $u_{yy} = \pm 2.5$ mm): (a) Initial state before deformation. (b) During deformation: a necking of the specimen can be recognized at an axial elongation of about $\varepsilon_{yy} = \pm 1\,\%$. Maximal vertical displacement reaches about $u_{yy} = \pm 2.5$ mm at this deformation state. (c) After first failure: at an axial elongation of about $\varepsilon_{yy} = \pm 4\,\%$, a pivot breaks locally in the upper left corner of the specimen without resulting in ultimate failure. Lack of focus prevents correlation resulting in lost facets. (d) After ultimate failure: global rupture through the whole specimen in vertical direction in the middle of the specimen.

2.3.3 Shearing and torsion tests – 3D-digital image correlation

A Zwick Z010 testing device (ZwickRoell GmbH & Co. KG, Ulm, Germany), controlled by the device's dedicated software TestExpert, was used to perform displacement-controlled shearing tests and angle-controlled torsion tests at the Julius Wolff Institute at Charité Berlin, Germany. Schematics of both experimental set-ups are given in Fig. 24. The axial reaction force R_{eng} was measured by a device integrated load cell (Zwick-Series Xforce) being able to record axial forces in the range of $F = \pm 10$ kN with a calibrated accuracy of 0.1 % at 20 N. The quasi-static shear-displacement u was induced vertically with a velocity of $v = 15$ mm/min and was recorded by an integrated encoder unit with an accuracy of $\Delta u = \pm$ 2.0 µm. Moments were measured by means of an integrated torque sensor (Zwick-Series M) while torsion was induced

quasi-statically with $\omega = 1°/\text{min}$. The torsion transducer is able to record torques up to $M = \pm 20$ Nm with a resolution in the mNm range and resists maximal axial forces up to $F_M = \pm 5$ kN, which is obviously sufficiently enough for the tests performed on the pantographs.

The measurement device Q-400 (Dantec Dynamics GmbH, Ulm, Germany) was installed to record the state of three-dimensional deformation on the surface by the help of four cameras as given in Figs. 17/25. During the deformation process, pictures have been taken via a direct TTL-signal every two seconds with a resolution of about 1600 × 1200 pixels resulting in a synchronization of picture to the related force value. The device's accompanying commercial software Istra 4D (Dantec Dynamics GmbH, Ulm, Germany) is able to calculate three-dimensional surface deformations after calibrating the parameters from Eqs. (2-3) using the chess-like calibration target shown in Fig. 19. This software was used for all 3D-correlations without making use of smoothing operators. Torsion test performed on a heat treated ALU-H sample and shearing test performed on a PA sample are visualized in Fig. 25. Furthermore, Fig. 26 shows the raw data of the performed experiments, *i.e.*, raw data of the shear experiment in Fig. 26(b) and raw data of the torsion experiment in Fig. 26(d), and side-views in which out-of-plane movements can be recognized in Figs. 26(a)/(c).

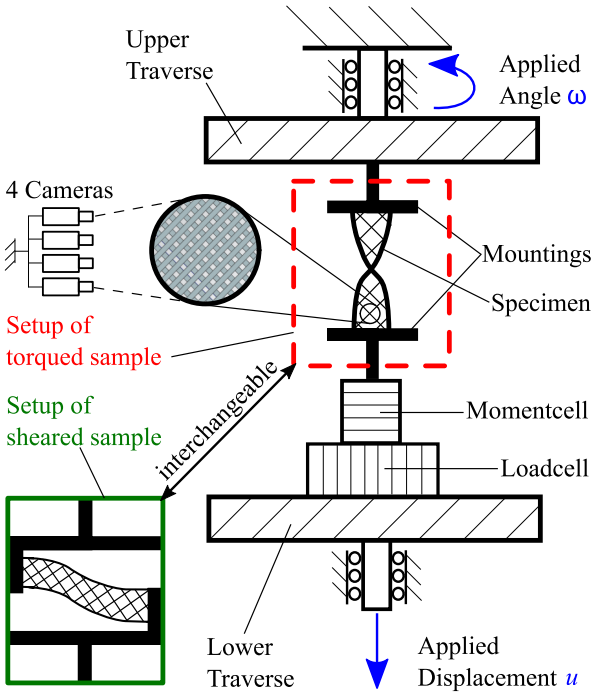

Figure 24: Schematic of angle-controlled torsion test (red box) and displacement-controlled shearing test (green box). Four cameras record in/out-of-plane movements of the whole specimen. Displacement is given by the parameter u, the angle by ω.

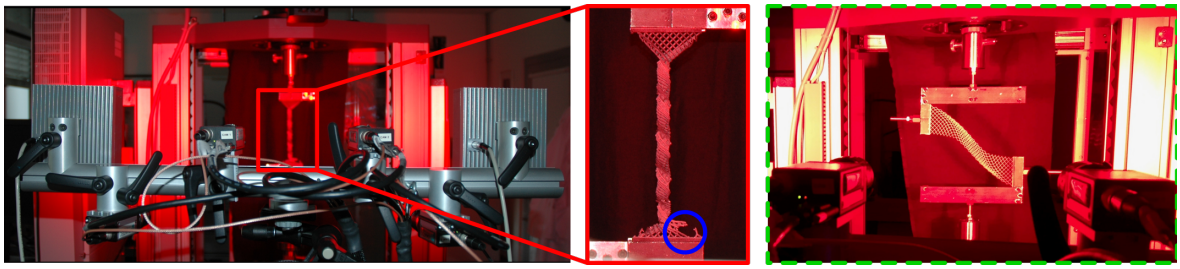

Figure 25: Set-up of a torsion test (ALU-H) in the lab of Julius Wolff Institute at Charité Berlin including 3D-DIC measurement device Q-400 (Dantec Dynamics GmbH, Ulm, Germany) in the front on the left picture and testing machine Zwick Z010 (ZwickRoell GmbH & Co. KG, Ulm, Germany) in the back on the left picture. Detail-view in the middle picture (red box) shows the heat-treated aluminum sample after two full rotations. Ductile failures of beams at the lower right mounting side are visible (blue circle). Set-up of a shearing test (PA) is given on the right side (green box).

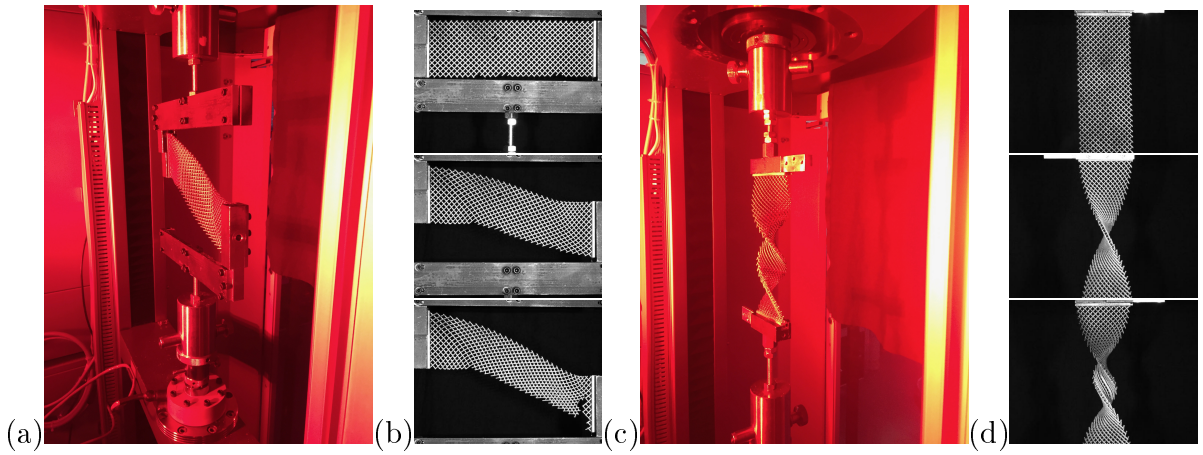

Figure 26: (a) Side-view of a shearing test performed on an aluminum sample (ALU); (b) picture sequence of camera-raw-data of a sheared ALU sample (up to 100% shear-elongation); (c) side-view of a torsion test performed on a heat treated aluminum sample (ALU-H); (d) picture sequence of camera-raw-data of a torqued ALU-H sample (up to one full rotation). Experiments have been performed in the lab of Julius Wolff Institute at Charité Berlin, Germany.

Exemplary, results of out-of-plane image correlations of PA samples are given in Fig. 27 (torsion) and Fig. 28 (shear). In order to obtain scalar results for an out-of-plane displacement of a sheet, a point in a single facet, *i.e.*, a sub-area of image correlation, or an average area like a circle or a polygon can be selected for each sample, respectively.

This point/area is located in the place where maximal out-of-plane movement has been presumed. Due to the large deformations, some facets moved out of the optical focus, which caused the image correlation to abort. Furthermore, when a sudden rupture occurs in between the shutter releases of the cameras, so that the facets to be correlated are displaced laterally too much, image correlation is aborted. For these reasons some of the facets can be incomplete, *e.g.*, in Fig. 23(c). Notice that results obtained from DIC measurements indicate that vertical parallelism of both (optimized) mounting sides is still given, even for high loads acting on the aluminum specimen during shear load.

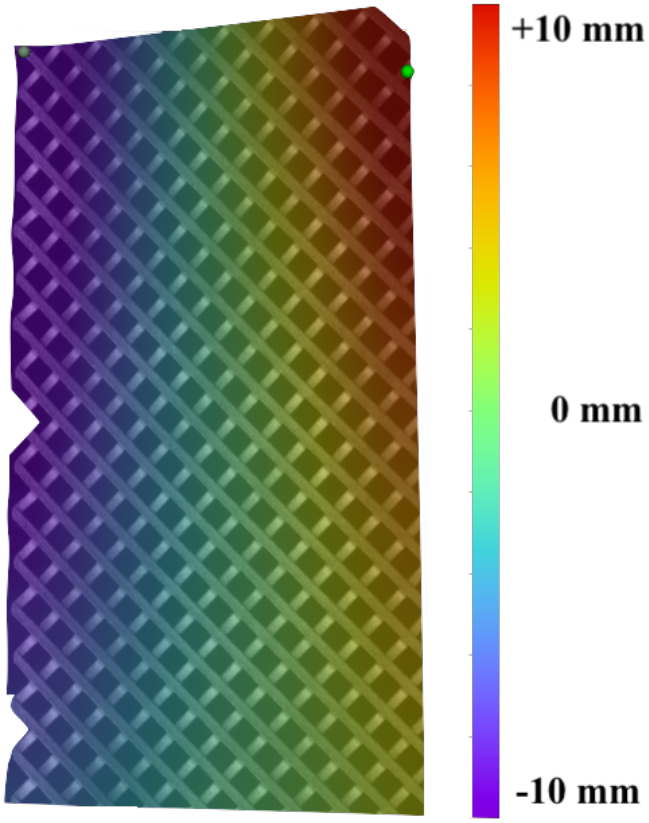

Figure 27: Torque deformation of a PA sample, validated by 3D-DIC [3]: Overlay of the structure and the contour of out-of-plane displacements. Maximal out-of-plane movements reach about $u_{zz} = \pm 10$ mm.

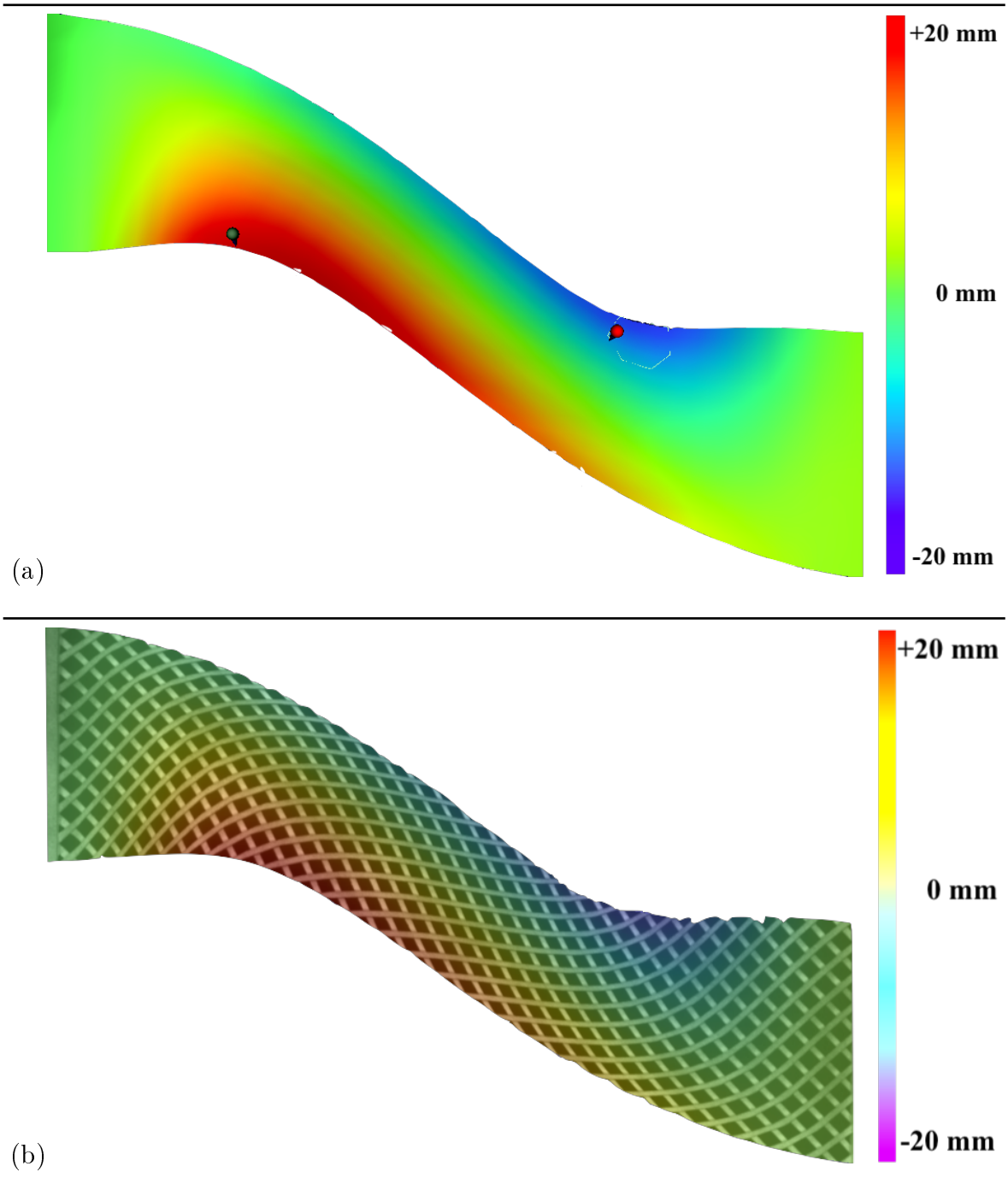

Figure 28: Shear deformation of a PA sample (more than 100% of shear-elongation), validated by 3D-DIC [3]: (a) Contour of the out-of-plane displacement. Region of interest is marked by a circle or a pin, respectively; (b) Overlay of the structure and the contour of out-of-plane displacements. Maximal out-of-plane movements reach about $u_{zz} = \pm 20$ mm in both graphs.

2.4 Material parameter identification – inverse analysis

It is well known that metamaterials with a pantographic substructure are able to deform in a large, (non-)linear elastic manner [11, 14, 12, 13, 1, 2, 52, 4, 40, 17, 53, 43, 38]. A classic Cauchy-Boltzmann-Continuum model, *e.g.*, Hooke's law, is not sufficient to describe and predict non-linear stress-strain relationships during large deformations of pantographic sheets. As mentioned in Sect. 1 higher gradient theories are able to overcome these limits. During the development of higher gradient theories, constitutive laws with new parameters show up. These new parameters are often directly linked to the the material and the inner structure showing a very strong influence on the macroscopic deformation behavior. Indeed, they are often referred to as so-called higher material parameters or higher structure parameters or just higher parameters. Their quantitative values are usually unknown. Furthermore, a qualitative description of their physical meaning is very rare or imprecise, not to mention impossible for some cases. To push the boundaries, experiments are required and essential in this field of research. Their results are used to determine these unknown (higher) parameters with the aid of an inverse analysis.

2.4.1 Small deformations

With the aim to compare results of isotropic, linear-elastic numerical simulations with experimental results of small deformations, *i.e.*, axial elongation smaller than 3 % (see [4]), an inverse analysis has to be performed [43, 4]. Therefore, so-called effective parameters have to be determined, *i.e.*, in this case the effective Young's modulus $E_{g_{\text{eff.}}}$. Note that the index g describes the layer orientation with respect to the lateral plane of an additively printed PS [43], as exemplary depicted in Fig. 5. A PS is assumed to behave as one body, *e.g.*, as a kind of a "spring" in investigations performed in the 4th publication [4]. Indeed, the term "effective" implies that effective material parameters, *e.g.*, here the parameter $E_{g_{\text{eff.}}}$, are not real material parameters but refer to engineered stiffnesses which depend on the "smeared out", entire specimen, *i.e.*, the combination of material and structure including geometries on the microscale. Therefore, the effective Young's modulus $E_{g_{\text{eff.}}}$ can also be replaced by a stiffness parameter $c_{g_{\text{eff}}}$ resulting in

$$E_{g_{\text{eff.}}} = c_{g_{\text{eff}}} \ . \tag{4}$$

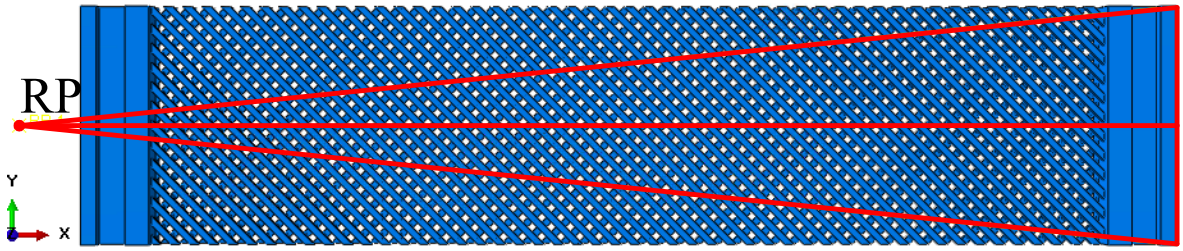

Figure 29: Model of a PS in Abaqus 6.14 (Dassault Systemes, Vélizy-Villacoublay Cedex, France). The reference point RP is linked via a rigid coupling to the outer surface of the right mounting (red lines). Prescribed displacement u and calculated reaction force R_{sim} are coupled to the fixed reference RP and therefore imposed (u) or calculated (R_{sim}) on this very point, respectively. The left mounting side is fixed.

To allow a reasonable fit between the parameters obtained from simulation c_{sim} and the values gained by experiments $c_{0_{\text{eff}}}$ in the presumed case of an isotropic material, only the linear elastic deformation regime is taken into account. Furthermore, since the (engineered) reaction force ΔR_{eng} triggered by the global deformation of a PS during a real extension test is measured in a single reference point RP in the load cell, which is located on the very center line/mid axis of the specimen, see. Fig. 22, the calculated maximal force output value R_{sim} of the numerical simulation was also coupled to one RP, see. Fig. 29. Alternatively, each force-point on the outer surface has to be integrated over the entire surface of the movable right mounting side. Therefore, Hooke's Law is valid for small deformations under the aforementioned restrictions [4]:

$$\sigma = E\varepsilon \ , \tag{5}$$

where the Young's modulus E is introduced as a linear proportional factor between stress σ and strain ε. The stress σ can be described as the quotient of measured force ΔR_{eng} and the projection onto the mounting-side of an initial cross-section A_{proj}. The strain ε is defined as the quotient of measured elongation $\Delta\ell$ and initial length ℓ resulting in the equation for the effective stiffness parameter

$$c_{g_{\text{eff}}} = \frac{\Delta R_{\text{eng}}}{A_{\text{proj}}} \frac{\ell}{\Delta\ell} \ , \tag{6}$$

with $g = 0$ for printing direction of 0° with respect to the lateral plane of the specimen and $g = 90$ for 90°, respectively [43]. Examples of determined stiffness parameters are given in Table 6.

Parameter	Value PLA	Value ER	Value PETG
$c_{0_{\text{eff}}}$	15.51 MPa	16.55 MPa	9.58 MPa
c_{sim}	17.98 MPa	17.17 MPa	8.45 MPa

Table 6: Comparison of an experimentally measured reduced stiffness parameter $c_{0_{\text{eff}}}$ ($g = 0$) with a numerically calculated stiffness parameter c_{sim} of an extended PLA sample [4], an extended ER sample [4], and an extended PETG sample [43], respectively.

2.4.2 Large deformations

For a metamaterial with a pantographic substructure, the classical Cauchy-Boltzmann continuum model mostly fails in order to investigate large deformations and hence a 2nd gradient continuum model is necessary to describe many of its deformation behaviors [28, 6, 17]. Intending to compare results of a 2D continuum model embedded in a 3D space adapted from [44, 54] with shear experiments performed in the second and third publication [2, 3] quantitatively, a variational framework is used. The following orthotropic deformation energy density is taken from [44]:

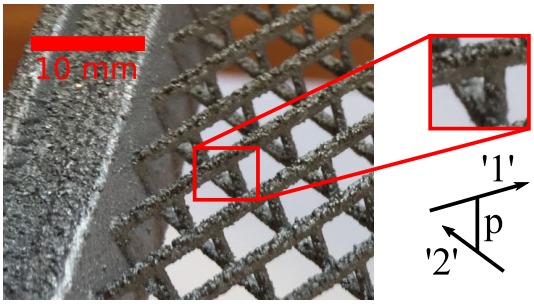

Figure 30: Reference frame of both families of fibers $\alpha =$ '1' and $\alpha =$ '2', and the interconnected pivot p.

$$\begin{aligned}\pi \;=\; \frac{1}{2}\Bigg\{ & \mathrm{K_e}\left[\left(\varepsilon^1\right)^2+\left(\varepsilon^2\right)^2\right]+\mathrm{K_s}\left(\left[1+\left(\frac{\gamma}{Q}\right)^2\right]^m-1\right)+ \\ & +\mathrm{K_t}\left[\left(\kappa_1^1\right)^2+\left(\kappa_1^2\right)^2\right]+\mathrm{K_n}\left[\left(\kappa_2^1\right)^2+\left(\kappa_2^2\right)^2\right]+\mathrm{K_g}\left[\left(\kappa_3^1\right)^2+\left(\kappa_3^2\right)^2\right]\Bigg\},\end{aligned} \tag{7}$$

where $\mathrm{K_e} \in [0, \infty)$ describes the elongation stiffness of a beam being valid for both orthogonally aligned families of fibers '1' and '2', see Fig. 30. The parameter ε^α, with $\alpha = 1, 2$, is the strain measure of an elongated beam. $\mathrm{K_s}$ describes the shear stiffness of a pivot during torsion with the shear angle $\gamma \in [-\frac{\pi}{2}, \frac{\pi}{2}]$. Note that only torsional deformation of pivots is considered here, no elongation or bending of pivots. The unknown parameters m, and Q are positive constitutive parameters modified from

[44]. K_t describes the twist stiffness of fibers '1' and '2', K_n describes the normal bending stiffness of the fibers, and K_g describes the in-plane bending stiffness of the fibers and is also often referred to as geodesic bending stiffness. The strain measures κ_1^α, κ_2^α, and κ_3^α can be interpreted as the geodesic torsion, the normal curvature and the geodesic curvature of the deformed surface, respectively.

On the basis of this model, an identification of the material parameters, namely K_e, K_s, Q, m, K_t, K_n, and K_g was performed. Notice that quantitative values of parameters K_e, K_s, and K_g were already investigated in [14] and are therefore more or less known after a small correction during the inverse analysis. The unknown material parameters Q, m, K_t, and K_n have been determined by means of the commercial software COMSOL Multiphysics (COMSOL, Inc., Burlington, MA, USA). Parameters Q and m have been set to the value of $Q = m = 1$ while K_t and K_n have been determined. Subsequently, parameters Q and m have been fitted with the best approximation to the experimental values. An overview of the fitted parameters is given in Table 7.

K_e (N/m)	K_s (N/m)	Q (1)	m (1)	K_t (N m)	K_n (N m)	K_g (N m)
96975	13.589	0.266	0.6751	0.00786	0.0266	0.00898

Table 7: Material parameters of a sheared PA sample identified in [3].

3 Publications and their connection

With investigations on the deformation behavior of PSs under shear-loading conditions in the first paper [1], published as **"Gregor Ganzosch, Francesco dell'Isola, Emilio Turco, Tomasz Lekszycki, and Wolfgang H. Müller: Shearing tests applied to pantographic structures. *Acta Polytechnica CTU Proceedings*, 7:1–6, 2017"**, the whole idea of this work came up. The aim of the shearing tests applied to PSs made of polyamide was to investigate the large elastic, non-linear shear-deformation and its resilient material behavior based on five differently sized substructures. While the determination of the material parameters to be used in the numeric simulation was achieved for the case of two-dimensional deformations by means of 2D-DIC, a strange and very extraordinary effect was observed: three-dimensional out-of-plane movements. This buckling effect was not mentioned before in literature and hence was the start of a worldwide collaboration with research-partners from Italy, Poland, France, Germany and the US, respectively. Due to the out-of-plane buckling observed in [1], novel accurate experimental set-ups combined with non-invasive measurement methods had to be developed and designed with the aim to measure those peculiar three-dimensional out-of-plane movements with a sufficient quality. The whole measurement procedure was developed and tested in the second publication [2], published as **"Gregor Ganzosch, Klaus Hoschke, Tomasz Lekszycki, Ivan Giorgio, Emilio Turco, and Wolfgang H. Müller. 3D-measurements of 3D-deformations of pantographic structures. *Technische Mechanik,* 38(3):233–245, 2018"**. 3D-measurements of 3D-deformations of pantographic metamaterials made of polyamide and aluminum were investigated in shearing and torsion tests, respectively. For the first time, quantitative parameter determinations as well as qualitative statements of the out-of-plane movements triggered by shear and torsional loading conditions could be made. Thus, with the help of an inverse-analysis the material parameters based on these 3D-measurements could be determined and be used for a higher gradient model evaluation performed in the third publication [3], published as **"Emilio Barchiesi, Gregor Ganzosch, Christian Liebold, Luca Placidi, Roman Grygoruk, and Wolfgang H. Müller. Out-of-plane buckling of pantographic fabrics in displacement-controlled shear tests: experimental results and model validation. *Continuum Mechanics and Thermodynamics,* 31(1):33–45, 2019"**. Based on the principle of virtual work, local interactions between cylinders and beams could be imitated by means of a model adapted from the Italian colleagues [44]. Beside the experimental

part, the focus of this work was therefore to evaluate the adapted model of a 2D-sheet which was able to deform in 3D. In addition to the second [2] and third publication [3], further samples with different outer dimensions, different loading conditions, and other materials were also taken into account in the last publication [4], published as **"Gregor Ganzosch, Christina Völlmecke, Emilio Barchiesi, and Wolfgang H. Müller. The making and testing of FDM and SLA printed pantographic sheets. *Elasticity and Anelasticity,* Moscow State Univ. Publ., 57—66, 2021"**. Other manufacturing techniques and accompanied experimental investigations enabled a different point of view of the results based on the deformation behavior of PSs with different inner and outer geometries. In contrast to the first three publications, in which polyamide and aluminum were laser sintered [1, 2, 3], other manufacturing methods, namely fused deposition modeling and stereolithography (including different materials, *i.e.*, polylactide and epoxy resin), lead to further deformation characteristics: very large (in-elastic) deformations, which were observed in additionally performed shearing tests as well as small, linear (elastic) deformations, which occurred during extension tests. Moreover, by means of standard axial extension tests the determination of the raw material parameters by means of a laser extensometer was possible and used as input for a classical numerical simulation based on the Cauchy-Boltzmann continuum in the fourth publication [4]. In contrast to the experimental results, which are very similar to the ones calculated in the higher gradient model, classically generated numerical models are only in good agreement with experimental results for small deformations.

4 Publications

4.1 Shearing tests applied to pantographic structures

[1]: Gregor Ganzosch, Francesco dell'Isola, Emilio Turco, Tomasz Lekszycki, and Wolfgang H. Müller: Shearing tests applied to pantographic structures. *Acta Polytechnica CTU Proceedings*, 7:1–6, 2017.

Abstract: With the advancements in 3D printing technology, rapid manufacturing of fabric materials with complex geometries became possible. By exploiting this technique, different materials with different structures have been developed in the recent past with the objective of making generalized continuum theories useful for technological applications. So-called pantographic structures are introduced: Inextensible fibers are printed in two arrays orthogonal to each other in parallel planes. These superimposed planes are inter-connected by elastic cylinders. Five differently sized samples were subjected to shear-like loading while their deformation response was analyzed. Results show that deformation behavior is strong non-linear for all samples. Furthermore, all samples were capable to resist considerable external shear loads without leading to complete failure of the whole structure. This extraordinary behavior makes these structures attractive to serve as an extremely tough metamaterial.

DOI: https://doi.org/10.24352/UB.OVGU-2018-031

Acta Polytechnica CTU Proceedings **7**:1–6, 2017
doi:10.14311/APP.2017.7.0001

available online at http://ojs.cvut.cz/ojs/index.php/app

SHEARING TESTS APPLIED TO PANTOGRAPHIC STRUCTURES

Gregor Ganzosch[a,*], Francesco dell'Isola[b], Emilio Turco[c], Tomasz Lekszycki[d], Wolfgang H. Müller[a]

[a] *TU Berlin, Chair of Continuum Mechanics and Materials Theory, Einsteinufer 5, Berlin, Germany*
[b] *La Sapienza University, Dipartimento di Ingegneria Strutturale e Geotecnica, Via Eudossiana 18, Rome, Italy*
[c] *UNISS, Dipartimento di Architettura, Design e Urabanistica, via Garibaldi 35, Alghero, Italy*
[d] *PAN Warszawa, Instytut Podstawowych Problemów Techniki, ul. Pawinskiego 5B, Warszawa, Poland*
[*] corresponding author: ganzosch@tu-berlin.de

Abstract.

With the advancements in 3D printing technology, rapid manufacturing of fabric materials with complex geometries became possible. By exploiting this technique, different materials with different structures have been developed in the recent past with the objective of making generalized continuum theories useful for technological applications. So-called pantographic structures are introduced: Inextensible fibers are printed in two arrays orthogonal to each other in parallel planes. These superimposed planes are inter-connected by elastic cylinders. Five differently-sized samples were subjected to shear-like loading while their deformation response was analyzed. Results show that deformation behavior is strong non-linear for all samples. Furthermore, all samples were capable to resist considerable external shear loads without leading to complete failure of the whole structure. This extraordinary behavior makes these structures attractive to serve as an extremely tough metamaterial.

Keywords: Pantograpghic structures, shearing tests, generalized continuum theories.

1. Introduction

Micro-Electro-Mechanical-Systems (MEMS) are rapidly becoming smaller. The miniaturization of these systems requires new constitutive equations for describing their mechanical and material behavior (*e.g.*, the deformation pattern of accelerometer sensors in cars). In [1] it was shown that the elastic modulus of epoxy increases if the outer dimensions of the specimen become smaller. The reason for this behavior is hidden in an internal substructure. Such a phenomenon is a.k.a. *size effect* and it characterizes the departure of mechanical behavior from classical continuum mechanics when changing the outer dimension. However, this effect is not limited to the microscopic world. In the literature size effects of different materials of all length scales can be found, starting from investigations on block masonry in the meter-scale [17], continuing with experiments on polymer foams in the millimeter range [10], on to studies on the micrometer-scale in silicon beams [5], and ending finally with bending experiments of nanowires on the nanometer-scale [18].

Another example of intrinsic length scales in complex macroscopic specimens are so-called pantographic structures (see Fig. 1), which were developed and intensively studied by dell'Isola and his team in [2]. Here the length and elastic properties of the constituting trusses in combination with the stiffness of their joints form the internal platform on which their macroscopic deformation behavior relies. Such intrinsic length scale parameters are the true reason behind what is phenomenologically called *size effect*. Classical elasticity theory of continuum mechanics is not able to explain this kind of material behavior because it does not contain an intrinsic length scale. This is why generalized continuum theories must be used to overcome such limits. New material parameters show up during the development of the corresponding constitutive equations. Therefore experiments have to be performed, by means of which these new and unknown parameters can be determined.

Figure 1. Example of a pantographic structure developed by [2].

In recent years, accompanied by the advancements in 3D printing technology, new experimental techniques have been developed with the objective of making generalized continuum theories useful in technology [1–3, 5, 8]. Different experimental set-ups (microscopic as well as macroscopic) when using different materials with complex structures (*e.g.*, static and dynamic bending tests on foams) were developed [1, 2, 5, 8–10, 14]. An experiment was performed on

so-called pantographic structures by [2]. Two families of inextensible fibers, which can also be treated as beams, are 3D-printed in two arrays orthogonal to each other in parallel planes. These are then superimposed. The parallel planes are inter-connected by cylindrical elastic pivots of different diameters and heights. Based on a second gradient continuum model [2–4, 11–15], the deformation behavior of the samples was assessed in numerical simulations during an extension test. Non-linear models with specific intrinsic parameters led to non-classical behavior in the simulation [2]. Based on these results, real macroscopic tensile tests were designed and performed, resulting in an elongation along the direction of the shorter sides of the pantographic samples:

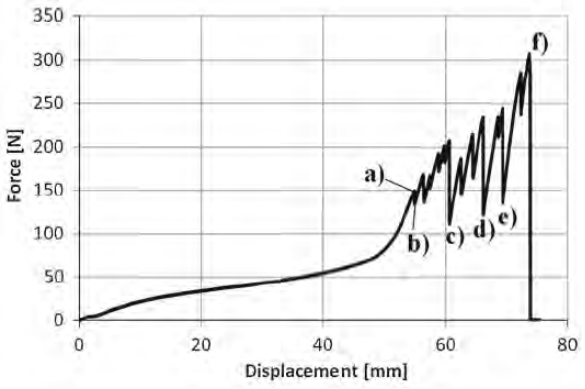

Figure 2. Results of a tensile test applied to a pantographic structure with a pivot height of 0.5 mm and a pivot diameter of 0.9 mm from [2].

Force over displacement is plotted in Fig. 2. The failure of the pantographic lattice is visualized by local minima, marked by b), c), d) and e) in Fig. 2. Each minimum relates to fracture of a beam or a pivot. Surprisingly after one failure within the structure, which was subjected to external loading, the specimen recovers and is able to carry even higher loads than before. The objective of this work is to find out in experiments as to whether the pantographic structures show the same non-linear behavior in shearing tests.

2. Material and Methods

Because of their complex periodic structure, the pantographic samples considered for the investigations in shearing tests were 3D-printed. Polyamide powder was used as raw material. 3D-models were generated by using a commercial CAD software and saving them in STL format file, which was then used as input for the 3D printer. Five variations of specimens with different inner geometries but equal material densities were investigated. The pantographic structure consists of rectangular beams and cylindrical pivots. A schematic shows different beam and pivot parameters in Fig. 3. Details can be found in Tab. 1. The inner parameters of the pivots are kept constant (except for the diameter of sample E with $d = 3.00$ mm, see

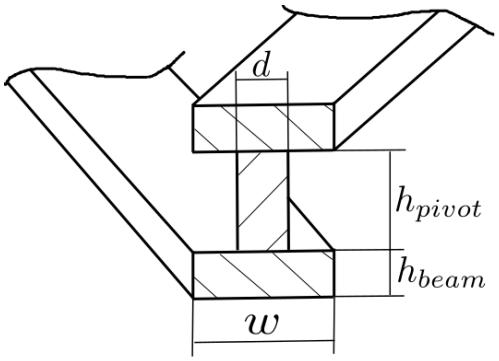

Figure 3. Schematic cross-section of a periodic cell of a pantographic structure.

Sample	w	h_{beam}	d	h_{pivot}
A	1.00 mm	1.00 mm	0.90 mm	1.00 mm
B	1.60 mm	1.00 mm	0.90 mm	1.00 mm
C	1.60 mm	1.60 mm	0.90 mm	1.00 mm
D	2.25 mm	1.60 mm	0.90 mm	1.00 mm
E	2.25 mm	1.60 mm	0.90 mm	3.00 mm

Table 1. Overview of five specimens with different beam and pivot parameters.

Tab. 1), so that investigations of pantographic structures will focus on different beam parameters and their influence on the deformation behavior during shear tests. The outer dimension of every specimen is kept constant (length= 204 mm, width= 70 mm).

An overview of the whole experimental setup used for the shear tests on planar pantographic sheets is shown in Fig. 4.

Figure 4. Experimental setup during shear deformation: Camera and illumination devices on the left, pantographic sample mounted in an MTS Tytron 250 testing machine in the middle, interface of control software on the right.

An MTS Tytron 250 testing-device controlled by the software Stationsmanager V 3.14 was used during the shearing tests. Applied force was measured by a load cell attached to the device, which is able to record axial forces in a range of $N = \pm 250$ N. The displacement was imposed horizontally on the top of the specimen with a loading rate of $v = 15$ mm/min. The experiments were displacement-controlled using a DC-linear motor in combination with a spindle. Displacement was measured and monitored by a device-own encoder unit. Almost frictionless movement was

(A) . Mounted sample A before deformation.

(B) . Deformed sample A directly before first failure occurs.

(C) . Sample A after complete failure.

FIGURE 5. Shear deformation of sample A.

achieved by using an air-film-bearing. External vibration was avoided by using a massive substructure and by arranging the system horizontally. Additionally to force-displacement recording, pictures were taken (0.25 pictures/second) by means of a commercial Canon EOS 1000D camera with a resolution of 4272×2848 pixels. Free software ImageJ 1.50i was used to evaluate image data. Open source software SciDAVis 1.14 was used for preparation, manipulation, and evaluation of acquired machine data.

Fig. 5 shows the deformation of sample A before, during, and after the shearing test.

3. RESULTS

Results of all five samples are visualized in Fig. 6 with the help of a force-displacement diagram. Local minima in Fig. 6 show a failure of a beam or a pivot. It can be recognized that all samples show different and pronounced non-linear behavior. In order to visualize the results for a discussion, the graph of each sample is plotted separately, starting with sample A in Fig. 7, and ending with sample E in Fig. 11.

In sample A the first failure occurs at $F_A = 26.0$ N.

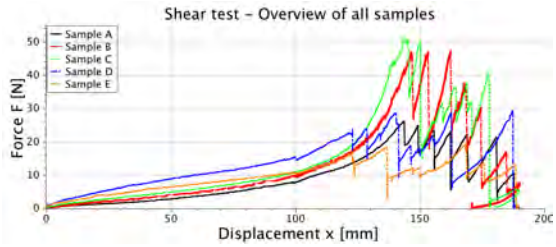

FIGURE 6. Raw-data of all samples; force F is plotted over displacement x.

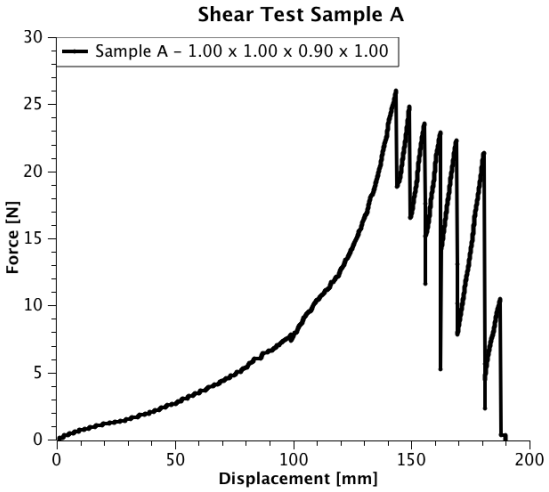

FIGURE 7. Raw-data of sample A; force F is plotted over displacement x.

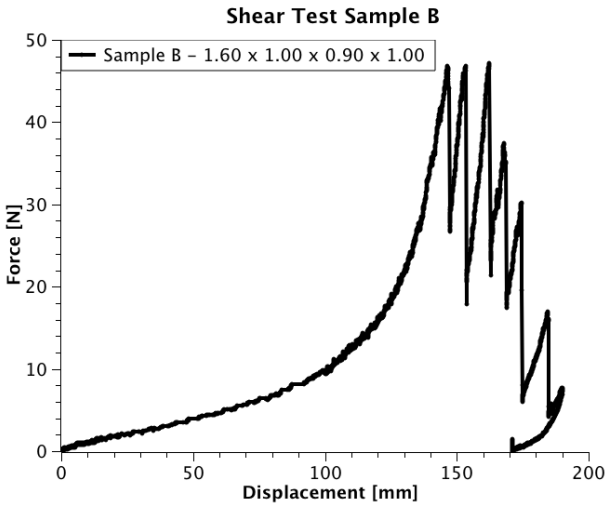

FIGURE 8. Raw-data of sample B; force F is plotted over displacement x.

Surprisingly, samples B ($F_B = 46.9$ N) and C ($F_C = 50.5$ N) are able to resist the highest loads. Sample D resists until $F_D = 23.9$ N. Sample E shows the lowest strength and failure occurs at about $F_E = 16.8$ N. In sample A and B, a beam failure occurs on the lower left corner (shown for sample A in Fig. 12). In contrast to the lower right corner, where just low deformation occurs, the beams at the lower left corner experience a large elongation between the pivots. In

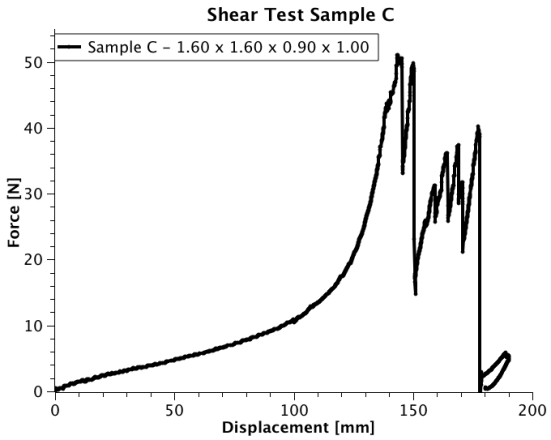

Figure 9. Raw-data of sample C; force F is plotted over displacement x.

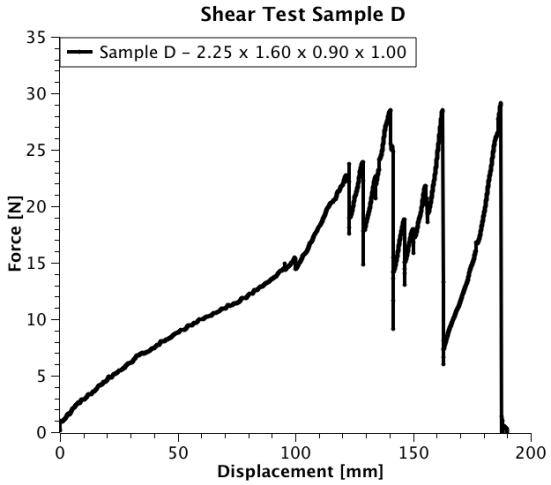

Figure 10. Raw-data of sample D; force F is plotted over displacement x.

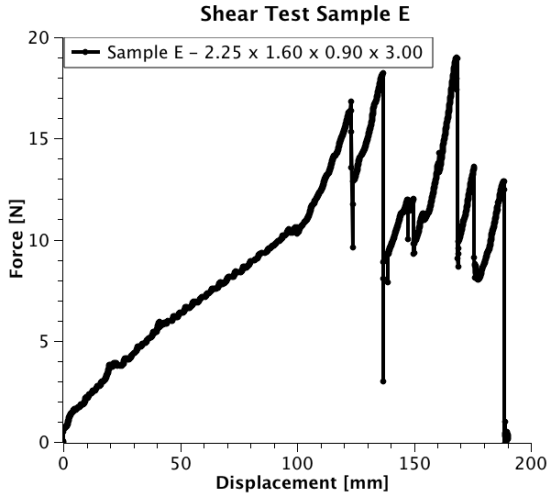

Figure 11. Raw-data of sample E; force F is plotted over displacement x.

this region, bending energy of fibers is concentrated leading to failure of a beam. First failure of sample C, D, and E is quite different (shown for sample C in Fig. 13). Obviously, bending energy of fibers is so high in the middle-left that pivots in this region (marked by the circle in Fig. 13) start to separate from the beam structure. Notice, that the variation of inner parameters leads to different deformation and rupture behavior. The influence of inner parameters on the material behavior of the specimen will be described and discussed.

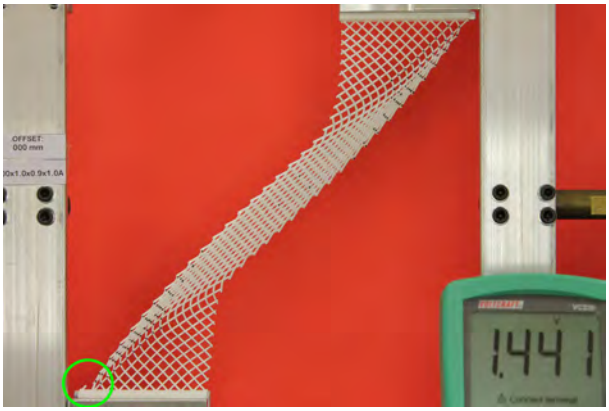

Figure 12. Deformed sample A directly after first failure occurs, region marked by the circle.

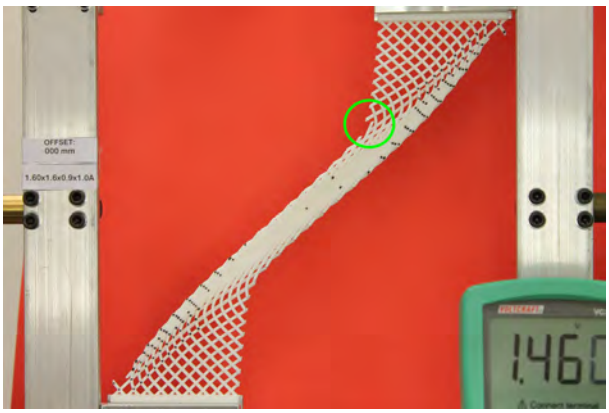

Figure 13. Deformed sample C directly after first failure occurs, region marked by the circle.

By enlarging the width of the beams in the pantographic structure from sample A ($w = 1.00$ mm) to sample B ($w = 1.60$ mm), the resistance to shear deformation increases by almost 80%. This enlargement has a very high influence on the strengthening of this structure.

By enlarging the height of the beams from sample B ($h_{beam} = 1.00$ mm) to sample C ($h_{beam} = 1.60$ mm), the resistance to shear deformation increases by just 7.7%. This is a much smaller influence compared the one from sample A to B mentioned before. But still sample C is able to carry the highest shear load until the first failure occurs ($F_C = 50.5$ N).

By enlarging the width of the beams from sample C ($w = 1.60$ mm) to sample D ($w = 2.25$ mm), the resistance to shear deformation decreases by 52.7%.

This observation is contrary to our assumptions and indicates an upper limit value for the width of beams between 1.60 mm $\leq w <$ 2.25mm.

Finally, by enlarging the height of the pivots from sample D ($h_{pivot} = 1.00$ mm) to sample E ($h_{pivot} =$ 3.00 mm), the resistance to shear deformation decreases by 29.7%. This can be explained by the higher lever arm between the beams resulting in a high torque which then leads to failure.

Notice that complete failure for samples A, D, and E occurs at a deformation of about $x = 190$ mm. Absolute structural failure of the flexible sample B and C could not be investigated due to movement-limitations of machine-axis. This is also the reason for unloading curves in sample B and C, which occurred during the removal procedure of the samples from testing device. Interestingly, sample A, B, and C show a strong non-linear increase of their slopes before first failure occurs. This is not the case for sample D and E with higher values for the width of beams ($w = 2.25$ mm). Furthermore, samples B, D, and E are able to carry even higher loads after first failure. Because of the complex geometry, the beams reorganize themselves resulting in a higher resistance to shear loading. This behavior was also observed during tensile tests for the case of uni-axial loading as afore-mentioned in [2].

Sample	x_m [mm]	x_i [$\pm$1 mm]	$\triangle x$ [$\pm$1 mm]
A	143.96	142.47	1.49 (1.04%)
B	142.91	141.50	1.41 (0.99%)
C	145.71	145.29	0.42 (0.29%)
D	122.96	122.13	0.83 (0.68%)
E	123.77	123.49	0.28 (0.23%)

TABLE 2. Listed values of displacement based on image data (x_i) and based on machine data (x_m) at the time when first breakage of the specimen occurred. Difference of displacement between machine data and image data ($\triangle x$) is presented in the last column.

By comparing image data with machine data, no significant difference in displacement was observed (see Tab. 2). Sample A shows the highest difference between displacement obtained from machine data and main displacement obtained from image data($\triangle x_A = 1.04\%$), sample E shows the lowest one ($\triangle x_E = 0.23\%$). Note that displacements captured by the camera are smaller than the ones obtained from the testing device. We assume, that one reason for this observation is the compliance (inverse of stiffness) of the testing device and its structure: deformation of clamping jaws and mounting support influences the real displacement. Another reason is based on the uncertainty of image data: pictures were taken every 4 seconds (as described in Sect. 2), in which the loading-axis was able to travel up to 1 mm (error of $\pm$1 mm in second column of Tab. 2, x_i). This results in a discrepancy between real and measured displacement.

Furthermore it has to be mentioned that image data was just able to capture the deformation behavior in a two dimensional plane. But during the experiments it was observed that the structure was also deforming in the third direction (out-of-plane). This buckling-like behavior varied strongly for each sample. Highest out-of-plane-movements were observed in experiments involving sample A and B (up to 19 mm). Sample C, D, and E showed very weak out-of-plane-movements or even none. The investigation of this effect is strongly recommended in further research projects. Manufacturing process (rapid prototyping) may have a big influence on the material behavior as well (*e.g.*, direction of printing or thickness of layer) and should also be part of future investigations. Notice, that each sample was just measured once. To increase the quality of results, each experiment should be repeated under exactly the same experimental conditions. Acquired data should then be compared among each other.

4. Conclusions

Deformation behavior of various pantographic structures with different inner parameters was investigated in shearing tests. We showed that the variation of inner parameters (beam and pivot dimensions) have a deep impact on the material behavior. All samples behaved non-linearly and were capable to resist considerable external shear loads without leading to complete failure of the whole structure. Because of the complex geometry beams and pivots reorganize themselves resulting in an higher resistance to outer load, so that even higher loads can be carried after failure (see sample B, D, and E). An aim for further investigations should be to provide a better predictability of structural failure behavior by manipulating the inner parameters in a way that all force-peaks should be at one level. This would make the deformation behavior of the structure more predictable and would contribute to make these structures available for application in technology.

Real experiments are quite involved. Thus, the obtained results shall be used to develop further simulation models as shown in [3] or [14, 15]. It is also possible to investigate the influence of inner parameters on the material behavior in a numerical analysis [14, 16]. However, these models are based on many simplifications and restrictions so that a true validation would still be challenging and should be investigated further.

As afore-mentioned in Sect. 3, investigated lattices were just examined in context with two-dimensional planar structures (neglect of twist or buckling). Other forms, such as cylinders or rectangles, would contribute to three-dimensional stability and would help to make these structures useful for technology. In summary one may say that the combination of strength and lightness makes these structures attractive to serve as an extremely tough metamaterial (*e.g.*, airplane frame parts or artificial bone scaffolds).

List of symbols

F Force [N]
x Displacement [mm]
x_m Displacement based on machine data [mm]
x_i Displacement based on image data [mm]
$\triangle x$ Difference between x_m and x_i [mm]
w Width [mm]
d Diameter [mm]
h_{beam} Beam-height [mm]
h_{pivot} Pivot-height [mm]
v Velocity [mm]

References

[1] Liebold, C., Müller, W.H. *Applications of higher-order continua to size effects in bending: Theory and recent experimental results.* Generalized Continua as Models for Classical and Advanced Materials, Springer International Publishing, pp. 237-260, 2016

[2] dell'Isola, F., Lekszycki, T., Pawlikowski, M., Grygoruk, R., Greco, L. *Designing a light fabric metamaterial being highly macroscopically tough under directional extension: First experimental evidence.* Zeitschrift für angewandte Mathematik und Physik, ZAMP, 66(6), pp. 3473-3498, 2015

[3] dell'Isola, F.,Della Corte, A., Giorgio, I., Scerrato, D. *Pantographic 2D sheets: Discussion of some numerical investigations and potential applications.* International Journal of Non-Linear Mechanics, Elsevier, 80, pp. 200-208, 2016

[4] Placidi, L., Andreaus, U., Della Corte, A., Lekszycki, T. *Gedanken experiments for the determination of two-dimensional linear second gradient elasticity coefficients.* Zeitschrift für angewandte Mathematik und Physik, ZAMP, 66(6), pp. 3699-3725, 2015

[5] Liebold, C. *Größeneffekt in der Elastizität.* Dissertation, Technische Universität Berlin, Germany, 2015

[6] Liebold, C., Müller, W.H. *Comparison of gradient elasticity models for the bending of micromaterials.* Computational Materials Science. Elsevier, pp. 52-61, 2016

[7] Liebold, C., Müller, W.H. *Measuring material coefficients of higher gradient elasticity by using AFM techniques and Raman-spectroscopy.* Generalized continua as models for materials, Springer-Verlag Berlin Heidelberg, pp. 255-271, 2013

[8] Ganzosch, G., Müller, W.H. *Experimental techniques applied to generalized continuum theories - A state-of-the-art report.* Proceedings of the XLIV Summer School-Conference. 44, pp. 149-161, 2016

[9] Lam, D. C. C., Yang, F., Chong A. C. M., Wang, J., Tong, P. *Experiments and theory in strain gradient elasticity.* Journal of the Mechanics and Physics of Solids. 51(8), pp. 1477-1508, 2013

[10] Lakes, R., Drugan, W.J. *Bending of a Cosserat elastic bar of square cross section: Theory and experiment.* Journal of Applied Mechanics, 82(9), pp. 2-8, 2015

[11] dell'Isola, F., dAgostino, M. V., Madeo, A., Boisse, P., Steigmann, D. *Minimization of shear energy in two dimensional continua with two orthogonal families of inextensible fibers: the case of standard bias extension test.* Journal of Elasticity, 122(2), pp. 131-155, 2016

[12] Pipkin, A.C. *Plane Traction Problems for inextensible Networks.* Q.J. Mech. Appl. Math., 34(4), pp. 415-429, 1981

[13] Rivlin, R.S. *Plane Strain of a Net formed by inextensible Cords.* Collected Papers of RS Rivlin, Springer Berlin, pp. 511-534, 1997

[14] Turco, E., dell'Isola, F., Rizzi, N.L., Grygoruk, R., Müller, W.H., Liebold, C. *Fiber rupture in sheared planar pantographic sheets: Numerical and experimental evidence.* Mechanics Research Communications, Elsevier, 76, pp. 86-90, 2016

[15] Turco, E., dell'Isola, F., Cazzani, A., Rizzi, N.L. *Hencky-type discrete model for pantographic structures: numerical comparison with second gradient continuum models.* Zeitschrift für angewandte Mathematik und Physik, ZAMP, 67(85), pp. 01-28, 2016

[16] Abali, B.E., Müller, W.H., Eremeyev, V.A. *Strain gradient elasticity with geometric nonlinearities and its computational evaluation* Mechanics of Advanced Materials and Modern Processes, 1(1), pp. 01-11, 2015

[17] Pau, A., Trovalusci, P. *Block masonry as equivalent micropolar continua: The role of relative rotations.* Acta Mechanica, 223(7), pp. 1455-1471, 2012

[18] Jing, G.Y., Duan, H.L., Sun, X.M., Zhang, Z.S., Xu, J., Li, Y.D., Wang, J.X., Yu, D.P. *Surface effects on elastic properties of silver nanowires: Contact atomic-force microscopy.* Physical Review B, 73, pp. 01-06, 2006

4.2 3D-measurements of 3D-deformations of pantographic structures

[2]: Gregor Ganzosch, Klaus Hoschke, Tomasz Lekszycki, Ivan Giorgio, Emilio Turco, and Wolfgang H. Müller. 3D-measurements of 3D-deformations of pantographic structures. *Technische Mechanik,* 38(3):233–245, 2018.

Abstract: Samples of differently sized so-called pantographic structures are subjected to large deformation loading tests up to rupture, while their response to the deformation is recorded by an optical 3D-measurement system. Digital image correlation is used to calculate the deformation that took place perpendicular to the reference plane by the help of a four-camera system. Results show that the deformation behavior is strongly non-linear and that the structures are capable to perform large (elastic) deformations without leading to complete failure.

DOI: https://doi.org/10.24352/UB.OVGU-2018-031

DOI: 10.24352/UB.OVGU-2018-031 TECHNISCHE MECHANIK, 38, 3, (2018), 233 – 245
submitted: December 11, 2017

3D-Measurements of 3D-Deformations of Pantographic Structures

G. Ganzosch, K. Hoschke, T. Lekszycki, I. Giorgio, E. Turco, W. H. Müller

Samples of differently sized so-called pantographic structures are subjected to large deformation loading tests up to rupture, while their response to the deformation is recorded by an optical 3D-measurement system. Digital image correlation is used to calculate the deformation that took place perpendicular to the reference plane by the help of a four-camera system. Results show that the deformation behavior is strongly non-linear and that the structures are capable to perform large (elastic) deformations without leading to complete failure.

1 Introduction

The progress in 3D-printing technology enables the development of new structures with extraordinary geometric and mechanical characteristics (dell'Isola et al., 2016d). In combination with specially treated materials, a new class of intelligent structures was developed (dell'Isola et al., 2015b, 2016a,c). So-called Pantographic Structures (PSs) were conceived by dell'Isola, Lekszycki and their co-workers (Battista et al., 2017; Cuomo et al., 2017; dell'Isola et al., 2017, 2016b; Giorgio et al., 2016; Placidi et al., 2016; Spagnuolo et al., 2017; Turco et al., 2017, 2016c) with the aim to find a planar body that can be enlarged without damage up to about 50 percent and still remains in the elastic range. The models proposed to describe the behavior of these kind of materials fall within the general framework of micropolar anisotropic elasticity (Auffray et al., 2015; Eremeyev and Pietraszkiewicz, 2016), and can be reduced to second gradient materials (dell'Isola et al., 2015c; Pideri and Seppecher, 1997; Dos Reis and Ganghoffer, 2012; AminPour and Rizzi, 2016; Della Corte et al., 2016) by adding proper constraints. They can be interpreted as particular cases of shells, bi-dimensional foams or, from a more general point of view, as functionally graded materials or meta-materials, if the geometry of elementary constituents is suitably designed to meet given requirements (Altenbach and Eremeyev, 2009a,b, 2014; Hendy and Turco, 2008; Turco, 1998; Alibert et al., 2003; De Masi et al., 2008, 2009). Those newly introduced structures share a very similar kinematics to woven fabrics. Therefore theoretical tools developed for reinforced composites can also be applied successfully to PSs, see, e.g., (dell'Isola and Steigmann, 2015; Steigmann and dell'Isola, 2015; Misra et al., 2015; Zeidi and Kim, 2017; Alsayednoor et al., 2017; Harrison, 2016; Launay et al., 2008; Selvadurai and Nikopour, 2012).

In order to investigate the deformation behavior of PSs in the best possible way, an optical measurement technique, to be more precise, Digital Image Correlation (DIC), will be used. This non-invasive technique is able to detect and to measure a three dimensional deformation of a surface. This pattern, in which wrinkling occurs, can also be spotted in biological systems as, e.g., the skin (Lejeune et al., 2016). Uniaxial tests, shearing tests, and torsion tests were applied to PSs. Based on experimental data the extraordinary deformation behavior of PSs will be discussed.

2 Material and Methods

Because of their complex periodic structure, the pantographic samples considered for the investigations in tension, shear, and torsion tests were manufactured with the help of a 3D-printer. Polyamide as well as aluminum powder were used as raw materials. The PS consists of rectangular beams and cylindrical pivots (see Fig. 1). 3D-models have been generated by using the commercial CAD software SolidWorks® (Dassault Systèmes SolidWorks Corporation, Waltham, MA 02451). STL file was transformed to a GCODE and has been used as input for the 3D-printer.

For the production of the specimen made out of polyamide (PA2200) a Formiga P 100® (EOS GmbH, Munich, Germany) Selective Laser Sintering (SLS) 3D-printer was used at the University of Technology, Warsaw, Poland. The aluminum specimen was manufactured on an EOS M 400® 3D-printer with Direct Metal Laser Sintering (DMLS) from AlSi10Mg metal powder with a 1 kW laser source at Fraunhofer EMI, Freiburg, Germany. Even

small deviations during the printing process lead to breakage and abortion of the process or pre-damage in the case of filigree structures, such as PSs. In comparison to the plastic process, for the metal fabrication a special support structure and a complicated elaborated laser exposure strategy was employed in order to avoid thermal distortions due to the higher laser powers and energy input. The specimens were positioned at a special angle with regard to the building direction in order to minimize the cross-sectional area of exposure in the layer-wise process. This very angle was also chosen in a way that the arrangements of beams and pivots ensured self-supporting. The mounting area was supported. A contour based arrangement of laser tracks was used to minimize transient deviations of the energy input due to the inertia in the optical scanning system. That approach fits the geometric characteristic of the slender beams better. In Fig. 3 aluminum specimens are shown after the small batch production. Prior to support removal and separation from the building plate, a stress relief heat treatment (2 h at 300 °C) was employed for this configuration. Deviations due to thermal stresses were prevented. Heat treatment also results in ductile behavior of the material (Mower and Long, 2016) in comparison to the as-built properties.

Figure 1: Polyamide sample of a PS developed by (dell'Isola et al., 2015b).

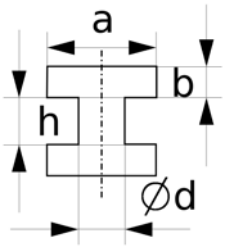

Figure 2: Example of a periodic unit cell of a PS: a and b describe width and height of a beam, Ø d and h describe diameter and height of a pivot.

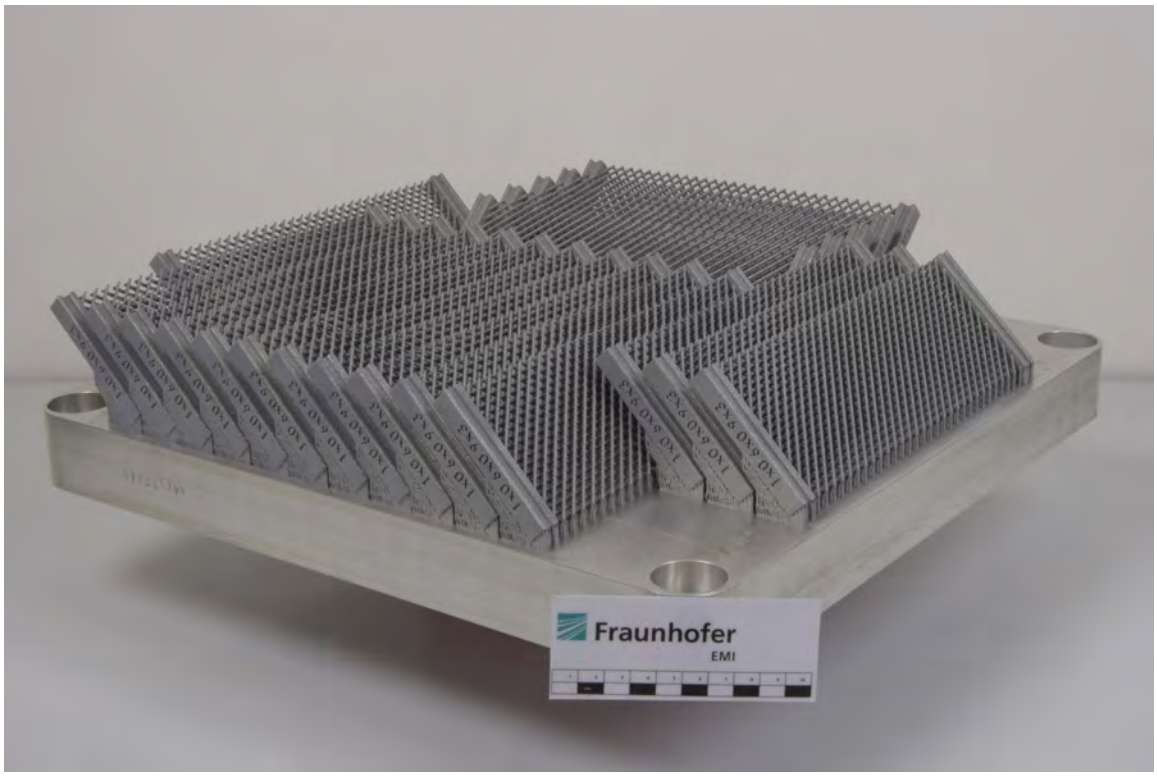

Figure 3: PSs made out of aluminum, manufactured at EMI, Freiburg, Germany.

Specimens with different internal geometries were investigated. A schematic outline of the substructure is presented in Fig. 2. It shows the different pivot parameters and beam parameters. All values of these parameters for each to be tested specimen are given in Tab. 1. The outer dimensions of all sheets are $210\,\text{mm} \times 70\,\text{mm}$. The main aim of this work is to find out if it is possible to measure surface deformation with the help of the 3D-DIC system. Furthermore, we will discuss different material parameters and their influence on the deformation behavior. Note that we will focus on shearing and torsion experiments, because out-of-plane movement was not measured in

regular tension tests. Uniaxial experiments on PSs were discussed intensively in (dell'Isola et al., 2015b, 2016a).

Sample	Material	a [mm]	b [mm]	Ø d [mm]	h [mm]
A	Polyamide	1.0	1.0	0.9	1.0
B	Aluminum	1.0	0.6	0.9	3.0

Table 1: Overview of investigated specimens: list of different materials and geometry parameters, see Fig. 2.

An overview of the experimental setup of a shearing test is shown in Fig. 4. Fig. 5 shows the setup of a torsion test. The schematic setup of the device is presented in Fig. 6. A `Zwick Z010`® testing-device, controlled by the software `TestExpert`®, was used during all tests.

The resultant applied axial force was measured by a device-own load cell (`Zwick-Serie Xforce`®). The force transducer is able to record axial forces in the range of about $\pm\,10{,}000\,\mathrm{N}$, whereas the accuracy at $20\,\mathrm{N}$ is 0.1%. The displacement Δx was controlled vertically. The upper traverse-part of the tensile-to-shear adaption-device (see Fig. 4 and Fig. 6) is fixed horizontally and vertically, while the lower part can be linearly moved in the vertical direction. The velocity for the shear tests has been set to be $15\,\mathrm{mm/min}$, what is quite slow for such tests (displacement-controlled; quasi-static). The displacement itself was recorded and monitored by a device-own encoder unit with an accuracy of $\pm\,2.0\,\mu\mathrm{m}$. For the torsion tests a device-own torque sensor (`Zwick-Serie M`®) was applied on the very fixed bottom of the lower traverse, while the torsion was induced on the top of the mounting with 1° /min on the upper traverse-part of the torque adaption-device (see Fig. 5 and Fig. 6). The torsion transducer is able to record moments up to $20\,\mathrm{Nm}$ and resists maximal axial forces up to $\pm\,5{,}000\,\mathrm{N}$.

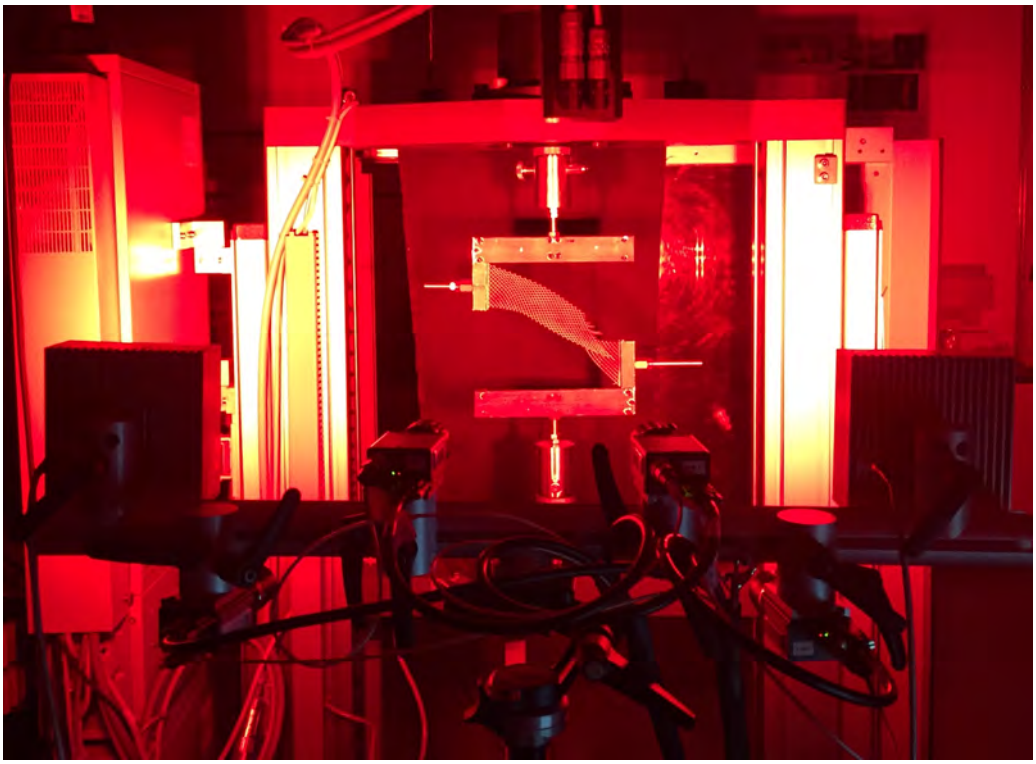

Figure 4: Experimental setup of a shear test: PS after rupture. PS is mounted into the tensile-to-shear adaption-device, which is connected to the Zwick loading machine. The upper adaption is fixed. The lower traverse can move vertically. The Dantec camera and illumination system can be recognized in the front of the figure.

A non-invasive optical measurement device `Q-400` (Dantec Dynamics GmbH, Ulm, Germany) was installed to record the state of three dimensional deformation of the surface of a sheet by the help of four cameras as shown in Fig. 4 (front) and in Fig. 5 (right). A more-than-one camera system is able to recognize the 3D-motion within overlapping regions of the image sections (in our case four cameras). Due to the large deformation applied here, this region of overlapping was doubled, in order to capture the whole deformation process. To enable the software of image correlation to separate small surface areas (so-called facets) and because of lack of contrast, the surfaces of all specimens have been sprayed in a speckled pattern using an airbrush system and the acrylic-based waterproof

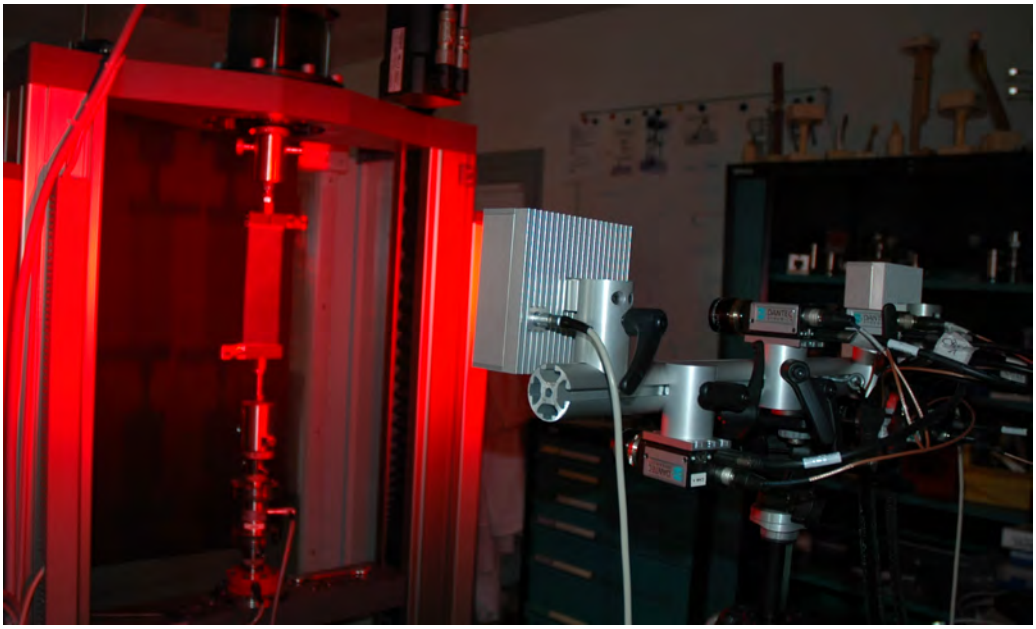

Figure 5: Experimental setup of a torsion test: PS during deformation. PS is mounted into the torsion device. The upper adaption can rotate. The lower traverse is fixed. Load-cell and torque-sensor can be recognized at the bottom. Four cameras and two illumination devices are fixed horizontally about 120 cm in front of the loading device.

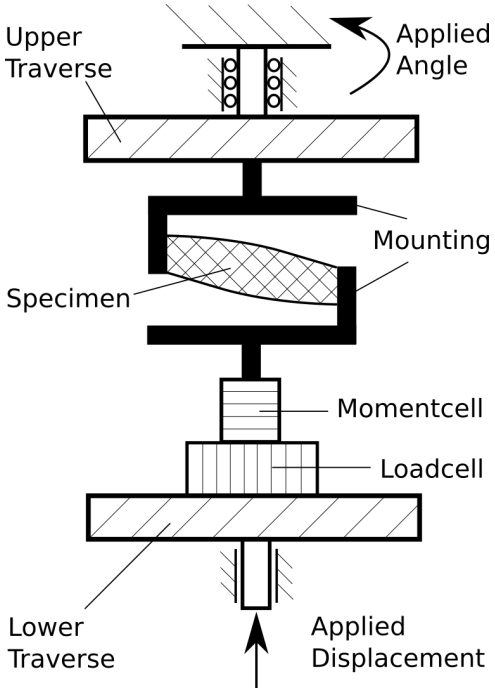

Figure 6: Schematic setup of the loading-device: Moment-cell and load-cell are fixed on the lower traverse, which is able to apply a vertical displacement. A rotation is applied aroung a fixed vertical axis from the upper traverse.

ink (Molotow One4All, Feuerstein GmbH, Lahr, Germany). During the deformation process, pictures have been taken via direct TTL-signal every 2 seconds by means of the afore mentioned commercial camera system with a resolution of about $1{,}600 \times 1{,}200$ pixels. This way, we were able to synchronize each picture to the related force-value in real time. Figure 7 shows three exemplary 2D-pictures of one of the cameras during shear test up to rupture for sample **B**. Figure 8 shows six exemplary 2D-pictures of one camera during the torsion test up to rupture for sample **B**. By means of a calibration procedure of the camera setup, the commercial software `Istra4D`® is able to re-calculate a three dimensional surface deformation.

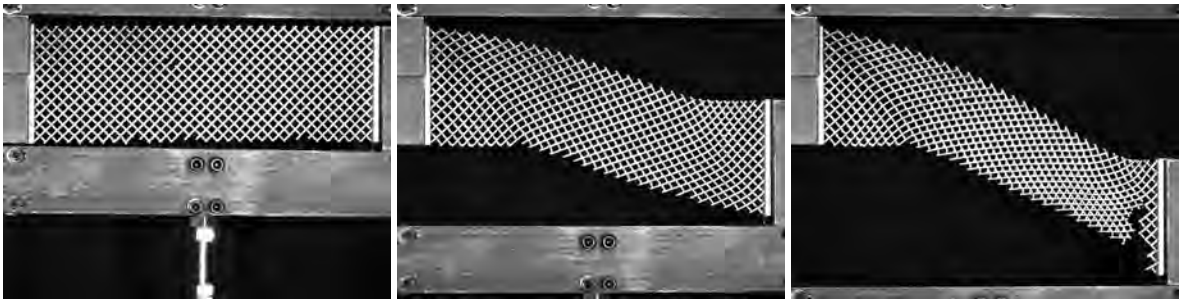

Figure 7: Exemplary raw pictures of sample **B** up to rupture during shear-load after 0 mm, 45 mm, and 80 mm shear-displacement. Rupture occurs next to the mounting in the lower right corner of the sample.

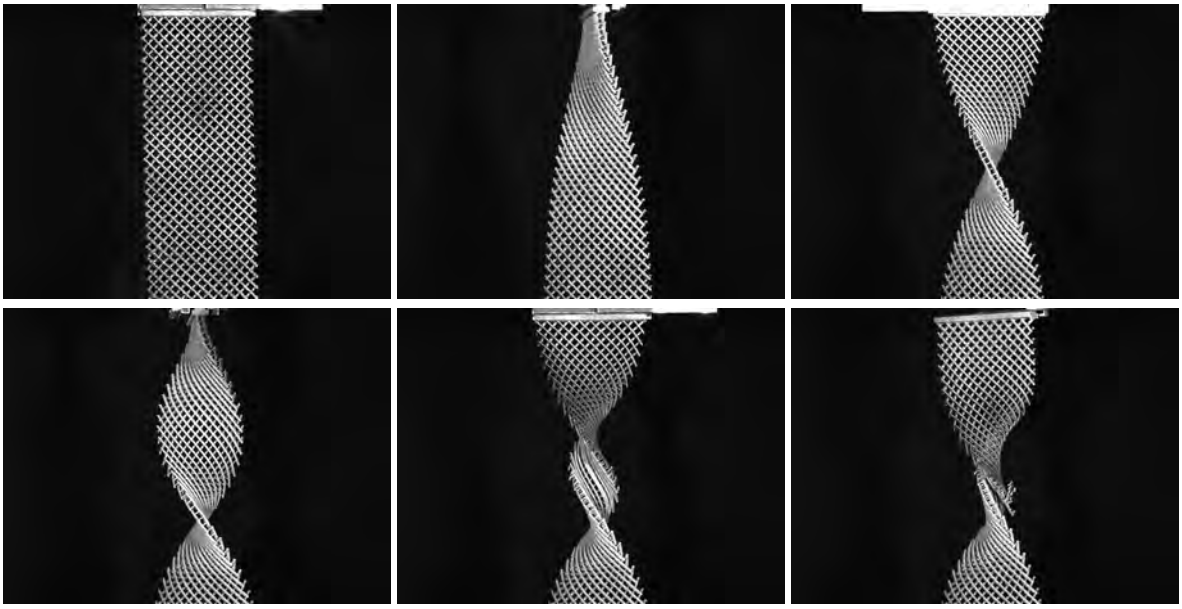

Figure 8: Exemplary raw pictures of sample **B** about every $90°$ (for the first five sequences) up to rupture during torsion-load. Rupture of beams can be recognized in the middle of the sheet.

Originally, the adaption-device was equipped with linear-guides, in order to ensure a parallel movement of the upper and lower part in the shearing tests. Nevertheless, the present measurements have been performed without the linear-guides in order to improve the friction induced noise signals. Results from the DIC measurements indicated that the vertical parallelism is still given, even for high loads acting on the aluminum specimen. After evaluating the 3D-data, only a minor out-of-plane movement of the lower part of the shear-adapter has been recognized and taken into account for sample **B**.

3 Results

In order to obtain scalar results for an out-of-plane displacement of a sheet, a point in a single facet (a sub-area of image correlation) has been selected for each sample. This point is located in the place where maximal out-of-plane movement has been presumed. Due to the large deformations, some facets will move out of the optical focus, which may cause the image correlation to abort. Furthermore, image correlation is aborted, when a sudden rupture occurs in between the shutter releases, so that the facets to be correlated are displaced laterally too much. For these reasons some of the facets in Fig. 11 and some plots in Fig. 9 are incomplete.

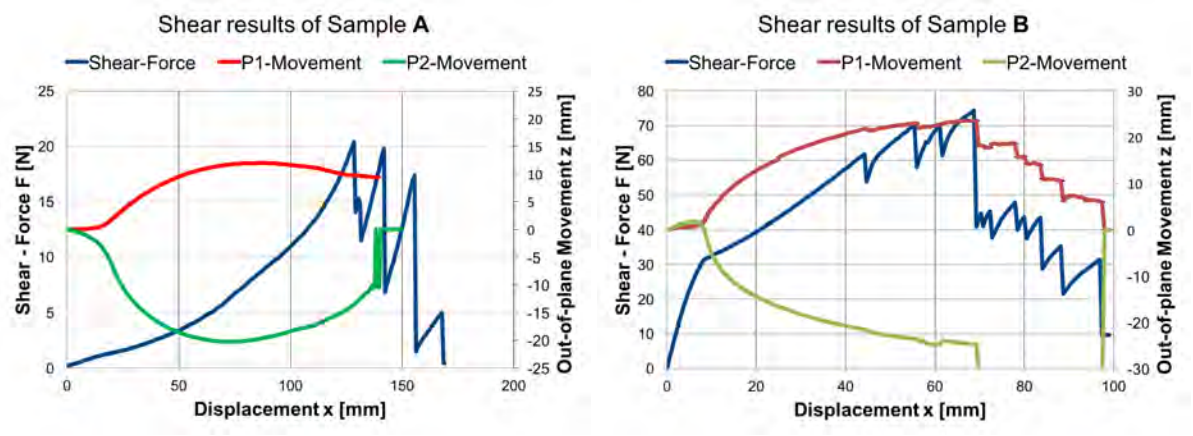

Figure 9: Shear-force/displacement diagram and out-of-plane movement/displacement diagram of sample **A** (left picture) and sample **B** (right picture) during shear-load.

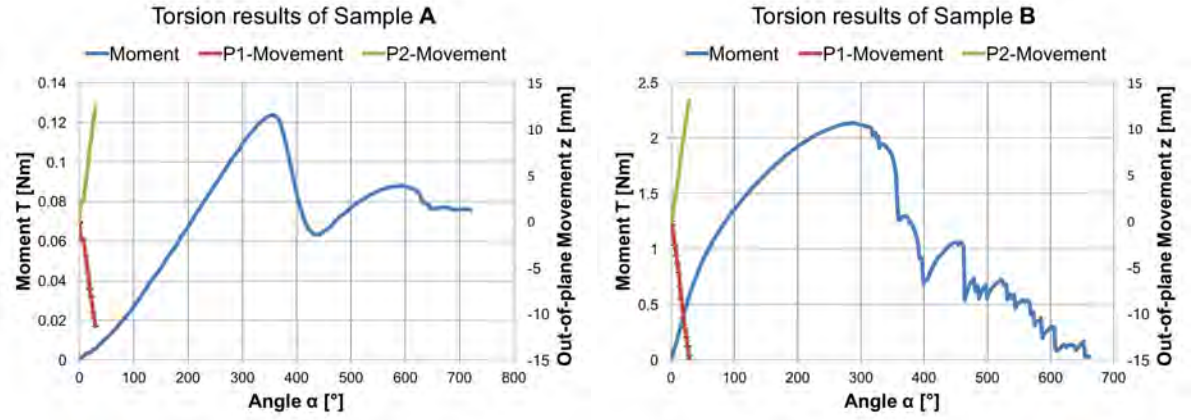

Figure 10: Moment/angle diagram and out-of-plane movement/angle diagram of sample **A** (left picture) and sample **B** (right picture) during torsion.

The summary of the experimental results of both samples, the polyamide one as well as the aluminum one, are visualized in Fig. 9 for the case of shearing, showing the plots for the shear-force vs. shear-displacement (left ordinate), as well as the out-of-plane vs. the shear-displacement (right ordinate). In Fig. 10 experimental results of both samples for the case of torsion are plotted, showing the plots for the moment vs. twist-angle (left ordinate), as well as the out-of-plane vs. the twist-angle (right ordinate). Local minima in all plots describe failure of a beam or a pivot. All samples show different and pronounced non-linear curves.

In order to demonstrate the data acquisition, Fig. 11 shows the processed 3D-data of both samples during the shear deformation. Regrading the data acquisition for the case of torsion, Fig. 12 shows the processed 3D-data of both samples during the torsional deformation. All data was generated without smoothing.

Furthermore, Table 2 shows the maximal out-of-plane displacement values per sample for shearing as well as for torsion, within the valid measurement ranges.

Sample	Maximal out-of-plane displ. in shearing-test [mm]	Maximal out-of-plane displ. in torsion-test [mm]
A	-20.31	12.39
B	-23.29	-16.27

Table 2: Maximal out-of-plane values for shearing and torsion.

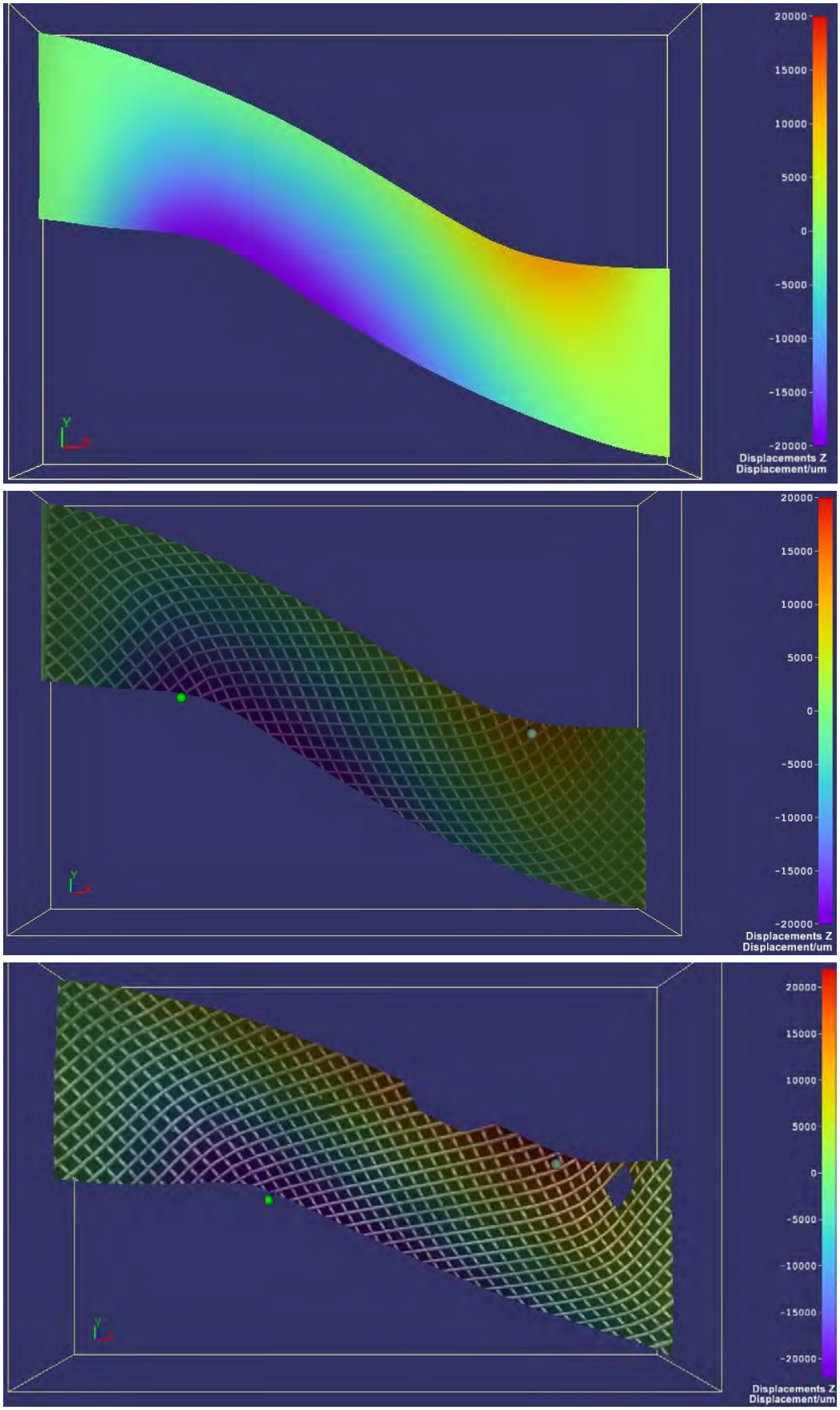

Figure 11: 3D-evaluation-image during the shearing tests: red areas in the upper right part of the sheet show out-of-plane movement in the positive direction, blue areas in the lower left part of the sheet show negative movements. Pure data of sample **A** (upper figure). Overlay with real image of sample **A** (middle figure). Overlay with real image of sample **B** (lower figure). A symmetric deformation can be observed.

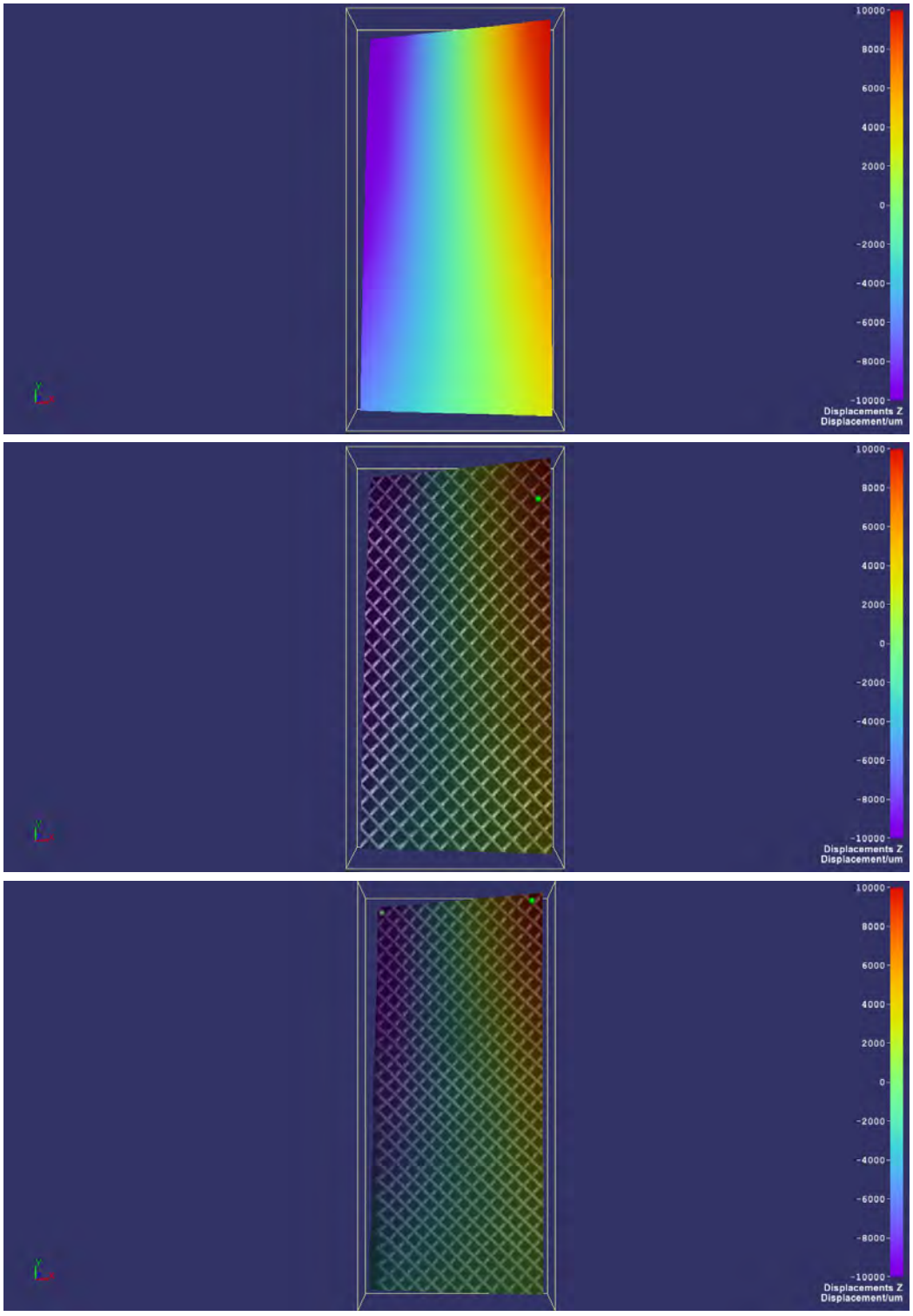

Figure 12: 3D-evaluation-image during the torsion tests: red areas in the upper right corner show out-of-plane movement in the positive direction, blue areas in the upper left corner show negative movements. Pure data of sample **A** (upper figure). Overlay with real image of sample **A** (middle figure). Overlay with real image of sample **B** (lower figure). A symmetric deformation can be observed.

4 Discussion and Conclusion

It is possible to measure out-of-plane movement of 3D-deformation applied to PSs. Furthermore, we confirmed the presumed non-linear deformation behavior, which was also measured in our preliminary work (dell'Isola et al.,

2015b; Ganzosch et al., 2017). By comparing the shear-forces of sample **A** and sample **B** in Fig. 9 (blue curve), it can be recognized that the aluminum sample **B** is able to resist outer loads about three times higher than the polyamide one until first rupture occurs. Although parameters of sample **B** are smaller than the ones of sample **A** (see Table 1), sample **B** resists higher load conditions because of the stiffer material behavior of aluminum. Both samples show non-linear deformation behaviors. At about 32 N the structure of sample **B** fails and a buckling effect occurs. Henceforth a weaker and less stiffer response to outer load can be recognized. A local minimum appears in the plot if a pivot or a beam breaks. After one failure within the structure the specimen "recovers" and is able to carry even higher loads than before. Because of the complex geometry, beams and pivots reorganize themselves resulting in a higher resistance to outer load, so that even higher loads can be carried (see sample **B**) after local failure in a beam or a pivot.

This kind of extraordinary deformation behavior was also observed in the torsion-tests (see Fig. 10). A strongly non-linear dependence of moment and angle was measured (blue curve). The maximal torsion-load of sample **B** is about seventeen times higher than the one measured for the polyamide sample **A**. Note that the maximum torque was measured for sample **A** after about one full rotation and for sample **B** at a rotation of about $280°$. These high values indicate a very robust and strong resistance to outer torsion-loads and will be discussed further in future research with a focus on specific material characteristics (Misra, 1997; Misra and Chang, 1993) and geometric non-linearity (Misra et al., 2018).

By comparing the out-of-plane movement of both samples during the shearing-test, which are marked red for positive values and green for negative values on second ordinate axis in Fig. 9, non-symmetric out-of-plane movement for the polyamide sample **A** and symmetric out-of-plane movement for the aluminum sample **B** are distinguishable. The positive out-of-plane movement of sample **A** is much smaller than the negative one. This is visualized in the upper picture and in the middle picture of Fig. 11 by the red areas for positive out-of-plane movements and by the blue areas for negative out-of-plane movements. One reason for this behavior is the manufacturing-process of the specimen. Because of the print direction in rapid-prototyping, a non-homogeneous material distribution resulting in an asymmetry of the structure is conceivable. Another reason could result from the machine compliance of the mounting device (the same one was used for all experiments). Because of the symmetric out-of-plane movement of the aluminum sample **B**, which shows much stiffer and symmetric response behavior (see lower picture of Fig. 11), the machine compliance should not be the main reason for the non-symmetric out-of-plane movement. The symmetric out-of-plane movement of sample **B** starts at about 9 mm simultaneously when the kink of the shear-force occurs. At this very point the whole structure becomes unstable, because some beams start to buckle and to twist resulting in an out-of-plane movement. Another explanation could come from the failure of pivots. After leaving the elastic range, the pivot is plastically deformed and unable to resist the shear-force resulting in a failure and therefore out-of-plane movement of the attached beams.

In Fig. 12 the positive (red areas) and negative (blue areas) out-of-plane movements are visualized for the case of torsion. By comparing the maximal out-of-plane movements of shearing with torsion in Table 2, lower values for torsion are measured. The main reason for this fact is the limitation of the camera-focus. In the very middle of the recorded picture the focus is better than in the outer corners, were the evaluated out-of-plane movement of points was measured. But still, the non-smoothed results indicate that the measured values are within an error of $\pm 10\,\mu$m.

In order to achieve more precise results in the future, a redesign of the mounting clamps has to be considered allowing to manipulate the mounting plates to ensure their parallelism. Furthermore, all parts should be manufactured with a stronger material, such as stainless steel, with the aim to reduce the compliance of the mounting device. Another source of error is the manufacturing process of the specimen. Here we suggest to optimize the process-parameters for printing machines in order to find a procedure, in which a more homogeneous specimen will be printed. Moreover, the calibration procedure between the cameras should be developed further. It is important to find the right balance between illumination settings and contrast of the speckle pattern. Based on the preliminary work of (dell'Isola et al., 2016a; Placidi et al., 2015; Barchiesi et al., 2018) we want to develop an analytical and numerical model to investigate the extraordinary deformation behavior more precisely. A key point to obtain predictive simulations is to identify the material parameters to be used in the adopted models. To address this issue the reader may refer to the recent achievements obtained in (Placidi et al., 2015, 2017b,a).

Another future development concerns the ability to describe possible interactions between beams in the cases in which these come into contact (see, e.g., Misra and Huang (2012); Andreaus et al. (2016, 2013); Misra et al. (2018)). This circumstance is very interesting because PSs, which behave like a second gradient material (dell'Isola et al., 2016c, 2015a; Eugster and dell'Isola, 2017b,a), can exhibit some sort of phase transition behavior characterized by the presence of zones behaving like a first gradient material (De Masi et al. (2006); Chatzigeorgiou et al. (2015); De Masi et al. (2011)). Furthermore, the development of models related to damage evolution and plasticity

should be taken into account for the particular nature of the system under study. To address this issue some first results are presented in (Yang and Misra, 2012; Thiagarajan and Misra, 2004; Placidi, 2016). As seen in (Turco et al., 2016b,a; Barchiesi et al., 2018) and described for other materials in (Ganzosch and Müller, 2016), results obtained from higher gradient simulations will be compared with our real experiments and investigated further. 2D-structures with 3D-deformation were considered in this work. But with the progress in 3D-prototyping, we are also able to investigate 3D-deformation of 3D-structures, which are based on pantographic sheets, in the future.

Pantographic structures show extraordinary features: the deformation behavior is strongly nonlinear, and they are able to undergo large elastic deformations without reaching complete failure (strong resilient behavior). The combination of this special deformation behavior and intelligent artificial materials, such as electroactive polymers, makes PSs very interesting for industrial applications: It is conceivable that PSs could serve as a meta-material for stents or in medical devices (because of their resilient properties) or as a protective bullet-shield for security applications.

5 Acknowledgement

We want to thank Dag Wulsten and Paul Zaslansky from the Julius Wolff Institute at Charité in Berlin, Germany, for their help and support in the lab.

References

Alibert, J.-J.; Seppecher, P.; dell'Isola, F.: Truss modular beams with deformation energy depending on higher displacement gradients. *Mathematics and Mechanics of Solids*, 8, 1, (2003), 51–73.

Alsayednoor, J.; Lennard, F.; Yu, W.; Harrison, P.: Influence of specimen pre-shear and wrinkling on the accuracy of uniaxial bias extension test results. *Composites Part A: Applied Science and Manufacturing*, 101, (2017), 81–97.

Altenbach, H.; Eremeyev, V.: Eigen-vibrations of plates made of functionally graded material. *Computers, Materials, & Continua*, 9, 2, (2009a), 153–178.

Altenbach, H.; Eremeyev, V. A.: On the bending of viscoelastic plates made of polymer foams. *Acta Mechanica*, 204, 3-4, (2009b), 137.

Altenbach, H.; Eremeyev, V. A.: Vibration analysis of non-linear 6-parameter prestressed shells. *Meccanica*, 49, 8, (2014), 1751–1761.

AminPour, H.; Rizzi, N.: A one-dimensional continuum with microstructure for single-wall carbon nanotubes bifurcation analysis. *Mathematics and Mechanics of Solids*, 21, 2, (2016), 168–181.

Andreaus, U.; Baragatti, P.; Placidi, L.: Experimental and numerical investigations of the responses of a cantilever beam possibly contacting a deformable and dissipative obstacle under harmonic excitation. *International Journal of Non-Linear Mechanics*, 80, (2016), 96–106.

Andreaus, U.; Placidi, L.; Rega, G.: Microcantilever dynamics in tapping mode atomic force microscopy via higher eigenmodes analysis. *Journal of Applied Physics*, 113, 22, (2013), 224–302.

Auffray, N.; Dirrenberger, J.; Rosi, G.: A complete description of bi-dimensional anisotropic strain-gradient elasticity. *International Journal of Solids and Structures*, 69, (2015), 195–206.

Barchiesi, E.; Ganzosch, G.; Liebold, C.; Placidi, L.; Grygoruk, R.; Müller, W. H.: Out-of-plane buckling of pantographic fabrics in displacement-controlled shear tests: experimental results and model validation. *Continuum Mechanics and Thermodynamics*.

Battista, A.; Del Vescovo, D.; Rizzi, N.; Turco, E.: Frequency shifts in natural vibrations in pantographic metamaterials under biaxial tests. *Technische Mechanik*, 37, 1, (2017), 17.

Chatzigeorgiou, G.; Javili, A.; Steinmann, P.: Multiscale modelling for composites with energetic interfaces at the micro-or nanoscale. *Mathematics and Mechanics of Solids*, 20, 9, (2015), 1130–1145.

Cuomo, M.; dell'Isola, F.; Greco, L.; Rizzi, N.: First versus second gradient energies for planar sheets with two families of inextensible fibres: Investigation on deformation boundary layers, discontinuities and geometrical instabilities. *Composites Part B: Engineering*, 115, (2017), 423–448.

De Masi, A.; Dirr, N.; Presutti, E.: Interface instability under forced displacements. In: *Annales Henri Poincaré*, vol. 7, pages 471–511, Springer (2006).

De Masi, A.; Merola, I.; Presutti, E.; Vignaud, Y.: Potts models in the continuum. uniqueness and exponential decay in the restricted ensembles. *Journal of Statistical Physics*, 133, 2, (2008), 281–345.

De Masi, A.; Merola, I.; Presutti, E.; Vignaud, Y.: Coexistence of ordered and disordered phases in potts models in the continuum. *Journal of Statistical Physics*, 134, 2, (2009), 243–306.

De Masi, A.; Presutti, E.; Tsagkarogiannis, D.: Fourier law, phase transitions and the stationary stefan problem. *Archive for rational mechanics and analysis*, 201, 2, (2011), 681–725.

Della Corte, A.; dell'Isola, F.; Esposito, R.; Pulvirenti, M.: Equilibria of a clamped euler beam (elastica) with distributed load: Large deformations. *Mathematical Models and Methods in Applied Sciences*, pages 1–31.

dell'Isola, F.; Andreaus, U.; Placidi, L.: At the origins and in the vanguard of peridynamics, non-local and higher-gradient continuum mechanics: An underestimated and still topical contribution of Gabrio Piola. *Mathematics and Mechanics of Solids*, 20, 8, (2015a), 887–928.

dell'Isola, F.; Cuomo, M.; Greco, L.; Della Corte, A.: Bias extension test for pantographic sheets: numerical simulations based on second gradient shear energies. *Journal of Engineering Mathematics*, 103, 1, (2017), 127–157.

dell'Isola, F.; Della Corte, A.; Giorgio, I.; Scerrato, D.: Pantographic 2D sheets: Discussion of some numerical investigations and potential applications. *International Journal of Non-Linear Mechanics, Elsevier*, 80, (2016a), 200–208.

dell'Isola, F.; Della Corte, A.; Greco, L.; Luongo, A.: Plane bias extension test for a continuum with two inextensible families of fibers: A variational treatment with lagrange multipliers and a perturbation solution. *International Journal of Solids and Structures*, 81, (2016b), 1–12.

dell'Isola, F.; Giorgio, I.; Pawlikowski, M.; Rizzi, N.: Large deformations of planar extensible beams and pantographic lattices: heuristic homogenization, experimental and numerical examples of equilibrium. 472, 2185, (2016c), 790.

dell'Isola, F.; Lekszycki, T.; Pawlikowski, M.; Grygoruk, R.; Greco, L.: Designing a light fabric metamaterial being highly macroscopically tough under directional extension: First experimental evidence. *Zeitschrift für angewandte Mathematik und Physik, ZAMP*, 66, 6, (2015b), 3473–3498.

dell'Isola, F.; Seppecher, P.; Della Corte, A.: The postulations á la d'alembert and á la cauchy for higher gradient continuum theories are equivalent: a review of existing results. 471, 2183, (2015c), 415.

dell'Isola, F.; Steigmann, D.: A two-dimensional gradient-elasticity theory for woven fabrics. *Journal of Elasticity*, 118, 1, (2015), 113–125.

dell'Isola, F.; Steigmann, D.; Della Corte, A.: Synthesis of fibrous complex structures: designing microstructure to deliver targeted macroscale response. *Applied Mechanics Reviews*, 67, 6, (2016d), 21.

Dos Reis, F.; Ganghoffer, J.: Construction of micropolar continua from the asymptotic homogenization of beam lattices. *Computers & Structures*, 112, (2012), 354–363.

Eremeyev, V. A.; Pietraszkiewicz, W.: Material symmetry group and constitutive equations of micropolar anisotropic elastic solids. *Mathematics and Mechanics of Solids*, 21, 2, (2016), 210–221.

Eugster, S. R.; dell'Isola, F.: Exegesis of sect. ii and iii. a from "fundamentals of the mechanics of continua". *Zeitschrift für Angewandte Mathematik und Mechanik*.

Eugster, S. R.; dell'Isola, F.: Exegesis of the introduction and sect. i from "fundamentals of the mechanics of continua". *Zeitschrift für Angewandte Mathematik und Mechanik*, 97, 4, (2017b), 477–506.

Ganzosch, G.; dell'Isola, F.; Turco, E.; Lekszycki, T.; Müller, W.: Shearing tests applied to pantographic structures. *Acta Polytechnica CTU Proceedings*, 7, 1–6.

Ganzosch, G.; Müller, W. H.: Experimental techniques applied to generalized continuum theories - a state-of-the-art report. *Proceedings of the XLIV Summer School-Conference Advanced Problems in Mechanics, APM, St. Petersburg, Russia*, 44, (2016), 149–161.

Giorgio, I.; Della Corte, A.; dell'Isola, F.; Steigmann, D. J.: Buckling modes in pantographic lattices. *Comptes Rendus Mecanique*, 344, 7, (2016), 487–501.

Harrison, P.: Modelling the forming mechanics of engineering fabrics using a mutually constrained pantographic beam and membrane mesh. *Composites Part A: Applied Science and Manufacturing*, 81, (2016), 145–157.

Hendy, C. R.; Turco, E.: Numerical validation of simplified theories for design rules of transversely stiffened plate girders. *Structural Engineer*, 86, 21, (2008), 37–46.

Launay, J.; Hivet, G.; Duong, A. V.; Boisse, P.: Experimental analysis of the influence of tensions on in plane shear behaviour of woven composite reinforcements. *Composites science and technology*, 68, 2, (2008), 506–515.

Lejeune, E.; Javili, A.; Linder, C.: An algorithmic approach to multi-layer wrinkling. *Extreme Mechanics Letters*, 7, (2016), 10–17.

Misra, A.: Mechanist Model for Contact Between Rough Surfaces. *Journal of Engineering Mechanics*, 123, 5, (1997), 475–484.

Misra, A.; Chang, C. S.: Effective elastic moduli of heterogeneous granular solids. *International Journal of Solids and Structures*, 30, 18, (1993), 2547–2566.

Misra, A.; Huang, S.: Micromechanical stress–displacement model for rough interfaces: Effect of asperity contact orientation on closure and shear behavior. *International Journal of Solids and Structures*, 49, 1, (2012), 111–120.

Misra, A.; Lekszycki, T.; Giorgio, I.; Ganzosch, G.; Müller, W. H.; dell'Isola, F.: Pantographic metamaterials show atypical poynting effect reversal. *Mechanics Research Communications*, 89, (2018), 6 – 10.

Misra, A.; Parthasarathy, R.; Singh, V.; Spencer, P.: Micro-poromechanics model of fluid-saturated chemically active fibrous media. *ZAMM-Journal of Applied Mathematics and Mechanics/Zeitschrift für Angewandte Mathematik und Mechanik*, 95, 2, (2015), 215–234.

Mower, T.; Long, M.: Mechanical behavior of additive manufactured, powder-bed laser-fused materials. *Material Science and Engineering A*, 651, (2016), 198–213.

Pideri, C.; Seppecher, P.: A second gradient material resulting from the homogenization of an heterogeneous linear elastic medium. *Continuum Mechanics and Thermodynamics*, 9, 5, (1997), 241–257.

Placidi, L.: A variational approach for a nonlinear one-dimensional damage-elasto-plastic second-gradient continuum model. *Continuum Mechanics and Thermodynamics*, 28, 1-2, (2016), 119–137.

Placidi, L.; Andreaus, U.; Della Corte, A.; Lekszycki, T.: Gedanken experiments for the determination of two-dimensional linear second gradient elasticity coefficients. *Zeitschrift für angewandte Mathematik und Physik, ZAMP*, 66, 6, (2015), 3699–3725.

Placidi, L.; Barchiesi, E.; Battista, A.: An inverse method to get further analytical solutions for a class of metamaterials aimed to validate numerical integrations. In: *Mathematical Modelling in Solid Mechanics*, pages 193–210, Springer (2017a).

Placidi, L.; Barchiesi, E.; Della Corte, A.: Identification of two-dimensional pantographic structures with a linear d4 orthotropic second gradient elastic model accounting for external bulk double forces. In: *Mathematical Modelling in Solid Mechanics*, pages 211–232, Springer (2017b).

Placidi, L.; Barchiesi, E.; Turco, E.; Rizzi, N. L.: A review on 2D models for the description of pantographic fabrics. *Zeitschrift für angewandte Mathematik und Physik*, 67, 5, (2016), 121.

Selvadurai, A.; Nikopour, H.: Transverse elasticity of a unidirectionally reinforced composite with an irregular fibre arrangement: experiments, theory and computations. *Composite Structures*, 94, 6, (2012), 1973–1981.

Spagnuolo, M.; Barcz, K.; Pfaff, A.; dell'Isola, F.; Franciosi, P.: Qualitative pivot damage analysis in aluminum printed pantographic sheets: numerics and experiments. *Mechanics Research Communications*, pages 47–52.

Steigmann, D. J.; dell'Isola, F.: Mechanical response of fabric sheets to three-dimensional bending, twisting, and stretching. *Acta Mechanica Sinica*, 31, 3, (2015), 373–382.

Thiagarajan, G.; Misra, A.: Fracture simulation for anisotropic materials using a virtual internal bond model. *International Journal of Solids and Structures*, 41, 11, (2004), 2919–2938.

Turco, E.: Load distribution modelling for pin-jointed trusses by an inverse approach. *Computer Methods in Applied Mechanics and Engineering*, 165, 1-4, (1998), 291–306.

Turco, E.; dell'Isola, F.; Cazzani, A.; Rizzi, N.: Hencky-type discrete model for pantographic structures: numerical comparison with second gradient continuum models. *Zeitschrift für angewandte Mathematik und Physik, ZAMP*, 67, 85, (2016a), 1–28.

Turco, E.; dell'Isola, F.; Rizzi, N.; Grygoruk, R.; Müller, W.; Liebold, C.: Fiber rupture in sheared planar pantographic sheets: Numerical and experimental evidence. *Mechanics Research Communications, Elsevier*, 76, (2016b), 86–90.

Turco, E.; Giorgio, I.; Misra, A.; dell'Isola, F.: King post truss as a motif for internal structure of (meta)material with controlled elastic properties. *Royal Society Open Science*, 4, (2017), 20.

Turco, E.; Golaszewski, M.; Cazzani, A.; Rizzi, N. L.: Large deformations induced in planar pantographic sheets by loads applied on fibers: experimental validation of a discrete lagrangian model. *Mechanics Research Communications*, 76, (2016c), 51–56.

Yang, Y.; Misra, A.: Micromechanics based second gradient continuum theory for shear band modeling in cohesive granular materials following damage elasticity. *International Journal of Solids and Structures*, 49, 18, (2012), 2500–2514.

Zeidi, M.; Kim, C. I.: Mechanics of fiber composites with fibers resistant to extension and flexure. *Mathematics and Mechanics of Solids*.

Address: Gregor Ganzosch, Technische Universität Berlin,
Institut für Mechanik, Fachgebiet Kontinuumsmechanik und Materialtheorie,
Sekr. MS2, Einsteinufer 5, 10587 Berlin, Germany
email: `ganzosch@tu-berlin.de`

Address: Klaus Hoschke, Fraunhofer-Institut für Kurzzeitdynamik Freiburg,
Ernst-Mach-Institut, Freiburg, Germany

Address: Tomasz Lekszycki, Warsaw University of Technology
and Department of Experimental Physiology and Pathophysiology, Medical University of Warsaw, Warsaw, Poland

---

Address: Ivan Giorgio, Sapienza University of Rome, Italy
and International Research Center for the Mathematics and Mechanics of Complex Systems, L'Aquila, Italy

---

Address: Emilio Turco, Universita Di Sassari
Dipartimento Di Architettura, Design e Urbanistica, Sassari, Italy

---

Address: Wolfgang H. Müller, Technische Universität Berlin,
Institut für Mechanik, Fachgebiet Kontinuumsmechanik und Materialtheorie, Berlin, Germany

4.3 Out-of-plane buckling of pantographic fabrics in displacement-controlled shear tests: experimental results and model validation

[3]: Emilio Barchiesi, Gregor Ganzosch, Christian Liebold, Luca Placidi, Roman Grygoruk, and Wolfgang H. Müller. Out-of-plane buckling of pantographic fabrics in displacement-controlled shear tests: experimental results and model validation. *Continuum Mechanics and Thermodynamics,* 31(1):33–45, 2019.

Abstract: Due to the latest advancements in 3D printing technology and rapid prototyping techniques, the production of materials with complex geometries has become more affordable than ever. Pantographic structures, because of their attractive features, both in dynamics and statics and both in elastic and inelastic deformation regimes, deserve to be thoroughly investigated with experimental and theoretical tools. Herein, experimental results relative to displacement-controlled large deformation shear loading tests of pantographic structures are reported. In particular, five differently sized samples are analyzed up to first rupture. Results show that the deformation behavior is strongly nonlinear, and the structures are capable of undergoing large elastic deformations without reaching complete failure. Finally, a cutting edge model is validated by means of these experimental results.

DOI: https://doi.org/10.1007/s00161-018-0626-x

Continuum Mech. Thermodyn. (2019) 31:33–45
https://doi.org/10.1007/s00161-018-0626-x

ORIGINAL ARTICLE

Emilio Barchiesi · Gregor Ganzosch · Christian Liebold · Luca Placidi · Roman Grygoruk · Wolfgang H. Müller

Out-of-plane buckling of pantographic fabrics in displacement-controlled shear tests: experimental results and model validation

Received: 17 November 2017 / Accepted: 15 January 2018 / Published online: 27 January 2018

Abstract Due to the latest advancements in 3D printing technology and rapid prototyping techniques, the production of materials with complex geometries has become more affordable than ever. Pantographic structures, because of their attractive features, both in dynamics and statics and both in elastic and inelastic deformation regimes, deserve to be thoroughly investigated with experimental and theoretical tools. Herein, experimental results relative to displacement-controlled large deformation shear loading tests of pantographic structures are reported. In particular, five differently sized samples are analyzed up to first rupture. Results show that the deformation behavior is strongly nonlinear, and the structures are capable of undergoing large elastic deformations without reaching complete failure. Finally, a cutting edge model is validated by means of these experimental results.

Keywords Out-of-plane buckling · Pantographic structures · Higher gradient continua · Experimental analysis

1 Introduction

Following the recent trend in material manufacturing technology, many theoretical investigations have been directed toward the development of mathematical models capable of describing mechanical systems characterized by complex geometries. Indeed, with the latest advancements in, e.g., 3D printing technology and, more in general, of rapid prototyping techniques, the small-scale production of materials with complex geometries has become more affordable than ever (see e.g., [7,26,43,60]). By exploiting these new technologies, materials with very different structures have been developed in the last few years with the aim of synthesizing materials that, at a well-specified macroscopic scale, exhibit a behavior which can be described by nonstandard mathematical models like the generalized continuum theories that were rediscovered in the last 50 years. Without claiming any priority, as it might be the case that the same scientific ideas were previously formulated and

Communicated by Francesco dell'Isola.

E. Barchiesi ( )
Università degli studi di Roma "La Sapienza", 18, Via Eudossiana, 00184 Rome, Italy
E-mail: barchiesiemilio@gmail.com

G. Ganzosch · C. Liebold · W. H. Müller
Faculty of Mechanics, Berlin University of Technology, Einsteinufer 5, 10587 Berlin, Germany

L. Placidi
International Telematic University Uninettuno, 39, C.so Vittorio Emanuele II, 00186 Rome, Italy

R. Grygoruk
Institute of Mechanics and Printing, Warsaw University of Technology, 85 Narbutta, Warsaw 02-524, Poland

then lost (see [51,56]), we can surely state that these theories were already known at least two centuries ago (see [18,19]). Pantographic structures have been proposed recently as a meta-material (see [17]) which is well described by second-gradient continuum theories [1,24,47]. They represent an effort to support the idea that a change in the vision of modern mechanics is needed, as it will be made more clear in the sequel. Typically, pantographic sheets are structures made up of two orthogonal families (this is not always the case, see [59]) of extensible straight (this is not always the case as well, see [36,53]) fibers lying on different parallel planes. Two fibers belonging to different planes are connected by small elastic cylinders, customarily called pivots, orthogonal to the two planes. Such structures have proved to show very interesting features, both in dynamics and statics and both in elastic and inelastic deformation regimes. With regard to their dynamics, by means of a network of Euler beams, the use of long and thin strips of pantographic sheets as wave guides has been investigated with promising applications. The propagation of quasi-solitons in such strips has been observed by means of a homogenized 1D continuum second-gradient model [35]. This feature could open the way to the use of pantographic strips in non-dissipative mechanical signaling transmission systems, which are of great utility in all those applications where the use of electric and/or electronic actuation has to be avoided as much as possible [20,22,30]. For instance, such devices could be employed for the actuation of safety valves in chemical plants, where a high risk of fires and explosions is frequently faced due to the inflammability of industrial chemical commodities. As a last example of the interesting features exhibited by pantographic fabrics in dynamic regime, we mention that their capability of storing elastic energy by means of different mechanisms related to their special microstructure, such as the different combinations of bending and stretching of fibers and of shearing and torsion of pivots, has been exploited to show that natural frequencies in pantographic sheets are not monotonically increasing with an increasing pre-stretch. This last point has been the subject of [5,6], where a homogenized elastic 2D continuum model has been exploited. Some continuum models, all based on variational approaches (see e.g., [25]) and sometimes having different Lagrangian coordinates, have been developed for the description of the statics of pantographic fabrics, each one of them being based on different hypotheses (inextensibility of fibers [21,39], pivots behaving like perfect hinges, etc.). Nevertheless, they all contain an essential ingredient: the relevant phenomenon of bending of fibers gives rise to second-gradient theories (for a motivation of this statement see [8,29,48,49]). For a comprehensive account of the existing literature on models for the 2D and 3D statics and dynamics of pantographic fabrics, see [4,50].

The inelastic regime of such structures is very interesting as well. Indeed, as it is clear by looking at a force–displacement diagram in tests like, e.g., displacement-controlled shear and bias extension, pantographic sheets are very robust structures. This is to mean that, following the first fiber and/or pivot rupture, pantographic fabrics do not undergo a structural failure, but loads are redistributed in such a way that the force required for the next element rupture usually increases instead of decreasing. Moreover, even if at an initial state of its development, the study of damage in these structures allows to forecast easily the position where the first and subsequent ruptures occur. It is also clear that the material the structure is made of (ductile or fragile) greatly influences rupture mechanisms and, subsequently, the position where such ruptures occur. So far, the study of damage mechanisms in pantographic fabrics has been addressed from a modeling standpoint in two papers [54,58] (see for more details on the topic of damage and dissipation in complex materials [3,13,14,38,44–46]). Further experimental data can be found also in [24,34]. We want to explicitly remark here that both continuum and discrete Hencky-type [2,12,23,27,40–42,55,57] elastic models have been employed in the literature, with suitable adaptions, for the study of structural degradation phenomena in pantographic fabrics. At the beginning of this Introduction, we mentioned that pantographic fabrics are not just a technological attempt of synthesizing an application-driven meta-material. Rather, they provide a chance to prove that theoretical developments, which may be initially considered difficult to frame in a real context, are at the basis of technological advancement, which is thus a consequence of them and not only at their origin, as it has been longly argued by some influential scientists: Generalized continuum theories were developed at least two centuries ago and then rediscovered in the 1960s ([28,32,33]). For a long time, the main argument raised by the opponents of such theories was that no existing structure could be described by such generalized theories much better than by classical continuum models, hence claiming their uselessness. Notwithstanding the fact that there exist some complex natural materials whose satisfactory mechanical description is possible only with generalized models, and this must have been known also by these opponents, the advent of new powerful manufacturing techniques has opened the way to the production of microstructured artificial materials, which are purposely designed to obey such generalized theories: Pantographic fabrics are in this sense an example to show that it is dangerous to underestimate new theories on the basis of their immediate applications.

In order to validate and direct new theoretical developments, the contribution of experimental measurements must not be underestimated as well. Only a continuous comparison with experimental results can help in

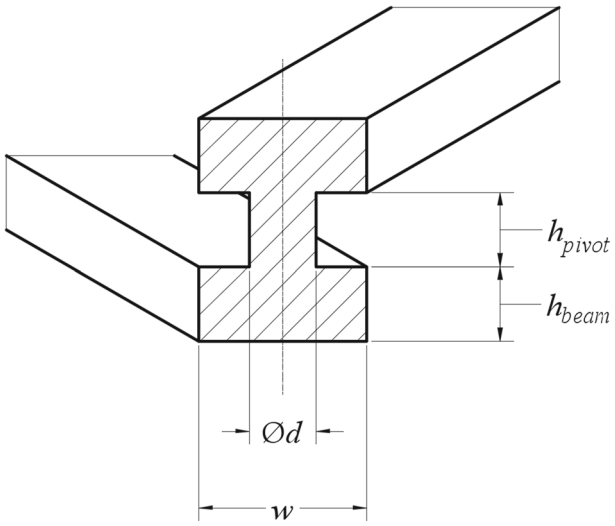

Fig. 1 Cross section scheme of a connecting pivot in a pantographic structure

Table 1 Overview of the geometric parameters characterizing the five different specimens analyzed

Sample	w (mm)	h_{beam} (mm)	d (mm)	h_{pivot} (mm)
A	1.00	1.00	0.90	1.00
B	1.60	1.00	0.90	1.00
C	1.60	1.60	0.90	1.00
D	2.25	1.60	0.90	1.00
E	2.25	1.60	0.90	3.00

ensuring that such theoretical developments are step by step approximating ever more the physical system under study. It is for this reason that we believe this paper to be an example of how experimental and theoretical investigations should interact one with each other in order to foster synergies (instead of rivalries) between different approaches to the same problem. In this paper, experimental results relative to displacement-controlled large deformation shear loading tests of pantographic structures are reported. In particular, five differently sized samples are analyzed up to first rupture. Their response to the deformation is recorded by a force transducer and an optical 3D measurement system. Subsequently, digital image correlation (DIC) is used to compute the deformation out of the shearing plane by the help of a two-camera system. Results show that the deformation behavior is strongly nonlinear, and the structures are capable to undergo large elastic deformations without reaching complete failure.

The plan of the work is the following. In Sect. 2, the experimental setup is thoroughly described and experimental results are being reported. In Sect. 3, the main features of a recently proposed model suitable to describe the out-of-plane buckling are outlined and such a model is then employed to describe the experimental results reported in Sect. 2. Finally, in Sect. 4 we present some conclusions and an outlook.

2 Experimental setup and results

Pantographic samples tested during our investigations have been produced with the aid of a 3D printer, using polyamide powder as raw material. First, 3D geometries have been generated by means of the commercial CAD software `SolidWorks`® (Dassault Systèmes SolidWorks Corporation, Waltham, MA 02451). A STL–format file has been used as input file for the 3D printer `Formiga P 100`® (EOS GmbH, Munich, Germany). Five specimens with different internal geometries, but equal volume mass density, were produced. A schematic outline of the samples, as they have been described in the introduction, is presented in Fig. 1, where the different beam and pivot parameters are explained. The values for such parameters are summarized for the five samples in Table 1. Our study mainly focuses on the influence of different beam parameters on the deformation behavior during the displacement-controlled shear test. The macroscopic dimensions of the pantographic sheets are 210 mm $\times$ 70 mm.

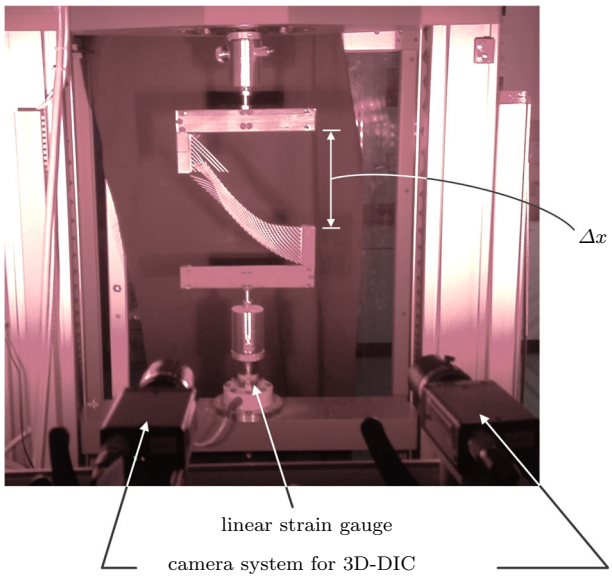

Fig. 2 Experimental setup for shear test: camera devices and the shear adaption device mounted in the tensile testing machine

In Fig. 2, an overview of the experimental setup is shown. A `Zwick Z010`® testing device, controlled by the software `TestExpert`®, has been used for the shear tests.
The resulting reaction force was measured by a load cell (`Zwick-Xforce`®) attached to the device. The force transducer is able to record axial forces in the range of about $\pm\, 10,000\,\mathrm{N}$, whereas the accuracy at 20 N is 0.2%. The displacement Δx was controlled vertically. The upper part of the tensile-to-shear adaption device (Fig. 2) is fixed, while the lower part can be linearly moved in the vertical direction. The displacement rate for the tests has been set to 15 mm/min, which can be considered quite slow for such tests. The displacement itself was recorded and monitored by a device own encoder unit with an accuracy of $\pm\, 2.0\,\mu\mathrm{m}$.

In addition, in order to measure the state of three-dimensional deformation of the equivalent surface representing the 3D sheets, the noninvasive optical measurement device `Q-400` (Dantec Dynamics GmbH, Ulm, Germany) has been installed together with four cameras, see Fig. 2. Two cameras have been employed to record the experiment, while another two-camera system was able to recognize the 3D motion within the overlapping region of the image sections of both cameras. We remark that the displacement out of the shear plane is subject to a higher error due to the fact that, in the worst case, if out-of-plane motion is out of the focus areas of the cameras, the software smears both planes of beams into one plane, or a facet disappears. Due to the large deformation undergone in these experiments by the specimens, the overlapping region of the image sections was doubled, in order to capture the whole deformation process. In order to enable the separation of small surface areas (so-called facets) by means of image correlation software, the whole surface of all specimens has been sprayed in a speckled pattern using an airbrush system and the acrylic-based waterproof ink (Molotow One4All, Feuerstein GmbH, Lahr, Germany). During the deformation process, pictures have been taken every 2 seconds by means of the aforementioned commercial digital image correlation (DIC) camera system with a resolution of about $1,600 \times 1,200$ pixels. Figure 3 shows three exemplary 2D pictures taken by one of the cameras during the shear test up to rupture. Following a calibration procedure of the camera setup, the commercial software `Istra4D`® is able to reconstruct a three-dimensional surface deformation.
Originally, the adaption device had been equipped with linear guides, to ensure a parallel movement of the upper and lower sides of the specimens. Nevertheless, the present measurements have been performed without the linear guides, in order to reduce the friction-induced noise signals. Results from the DIC measurements indicate that the vertical parallelism condition is still fulfilled, even for high loads. After evaluating the 3D data, only a minor out-of-plane movement of the lower part of the shear adapter has been recognized and taken into account for sample **C**.

In order to analyze quantities related to the out-of-plane displacement of a sheet, a single facet has been selected for each sample, in the place where the maximum out-of-plane movement has been presumed. Due to the large deformations, some facets have moved out of the optical focus, which may cause the image correlation to abort. Furthermore, the image correlation aborts when a sudden rupture occurs in-between the

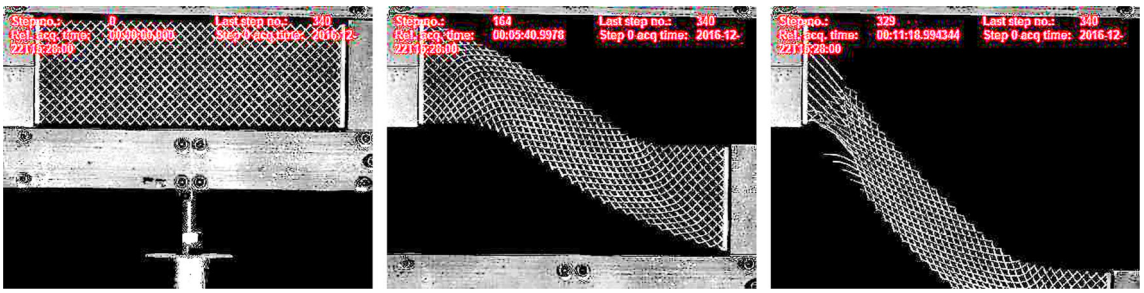

Fig. 3 Raw pictures of the sample **A** up to rupture

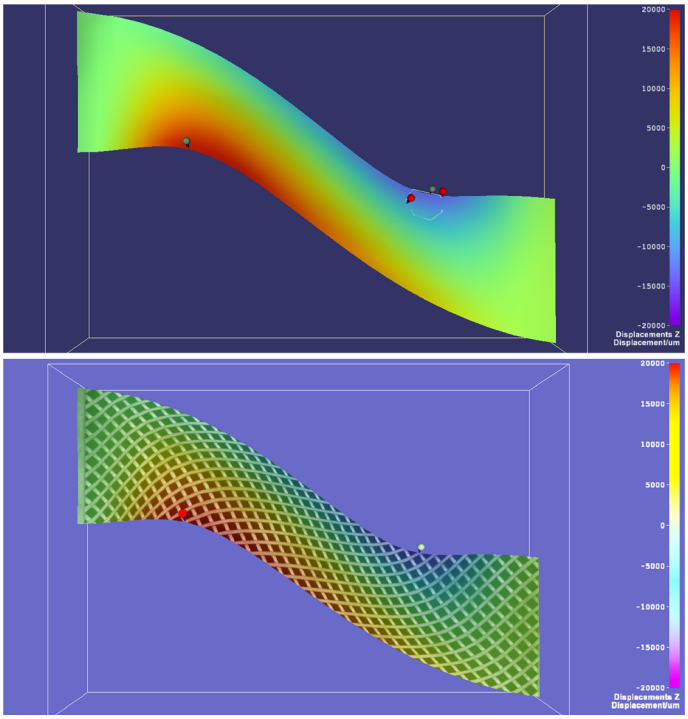

Fig. 4 3D image processing for sample **B**: red areas show out-of-plane positive displacements, blue areas show negative displacements. Acquired data (on the top). Superposition of the out-of-plane displacement field and a picture of the current equilibrium shape (on the bottom) (color figure online)

Table 2 Maximal out-of-plane displacements

Shear sample	**A**	**B**	**C**	**D**	**E**
Out-of-plane displacement (mm)	11.99	21.00	0.93	14.55	3.88

shutter releases, so that the facets to be correlated are laterally displaced too much. For these reasons, some of the plots in Fig. 11 are not complete. The summary of the experimental results for all five samples is displayed in Figs. 10 and 11, showing the plots for the shear force versus prescribed shear displacement, as well as the out-of-plane displacement versus the prescribed shear displacement. The local minima in the plots show a failure of a beam or a pivot. All samples show different and pronounced nonlinear curves. Shear force versus prescribed shear displacement and out-of-plane displacement versus prescribed shear displacement are plotted together in Figs. 5, 6, 7, 8 and 9 for each sample. To illustrate the data acquisition, Fig. 4 shows the processed 3D data of sample **B** during the shear deformation.

Table 2 shows the maximal out-of-plane displacement values for each sample, within the valid measurement ranges.

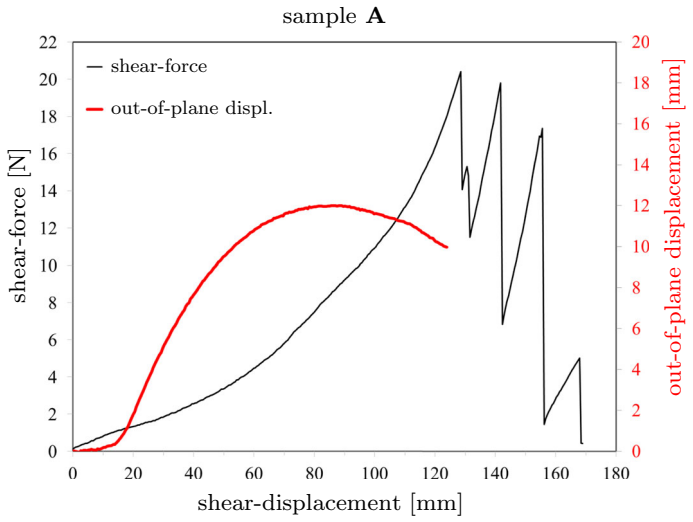

Fig. 5 Shear force and out-of-plane data versus the prescribed shear displacement Δx for sample **A**

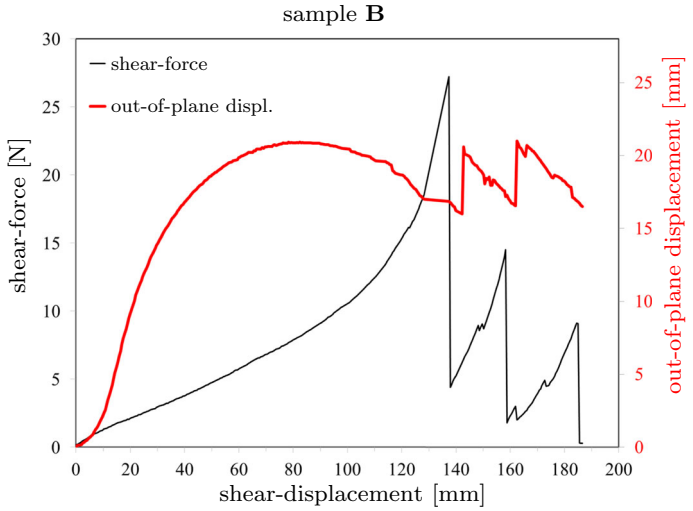

Fig. 6 Shear force and out-of-plane data versus the prescribed shear displacement Δx for sample **B**

As a preliminary analysis to that which will be made in the next section by means of mathematical modeling, we want to provide an insight into the complex interplay of different phenomena involved in the buckling, which is observed in all of the experiments. Buckling out of the shear plane is probably due to the competition of two different local deformation mechanisms: On one side, there is geodesic bending deformation of fibers, i.e., the bending deformation along the plane tangent to the equivalent deformed surface representing the deformed 3D specimen. On the other side, we face bending deformation of the fibers out of the plane tangent to the equivalent deformed surface and, subsequently, their twisting. Depending on whether the stiffness to in-plane bending of the beams is relatively larger than that to out-of-plane bending or not, the former or the latter behavior is observed. The subsequent model can take into account the aforementioned mechanisms and hence, given that it is able to fit well the experimental data, it can prove or disprove the previous interpretation which is solely based on a physical intuition ground. Finally, we want to remark that, clearly, the stiffness of the beams is determined by their dimensions and, therefore, the extent to which buckling is observed is strongly related to the kind of specimen which is considered (for a summary of the dimensions of the beams constituting the analyzed specimen, see Table 1).

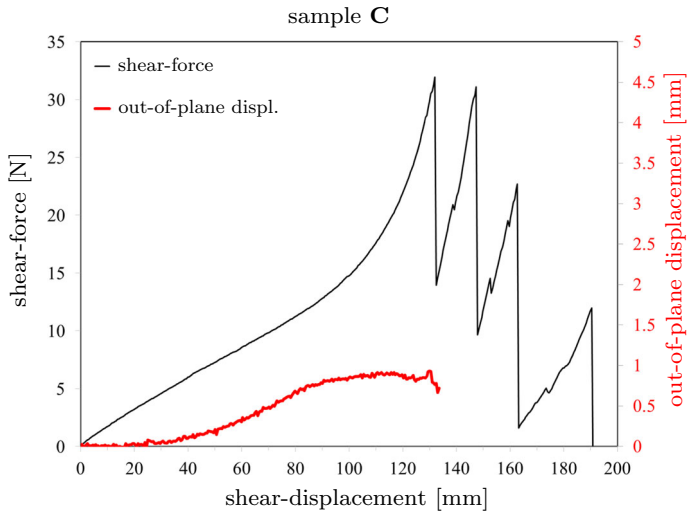

Fig. 7 Shear force and out-of-plane data versus the prescribed shear displacement Δx for sample **C**

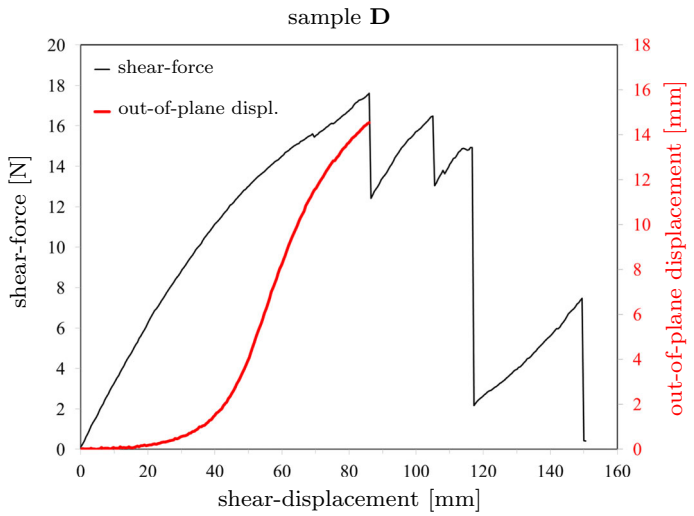

Fig. 8 Shear force and out-of-plane data versus the prescribed shear displacement Δx for sample **D**

3 Model validation

In order to investigate quantitatively the phenomena involved in the previous experiments, we made use of a recently proposed 2D continuum model embedded in a 3D space [37]. Let us consider a two-dimensional continuum, whose body points can be considered in a bijective correspondence with a closed subset $\mathcal{B}$ of the Euclidean space $\mathbb{R}^2$. The set $\mathcal{B}$ represents the shape of the body in the reference (undeformed) configuration. Introducing a Cartesian reference frame $\left(\mathcal{O}, \left(\hat{e}_1, \hat{e}_2\right)\right)$, we denote with $X = (X_1, X_2)$ the coordinates of a generic point in the Euclidean space $\mathbb{R}^2$. Working in a material Lagrangian framework, we define a placement function $\chi : \mathcal{B} \to \mathbb{R}^3$, such that the image $x = \chi(X)$ of X through χ is the position in the current configuration of the point which, in the reference configuration, was at the position X. The displacement field $u : \mathcal{B} \to \mathbb{R}^3$ is defined as $u(X) = \chi(X) - X$. The placement, or equivalently the displacement, is the independent kinematic descriptor of the system. The image $\mathcal{S} = \chi(\mathcal{B})$ of $\mathcal{B}$ through χ is the current shape of the body.

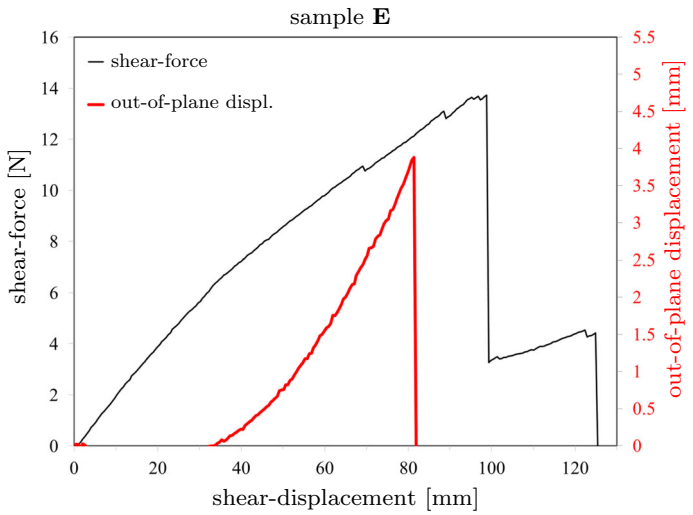

Fig. 9 Shear force and out-of-plane data versus the prescribed shear displacement Δx for sample **E**

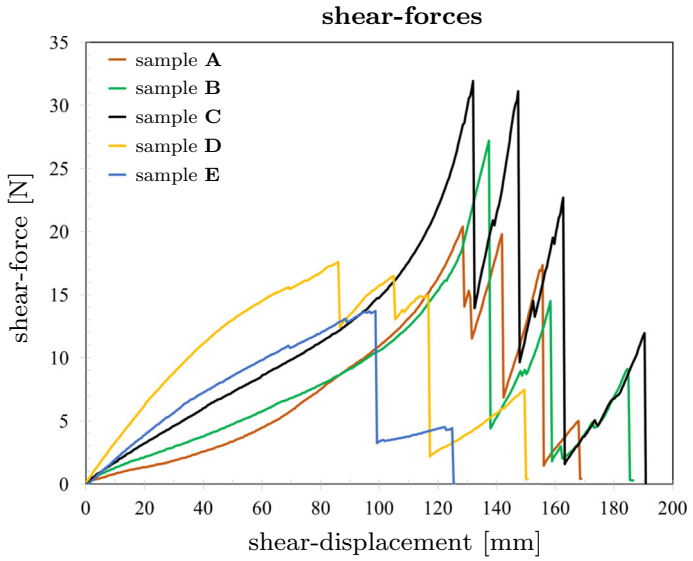

Fig. 10 Shear force data versus the prescribed shear displacement Δx of all samples

Relying on a variational framework, the following deformation energy density is proposed:

$$\pi = \frac{1}{2}\left\{ \mathrm{K}_e\left[\left(\varepsilon^1\right)^2+\left(\varepsilon^2\right)^2\right]+\mathrm{K}_s\left(\left[1+\left(\frac{\gamma}{Q}\right)^2\right]^m-1\right)+ \right.$$
$$\left. +\mathrm{K}_t\left[\left(\kappa_1^1\right)^2+\left(\kappa_1^2\right)^2\right]+\mathrm{K}_n\left[\left(\kappa_2^1\right)^2+\left(\kappa_2^2\right)^2\right]+\mathrm{K}_g\left[\left(\kappa_3^1\right)^2+\left(\kappa_3^2\right)^2\right]\right\}, \tag{1}$$

which is the orthotropic deformation energy density corresponding to a system of two orthogonal continuous families '1' and '2' of straight shear undeformable beams arranged along the coordinate axes in the reference configuration and resembling the pantographic microstructure. Fibers of family 'α' are parallel to the direction $\hat{e}_\alpha$. We shall now address the meaning of each additive contribution:

1. $\frac{1}{2}\mathrm{K}_e\left(\varepsilon^1\right)^2$ and $\frac{1}{2}\mathrm{K}_e\left(\varepsilon^2\right)^2$ are the elongation quadratic additive contributions relative to, respectively, the families '1' and '2' of fibers. The strain measure ε^α, with $\alpha = 1, 2$, is defined as

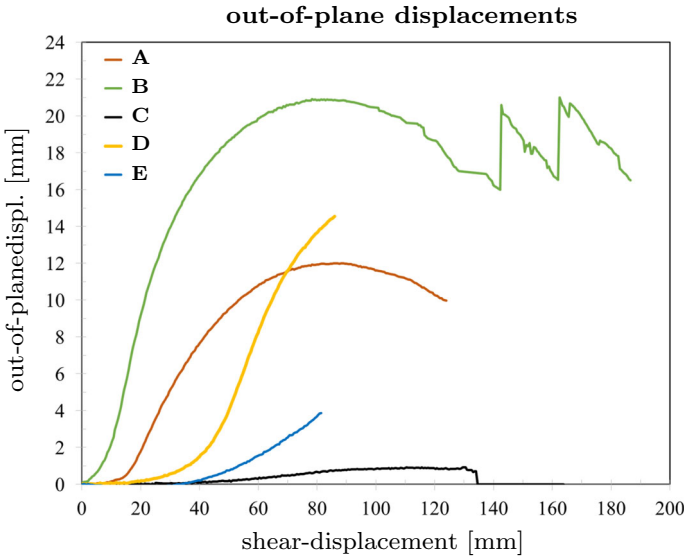

Fig. 11 Out-of-plane data versus the prescribed shear displacement Δx of all samples

$$\varepsilon^{\alpha} = \left\| \frac{\partial \chi}{\partial X_{\alpha}} \right\| - 1$$

and $\mathrm{K}_e \in [0, \infty)$ is the corresponding stiffness, which is the same for the two families of fibers;

2. $\mathrm{K}_s \left(\left[1 + \left(\frac{\gamma}{Q} \right)^2 \right]^m - 1 \right)$ is the Ogden-like additive contribution due to the relative rotation of two orthogonal intersecting fibers (shear). The strain measure $\gamma \in [-\frac{\pi}{2}, \frac{\pi}{2}]$, also referred to as the shear angle, is defined as

$$\gamma = \arcsin \frac{\frac{\partial \chi}{\partial X_1} \cdot \frac{\partial \chi}{\partial X_2}}{\left\| \frac{\partial \chi}{\partial X_1} \right\| \left\| \frac{\partial \chi}{\partial X_2} \right\|},$$

and K_s, m and Q are positive constitutive parameters. We remark that this contribution accounts for deformation energy stored in the pivot because of its torsion of an angle γ and that this contribution has been suitably modified from that proposed in [37];

3. $\frac{1}{2}\left[\mathrm{K}_t \left(\kappa_1^1 \right)^2 + \mathrm{K}_n \left(\kappa_2^1 \right)^2 + \mathrm{K}_g \left(\kappa_3^1 \right)^2 \right]$ and $\frac{1}{2}\left[\mathrm{K}_t \left(\kappa_1^2 \right)^2 + \mathrm{K}_n \left(\kappa_2^2 \right)^2 + \mathrm{K}_g \left(\kappa_3^2 \right)^2 \right]$ are the additive contributions due to twisting, normal bending and geodesic bending of beams belonging, respectively, to families '1' and '2' of fibers. The strain measures κ_1^{α}, κ_2^{α}, κ_3^{α} are the coordinates, in the augmented levorotatory reference Cartesian frame, of the axial vector corresponding to the skew tensor $W^{\alpha} = (R^{\alpha})^{\mathrm{T}} \frac{\partial R^{\alpha}}{\partial X_{\alpha}}$, which is the so-called current curvature tensor. The orthogonal tensor R^{α} transforms the augmented levorotatory reference Cartesian frame vectors into the following ordered triple: (i) the unitary vector tangent to the deformed coordinate line 'α'; (ii) the unitary vector normal to the previous one and lying on to the plane tangent to the deformed surface; (iii) the unitary vector normal to the plane tangent to the deformed surface. Explicit lengthy formulas can be found in [37]. We remark that:
   (a) because of the shear undeformability constraint for the two family of beams;
   (b) since both R^1 and R^2 transform the third vector $\hat{e}_3$ of the augmented levorotatory reference Cartesian frame into the same vector;
   (c) assuming that principal inertia axes of the cross sections for the two families '1' and '2' of beams in the undeformed configuration are considered to be respectively $(\hat{e}_2, \hat{e}_3)$ and $(-\hat{e}_1, \hat{e}_3)$;

   the cross-sections of the two families of fibers being attributed the same second principal inertia axis in the current configuration means that pivots are assumed to remain point-wise orthogonal to the two families of fibers. Thus, such vector can be interpreted as the current axis of the elastic cylindrical pivots and, accordingly, only torsional deformation of pivots is here considered. Finally, we mention that κ_1^{α}, κ_2^{α}, κ_3^{α}

Table 3 Material parameters identified

K_e (N/m)	K_s (N/m)	Q	m	K_t (N m)	K_n (N m)	K_g (N m)
96975	13.589	0.266	0.6751	0.00786	0.0266	0.00898

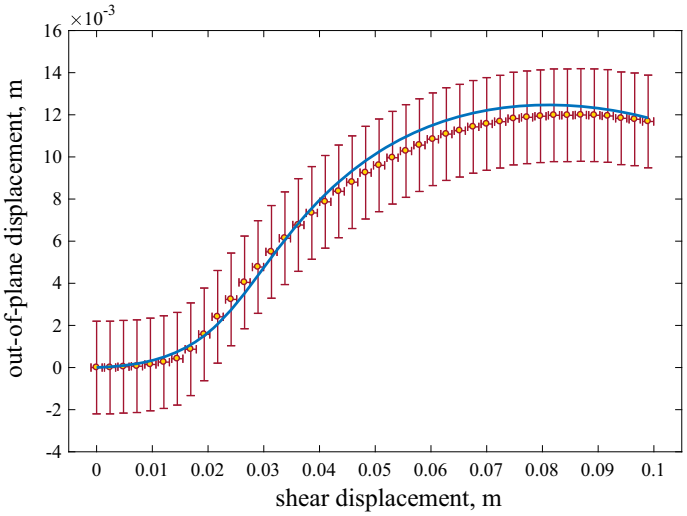

Fig. 12 Maximum out-of-plane displacement versus prescribed shear displacement: comparison between measurements and numerical simulations. Numerical solution (solid line); experimental measures (dotted line). Errors (vertical and horizontal red bars) (color figure online)

can be interpreted also as the geodesic torsion, the normal curvature and the geodesic curvature of the deformed surface multiplied, respectively, by $\|\frac{\partial \chi}{\partial X_\alpha}\|$, as X_α is not a unitary speed parametrization.

We remark that the contributions in point (iii) above entail the dependence of the strain energy density upon second gradient of the displacement field. We explicitly observe that, as the material lines of the deforming surface can undergo in-plane and out-of-plane bending and twisting, the model employed herein can be considered a richer second-gradient continuum with respect to, e.g., classical Kirchhoff–Love plate theory, where only second-gradient contribution related to out-of-plane bending is considered.

On the basis of this model, we performed an identification of the material parameters, namely K_e, K_s, Q, m, K_t, K_n and K_g (Table 3). Experimental measures relative to specimen **A** have been considered. Figures 12 and 13 show the comparison between the measurement data acquired in the shear tests and the numerical simulations performed with the above parameters, which were obtained by means of a least-square fitting technique. In particular, Fig. 12 displays the displacement out of the shear plane in that point where the maximum value is attained versus the prescribed shear displacement, while Fig. 13 displays the global shear force reaction versus the imposed shear displacement. The blue solid line in these figures represents the numerical solution; the dotted line represents the experimental measures. Measurements and theoretical predictions are in good agreement within the measurement errors shown as vertical and horizontal red bars.

FEM analyses have been performed by means of the software COMSOL Multiphysics®. The mesh was triangular and advancing front tessellated. Boundary conditions have been prescribed weakly by means of Lagrange multipliers. For the displacement u, we have used Argyris quintic basis functions.

The experimental behavior is characteristic of buckling, which is due to the presence of some imperfections. Such behavior is clearly detectable in Fig. 12 by following the post-buckling path, namely the fillet between the trivial behavior (plane deformation) and the presence of an out-of-plane displacement. For this reason, to properly compare the experiment and the simulation, we add some small defects also in the numerical analysis, directly connected to the features of the testing machine. Indeed, we consider an initial torsion of the whole sample of about 1.64 degrees as well as a small compression of 0.5 mm along the longitudinal direction of the specimen. In addition, we consider also, as a little perturbation, a distributed couple applied to the long edges of the sample. The use of this last imperfection is related to the fact that the two families of fibers are not on the

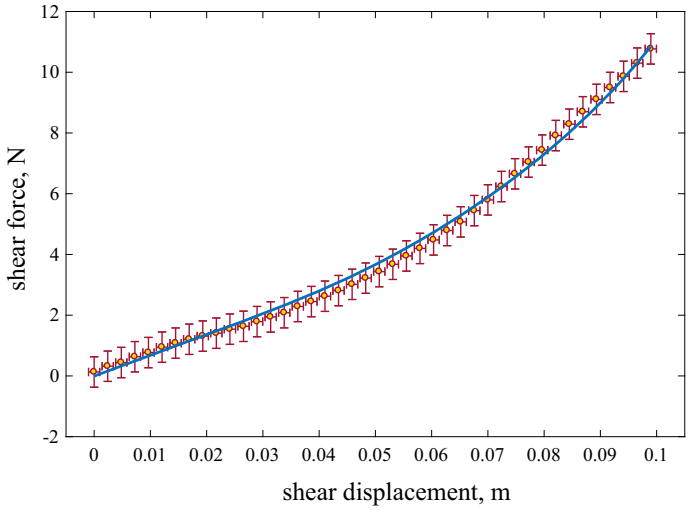

Fig. 13 Shear force reaction versus prescribed shear displacement: comparison between measurements and numerical simulations. Numerical solution (solid line); experimental measures (dotted line). Errors (vertical and horizontal red bars) (color figure online)

same plane, but there is an offset between them. This offset breaks the symmetry of the system and, therefore, it facilitates the emergence of buckling in one direction before that the critical displacement is imposed.

4 Conclusions

In this paper, experimental results relative to displacement-controlled large deformation shear loading tests of pantographic samples, produced with the aid of 3D printing using polyamide powder as raw material, have been reported. In particular, five differently sized samples have been analyzed up to first rupture. Their response to the deformation has been recorded by a force transducer and an optical 3D measurement system. Subsequently, digital image correlation (DIC) has been used to compute the deformation out of the shearing plane by the help of a two-camera system. Results show that the deformation behavior is strongly nonlinear, and the structures are capable of undergoing large elastic deformations without reaching complete failure. The experimental setup has been thoroughly described, and experimental results are being reported. An insight into the complex interplay of different phenomena involved in the buckling observed in all the experiments has been provided, arguing that buckling out of the shear plane is probably due to the competition of two different local deformation mechanisms. On one side, the geodesic bending deformation of fibers, i.e., the bending deformation along the plane tangent to the equivalent deformed surface representing the deformed 3D specimen. On the other side, the bending deformation of the fibers out of the plane tangent to the equivalent deformed surface and, subsequently, their twisting. Depending on whether the stiffness to in-plane bending of the beams is relatively larger than that to out-of-plane bending or not, the former or the latter behavior is observed. Then, the main features of a recently proposed model suitable to describe the out-of-plane buckling are outlined and the comparison between the measurement data acquired in the shear tests and the numerical simulations performed with the above parameters, which were obtained by means of a least-square fitting technique, has been presented. We want to remark that, clearly, the deformation energy of the continuum model employed in this paper can be seen as the limit, in a suitable sense, of the deformation energy of the assembly of a finite number of beams, as this number tends to infinity. In this sense, it is known that, for instance, in statistical mechanics some rigorous results are obtained proving how one can get fluid continua from discrete microscopic systems (see [31,52]). The inclusion in such homogenization frameworks of thermal phenomena is an open challenge for systems behaving macroscopically as fluids (see the e.g., [9–11,15,16]) as well as the determination, via statistical mechanics and rigorous arguments, of micro-properties leading, at macro-level, to solid behavior. The addition, in the numerical analysis, of some small defects, directly connected to the features of the testing machine, has been discussed as well in order to motivate the emergence of buckling. We believe to be able to conclude that pantographic fabrics proved again to be an interesting subject of study: Their use in engineering application is still far from being reality, but it is already promising, and they are

the source of a plethora of phenomena which can be properly described only by means of advanced modeling techniques and by carrying out serious measurement campaigns.

Acknowledgements The authors would like to thank F. dell'Isola and T. Lekszycki for helpful comments and advices through the study. A special thank to I. Giorgio and N. L. Rizzi for the interesting discussions about the two-dimensional continuum model adopted.

References

1. Alibert, J.-J., Seppecher, P., dell'Isola, F.: Truss modular beams with deformation energy depending on higher displacement gradients. Math. Mech. Solids **8**(1), 51–73 (2003)
2. Altenbach, H., Eremeyev, V.: On the constitutive equations of viscoelastic micropolar plates and shells of differential type. Math. Mech. Complex Syst. **3**(3), 273–283 (2015)
3. Andreaus, U., Baragatti, P.: Experimental damage detection of cracked beams by using nonlinear characteristics of forced response. Mech. Syst. Signal Process. **31**, 382–404 (2012)
4. Barchiesi, E., Placidi, L.: A review on models for the 3D statics and 2D dynamics of pantographic fabrics. In: Wave Dynamics and Composite Mechanics for Microstructured Materials and Metamaterials, pp. 239–258. Springer (2017)
5. Battista, A., Cardillo, C., Del Vescovo, D., Rizzi, N.L., Turco, E.: Frequency shifts induced by large deformations in planar pantographic continua. Nanomech. Sci. Technol.: Int. J. **6**(2), 161–178 (2015)
6. Battista, A., Del Vescovo, D., Rizzi, N.L., Turco, E.: Frequency shifts in natural vibrations in pantographic metamaterials under biaxial tests. Technische Mechanik **37**(1), 1–17 (2017)
7. Bertram, A., Glüge, R.: Gradient materials with internal constraints. Math. Mech. Complex Syst. **4**(1), 1–15 (2016)
8. Boutin, C., dell'Isola, F., Giorgio, I., Placidi, L.: Linear pantographic sheets: asymptotic micro–macro models identification. Math. Mech. Complex Syst. **5**(2), 127–162 (2017)
9. Caprino, S., Esposito, R., Marra, R., Pulvirenti, M.: Hydrodynamic limits of the vlasov equation. Commun. Partial Differ. Equ. **18**(5–6), 805–820 (1993)
10. Carinci, G., De Masi, A., Giardinà, C., Presutti, E.: Hydrodynamic limit in a particle system with topological interactions. Arab. J. Math. **3**(4), 381–417 (2014)
11. Carinci, G., De Masi, A., Giardinà, C., Presutti, E.: Super-hydrodynamic limit in interacting particle systems. J. Stat. Phys. **155**(5), 867–887 (2014)
12. Chatzigeorgiou, G., Javili, A., Steinmann, P.: Multiscale modelling for composites with energetic interfaces at the micro-or nanoscale. Math. Mech. Solids **20**(9), 1130–1145 (2015)
13. Cuomo, M., Contrafatto, L., Greco, L.: A variational model based on isogeometric interpolation for the analysis of cracked bodies. Int. J. Eng. Sci. **80**, 173–188 (2014)
14. Cuomo, M.: Forms of the dissipation function for a class of viscoplastic models. Math. Mech. Complex Syst. **5**(3), 217–237 (2017)
15. De Masi, A., Merola, I., Presutti, E., Vignaud, Y.: Coexistence of ordered and disordered phases in potts models in the continuum. J. Stat. Phys. **134**(2), 243–306 (2009)
16. De Masi, A., Olla, S.: Quasi-static hydrodynamic limits. J. Stat. Phys. **161**(5), 1037–1058 (2015)
17. Del Vescovo, D., Giorgio, I.: Dynamic problems for metamaterials: review of existing models and ideas for further research. Int. J. Eng. Sci. **80**, 153–172 (2014)
18. dell'Isola, F., Andreaus, U., Placidi, L.: At the origins and in the vanguard of peridynamics, non-local and higher-gradient continuum mechanics: An underestimated and still topical contribution of Gabrio Piola. Math. Mech. Solids **20**(8), 887–928 (2015)
19. dell'Isola, F., Della Corte, A., Giorgio, I.: Higher-gradient continua: the legacy of Piola, Mindlin, Sedov and Toupin and some future research perspectives. Math. Mech. Solids **22**(4), 852–872 (2017)
20. dell'Isola, F., Della Corte, A., Giorgio, I., Scerrato, D.: Pantographic 2D sheets: discussion of some numerical investigations and potential applications. Int. J. Non-linear Mech. **80**, 200–208 (2016)
21. dell'Isola, F., Della Corte, A., Greco, L., Luongo, A.: Plane bias extension test for a continuum with two inextensible families of fibers: A variational treatment with lagrange multipliers and a perturbation solution. Int. J. Solids Struct **81**, 1–12 (2015)
22. dell'Isola, F., Giorgio, I., Andreaus, U.: Elastic pantographic 2D lattices: a numerical analysis on static response and wave propagation. Proc. Eston. Acad. Sci. **64**(3), 219–225 (2015)
23. dell'Isola, F., Giorgio, I., Pawlikowski, M., Rizzi, N.: Large deformations of planar extensible beams and pantographic lattices: heuristic homogenization, experimental and numerical examples of equilibrium. Proc. R. Soc. A **472**(2185), 23 (2016)
24. dell'Isola, F., Lekszycki, T., Pawlikowski, M., Grygoruk, R., Greco, L.: Designing a light fabric metamaterial being highly macroscopically tough under directional extension: first experimental evidence. Zeitschrift für angewandte Mathematik und Physik **66**, 3473–3498 (2015)
25. dell'Isola, F., Placidi, L.: Variational principles are a powerful tool also for formulating field theories. In: Variational Models and Methods in Solid and Fluid Mechanics, pp. 1–15. Springer (2011)
26. dell'Isola, F., Steigmann, D., Della Corte, A.: Synthesis of fibrous complex structures: designing microstructure to deliver targeted macroscale response. Appl. Mech. Rev. **67**(6), 060804 (2015)
27. dell'Isola, F., Steigmann, D.J.: A two-dimensional gradient-elasticity theory for woven fabrics. J. Elast. **18**, 113–125 (2015)
28. dell'Isola, F., Della Corte, A., Esposito, R., Russo, L.: Some cases of unrecognized transmission of scientific knowledge: from antiquity to gabrio piola's peridynamics and generalized continuum theories. In: Generalized continua as models for classical and advanced materials, pp. 77–128. Springer (2016)

29. Dietrich, L., Lekszycki, T., Turski, K.: Problems of identification of mechanical characteristics of viscoelastic composites. Acta Mech. **126**(1), 153–167 (1998)
30. Engelbrecht, J., Berezovski, A.: Reflections on mathematical models of deformation waves in elastic microstructured solids. Math. Mech. Complex Syst. **3**(1), 43–82 (2015)
31. Esposito, R., Pulvirenti, M.: From particles to fluids. Handbook of mathematical fluid dynamics **3**, 1–82 (2004)
32. Eugster, S.R., dell'Isola, F.: Exegesis of the introduction and Sect. I from "Fundamentals of the mechanics of continua"** by E. Hellinger. ZAMM-J. Appl. Math. Mech./Zeitschrift für Angewandte Mathematik und Mechanik **97**(4), 477–506 (2017)
33. Eugster, S.R., dell'Isola, F.: Exegesis of Sect. II and III. A from "Fundamentals of the mechanics of continua"** by E. Hellinger. ZAMM-J. Appl. Math. Mech./Zeitschrift für Angewandte Mathematik und Mechanik (2017). https://doi.org/10.1002/zamm.201600293
34. Ganzosch, G., dell'Isola, F., Turco, E., Lekszycki, T., Müller, W.H.: Shearing tests applied to pantographic structures. Acta Polytechnica CTU Proceedings **7**, 1–6 (2016)
35. Giorgio, I., Della Corte, A., dell'Isola, F.: Dynamics of 1D nonlinear pantographic continua. Nonlinear Dyn. **88**(1), 21–31 (2017)
36. Giorgio, I., Della Corte, A., dell'Isola, F., Steigmann, D., Steigmann, D.: Buckling modes in pantographic lattices. C.R. Mec. **344**, 487–501 (2016)
37. Giorgio, I., Rizzi, N.L., Turco, E.: Continuum modelling of pantographic sheets for out-of-plane bifurcation and vibrational analysis. Proc. R. Soc. A **473**(2207), 21 (2017)
38. Giorgio, I., Scerrato, D.: Multi-scale concrete model with rate-dependent internal friction. Eur. J. Environ. Civ. Eng. **21**(7–8), 821–839 (2017)
39. Greco, L., Giorgio, I., Battista, A.: In plane shear and bending for first gradient inextensible pantographic sheets: numerical study of deformed shapes and global constraint reactions. Math. Mech. Solids **22**(10), 1950–1975 (2017)
40. Harrison, P.: Modelling the forming mechanics of engineering fabrics using a mutually constrained pantographic beam and membrane mesh. Compos. A Appl. Sci. Manuf. **81**, 145–157 (2016)
41. Kocsis, A., Challamel, N., Károlyi, G.: Discrete and nonlocal models of engesser and haringx elastica. Int. J. Mech. Sci. **130**, 571–585 (2017)
42. Melnik, A.V., Goriely, A.: Dynamic fiber reorientation in a fiber-reinforced hyperelastic material. Math. Mech. Solids **18**(6), 634–648 (2013)
43. Milton, G., Briane, M., Harutyunyan, D.: On the possible effective elasticity tensors of 2-dimensional and 3-dimensional printed materials. Math. Mech. Complex Syst. **5**(1), 41–94 (2017)
44. Misra, A.: Effect of asperity damage on shear behavior of single fracture. Eng. Fract. Mech. **69**(17), 1997–2014 (2002)
45. Misra, A.: Mechanistic model for contact between rough surfaces. J. Eng. Mech. **123**(5), 475–484 (1997)
46. Nadler, B., Steigmann, D.J.: A model for frictional slip in woven fabrics. Comptes Rendus Mec. **331**(12), 797–804 (2003)
47. Pideri, C., Seppecher, P.: A second gradient material resulting from the homogenization of an heterogeneous linear elastic medium. Continuum Mech. Thermodyn. **9**(5), 241–257 (1997)
48. Placidi, L., Andreaus, U., Della Corte, A., Lekszycki, T.: Gedanken experiments for the determination of two-dimensional linear second gradient elasticity coefficients. Zeitschrift für angewandte Mathematik und Physik **66**(6), 3699–3725 (2015)
49. Placidi, L., Andreaus, U., Giorgio, I.: Identification of two-dimensional pantographic structure via a linear D4 orthotropic second gradient elastic model. J. Eng. Math. **103**(1), 1–21 (2016)
50. Placidi, L., Barchiesi, E., Turco, E., Rizzi, N.L.: A review on 2D models for the description of pantographic fabrics. Zeitschrift für angewandte Mathematik und Physik **67**(5), 121 (2016)
51. Russo, L.: The Forgotten Revolution: How Science was Born in 300 BC and Why It had to be Reborn. Springer, Berlin (2013)
52. Saint-Raymond, L.: Hydrodynamic Limits of the Boltzmann Equation. Springer, Berlin (2009)
53. Scerrato, D., Giorgio, I., Rizzi, N.: Three-dimensional instabilities of pantographic sheets with parabolic lattices: numerical investigations. Zeitschrift für angewandte Mathematik und Physik **67**(3), 1–19 (2016)
54. Spagnuolo, M., Barcz, K., Pfaff, A., dell'Isola, F., Franciosi, P.: Qualitative pivot damage analysis in aluminum printed pantographic sheets: numerics and experiments. Mechanics Research Communications (2017)
55. Steigmann, D.J., dell'Isola, F.: Mechanical response of fabric sheets to three-dimensional bending, twisting, and stretching. Acta Mech. Sin. **31**(3), 373–382 (2015)
56. Stigler, S.M.: Stigler's law of eponymy. Transactions of the New York Academy of Sciences **39**(1 Series II), 147–157 (1980)
57. Turco, E., dell'Isola, F., Cazzani, A., Rizzi, N.L.: Hencky-type discrete model for pantographic structures: numerical comparison with second gradient continuum models. Zeitschrift für angewandte Mathematik und Physik **67**, 28 (2016)
58. Turco, E., dell'Isola, F., Rizzi, N.L., Grygoruk, R., Müller, W.H., Liebold, C.: Fiber rupture in sheared planar pantographic sheets: numerical and experimental evidence. Mech. Res. Commun. **76**, 86–90 (2016)
59. Turco, E., Golaszewski, M., Giorgio, I., D'Annibale, F.: Pantographic lattices with non-orthogonal fibres: experiments and their numerical simulations. Compos. B Eng. **118**, 1–14 (2017)
60. Victor, A.: Eremeyev and Wojciech Pietraszkiewicz. Material symmetry group and constitutive equations of micropolar anisotropic elastic solids. Math. Mech. Solids **21**(2), 210–221 (2016)

4.4 The making and testing of FDM and SLA printed pantographic sheets

[4]: Gregor Ganzosch, Christina Völlmecke, Emilio Barchiesi, and Wolfgang H. Müller. The making and testing of FDM and SLA printed pantographic sheets. *Elasticity and Anelasticity,* Moscow State Univ. Publ., 57—66, 2021.

This is the preprint version.

Abstract: Meta-materials with a pantographic substructure were manufactured additively by using fused deposition modeling and stereolithography. Samples of two different materials, polylactide and epoxy resin, are loaded in standard extension and shearing tests leading to large elastic deformations. 2D-digital image correlation is used to quantify the deformation. Results also show highly resilient deformation behavior making this structures very useful for technical applications in lightweight industries.

Status: *"published"*. The authors own their preprints (`https://www.elibrary.ru/item.asp?id=47390305&pff=1`).

ISBN: 978-5-19-011626-7

The making and testing of FDM and SLA printed pantographic sheets

Gregor Ganzosch
Technische Universität Berlin
Department of Mechanics
Chair of Continuum Mechanics and Constitutive Theory
Einsteinufer 5
10587 Berlin
Germany,
ganzosch@tu-berlin.de

Christina Völlmecke
Technische Universität Berlin
Department of Mechanics
Chair of Stability and Failure of Functionally Optimized Structures
Einsteinufer 5
10587 Berlin
Germany,
christina.voellmecke@tu-berlin.de

Emilio Barchiesi
International Research Center on
Mathematics and Mechanics of Complex Systems
Università degli Studi dell'Aquila
Via Giovanni Gronchi 18
Zona industriale di Pile, 67100, L'Aquila (Italy)
barchiesiemilio@gmail.com

Wolfgang H. Müller
Technische Universität Berlin
Department of Mechanics
Chair of Continuum Mechanics and Constitutive Theory
Einsteinufer 5
10587 Berlin
Germany,
wolfgang.h.mueller@tu-berlin.de

Abstract

Meta-materials with a pantographic substructure were manufactured additively by using fused deposition modeling and stereolithography. Samples of two different materials, polylactide and epoxy resin, are loaded in standard extension and shearing tests leading to large elastic deformations. 2D-digital image correlation is used to quantify the deformation. Results also show highly resilient deformation behavior making this structures very useful for technical applications in lightweight industries.

Keywords: additive manufacturing, experiment, elasticity, digital image correlation, pantographic structure

1 Introduction

New developments in additive manufacturing technology enable the combination of special tailored structures with custom designed materials resulting and form a new class of materials, the so-called meta-materials. Meta-materials show an extraordinary deformation behavior at the macroscopic scale, which, as a consequence, is controlled by the custom-tailored substructure. Pantographic Structures (PS), which can be described as meta-materials with substructures composed of two orthogonal arrays of beams [19–21], connected by internal cylinders ("pivots," see Fig. 1), were manufactured by using two different additive manufacturing techniques - Fused Deposition Modeling (FDM) and Stereo-Lithographic Addition (SLA).

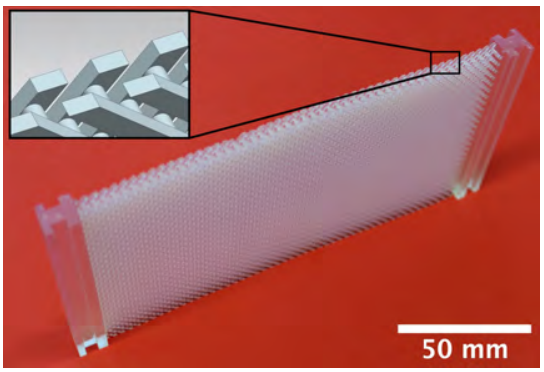

Figure 1: Pantographic structure developed by [1]; manufactured at the Institute of Mechanics at Technische Universität Berlin by means of SLA.

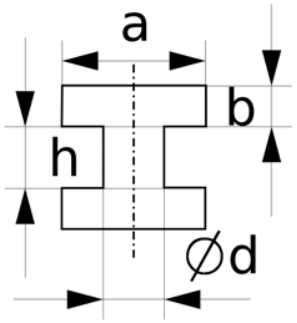

Figure 2: Two-dimensional cross-section of a unit cell of a pantographic substructure.

In order to achieve large elastic deformation behavior, material and geometric properties are carefully chosen by designing the so-called microscopic constituents [1–3] in the substructure. Therefore the mechanical performance

of PSs depends not only on the global structure, but also on the morphology of the periodically repeated unit cells in the substructure. Such effects have been investigated, for example in [22–27].

In order to make meta-materials useful for specific engineering applications, finite element methods [4, 5] can be used to predict the deformations. Calculations with this powerful tool are normally based on the constitutive assumption of a CAUCHY-BOLTZMANN continuum. Alternatively pantographic meta-materials can also be modeled by a higher gradient theory [2, 6, 28–42].

Here, new material parameters are introduced and specially adjusted experiments have been designed to determine these values of these parameters [7–11]. On the one hand, the newly identified parameters gained from theory have to be measured and determined in experiments [8, 9], and on the other hand the values for the parameters obtained by theory or from numerical analysis have to been validated by experiments [12, 13, 43, 44].

2 Materials and Methods

Two different types of materials, PolyLactide Acid (PLA) and Epoxy Resin (ER), are used as raw material to manufacture the pantographic sheets additively by means of FDM and SLA (see Subsect. 2.1). Standard extension and shearing experiments are performed to test the elastic deformation behavior of those pantographic sheets (see Subsect. 2.2). In addition, a non-invasive optical measurement technique, so-called Digital Image Correlation (DIC), is used to measure the deformation on the specimens' surface and to validate numerical results (see the Results sections).

2.1 Manufacturing

Pantographic structures, consisting of rectangular-cross-section beams linked by cylinders, were 3D-printed using two different additive manufacturing methods:

i) FDM by means of an Ultimaker 3 Extended (Ultimaker B.V., Geldermalsen, Netherlands) available at Technische Universität Berlin, Chair of Stability and Failure of Functionally Optimized Structures, Germany,

ii) SLA by means of Formlabs 2 (Formlabs, Inc., Somerville, MA, USA) located at Technische Universität Berlin, Chair of Stability and Failure of Functionally Optimized Structures, Germany.

PLA (Ultimaker B.V., Geldermalsen, Netherlands) was used as raw material for FDM (specimen **PLA**). In order to increase the printing quality of the specimen, water-soluble PolyVinyl Alcohol (PVA, Ultimaker B.V., Geldermalsen, Netherlands) was used additionally as a support-structure during the printing process (see Fig. 3) to fill the cavities. The whole print was put into regular

tap water at room temperature for 24 hours afterwards, so that the support structure could vanish (for further informations see [14]). Epoxy resin (Clear

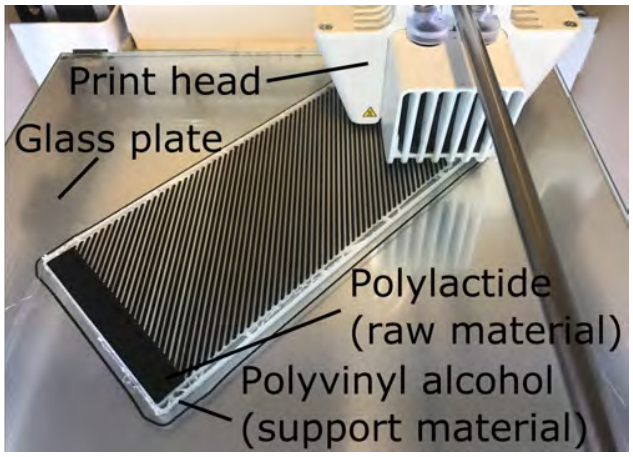

Figure 3: Picture of the specimen **PLA** during the manufacturing process by means of FDM. Two print cores enable synchronized printing of the raw material (PLA) and of the support material (PVA) on a heated glass plate (60°C) layer by layer.

RS-F2-GPCL-04, Formlabs, Inc., Somerville, MA, USA) was used as raw material in SLA (specimen **ER**). A special support structure was employed in order to avoid distortions due to the bottom-up manufacturing process by printing in layers. The remaining resin was washed off in 2-propanol-liquid by means of the orm Wash device (Formlabs, Inc., Somerville, MA, USA). Furthermore, a hardening treatment for 20 minutes at 60°C in the Form Cure device (Formlabs, Inc., Somerville, MA, USA) was performed on sample **ER** resulting in a stiffening of the specimen. Notice that all material properties vary with print orientation, geometry, and print settings (temperature, printing velocity, etc.). Since the microscopic substructures influence the macroscopic deformation behaviors significantly [15], specimens with different cylindric lengths were investigated as well. Fig. 4 shows both types of specimens (sample **PLA** and **ER**). In total eight specimens were investigated, four in extension tests and four in shearing tests, respectively. Details of the inner and outer dimensions of all samples can be found in Tab. 1.

2.2 Experimental Setup

Experiments are divided into extension and shearing tests. All experiments have been performed on a MTS Tytron 250 testing device (MTS Systems Corporation, Eden Prairie, MN, USA) located at Technische Universität Berlin, Chair of Continuum Mechanics and Constitutive Theory. Displacement-controlled and quasi-static standard tests have been taken into account. The experimental

Sample	L	l	t	a	b	d	h	Extension	Shearing
PLA1	140	70	3	1	1	0.9	1	x	
PLA2	140	70	3	1	1	0.9	1		x
PLA3	140	70	5	1	1	0.9	3	x	
PLA4	140	70	5	1	1	0.9	3		x
ER1	140	70	3	1	1	0.9	1	x	
ER2	140	70	3	1	1	0.9	1		x
ER3	140	70	5	1	1	0.9	3	x	
ER4	140	70	5	1	1	0.9	3		x

Table 1: Outer dimensions in mm (L = width, l = height, t = depth) and inner dimensions of the substructure in mm corresponding to the schematic in Fig. 2 (a = width of beam, b = height of beam, d = diameter of pivot, h = height of pivot). Distance between beams of all specimens is 1 mm.

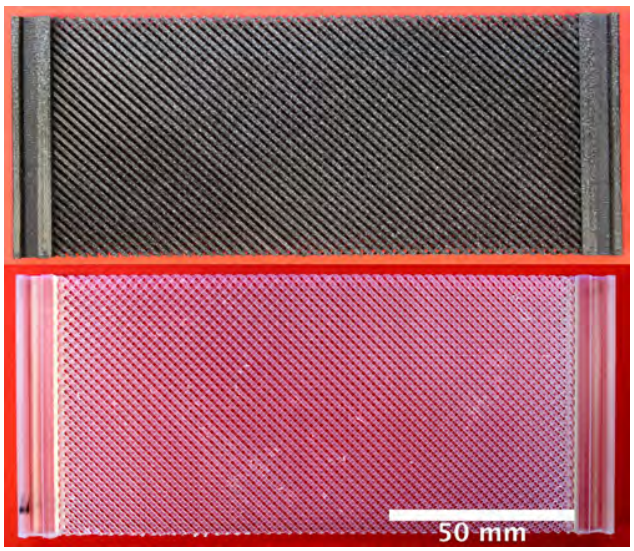

Figure 4: Front view of pantographic structures made out of polylactide **PLA** (top) and epoxy resin **ER** (bottom).

setup of extension test performed on sample **PLA** is shown in Fig. 5; the experimental setup of shearing-test performed on sample **ER** is presented in Fig. 6.

The MTS Tytron 250 testing-device is controlled by the software Stationsmanager V 3.14. The applied force was measured by a device-own loading cell being able to record axial forces in a range of $F = \pm 250\,\mathrm{N}$ with a precision of about ± 25 mN. The displacement x was imposed horizontally with a loading rate of $v = 15\,\mathrm{mm/min}$. The displacement was measured and monitored by the device-own encoder unit. Almost frictionless movement was achieved by using

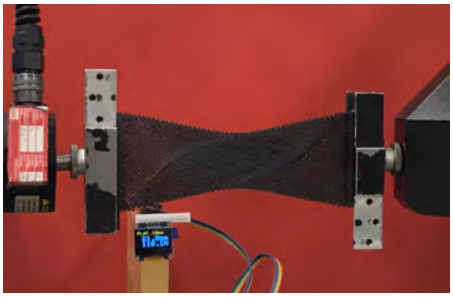

Figure 5: Side-view of setup of extension test of sample **PLA** performed on the MTS Tytron 250 testing device. Loading cell on the left; left mounting is fixed; displacement is imposed horizontally at the right mounting side.

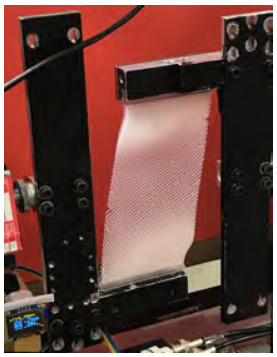

Figure 6: Side-view of setup of shearing test of sample **ER** performed on the MTS Tytron 250 testing device. An out-of-plane displacement can be recognized.

an air-film-bearing. External vibration was avoided by using a massive substructure and by arranging the system horizontally. Additionally, a non invasive optical deformation technique - Digital Image Correlation (DIC) - was performed in all tests. Pictures were taken (0.25 pictures/second) by means of a commercial Canon EOS 1000D camera with a resolution of 4272 x 2848 pixels. For connecting the camera and the testing device a TTL bridge was used. The TTL signal is able to synchronize each picture with the related force- and displacement-value in real time. 2D-DIC evaluation was performed in open-source GOM Correlate 2019 software (GOM GmbH, Braunschweig, Germany). Because of the lack of contrast the black specimen **PLA** was speckled with white ink by means of an airbrush tool (for further informations see [7]).

3 Results - Extension

Fig. 7 shows the results of samples **ER1, ER3, PLA1, PLA3** of the biaxial tension test in a stress/strain diagram. Obviously, elastic performance as seen in previously investigated experimental studies (see [1,15]) was also experienced in all specimens. However, the small heights (1mm) of the cylindric pivots of samples **ER1** and **PLA1** resulted in a kind of an-elasticity (see [16]). In order to avoid this, samples **EP3** and **PLA3** with three times larger pivot height (3mm) were tested resulting in linear elastic deformation behavior up to about 3.5 % of elongation. Consequently, plastic deformation, which is shown by the negative stress values beneath the x-axis, and visco-elasticity, which is shown by the non-linear lower-valued regime, must be taken into account as well. For further informations see [4]. Fig. 8 illustrates the 2D-DIC evaluation and linear elastic FE analysis of specimen **EP1** during an extension test. The

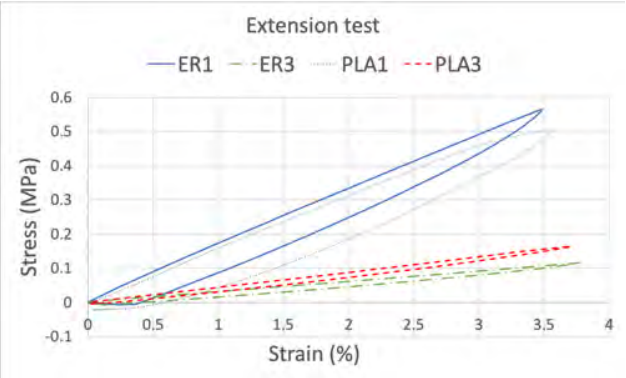

Figure 7: Stress-strain curves of biaxial extension tests of specimen **ER1, ER3, PLA1, PLA3** performed on MTS Tytron 250 device.

amount of deformation based on the MTS machine code differs by less than 0.5% from the DIC calculation. Necking, calculated by means of 2D-DIC in vertical direction, results in a shortening in vertical direction of about $\Delta y_{\mathbf{DIC}} = 1.7\,\mathrm{mm}$ ($\Delta y_{\mathbf{FEM}} = 1.9\,\mathrm{mm}$, respectively). This corresponds well to the results reported in [14] for specimens consisting of polyamide.

YOUNG's moduli of PLA and ER were determined with the help of a device-own laser extensometer of the MTS Tytron 250 testing machine by testing specially developed specimens with higher radii than the standard test specimen (see Fig. 9). The measured values of the elastic moduli E differ from the parameters provided by the manufacturer (see Tab. 2). This may be caused by different print orientations, non-consistent geometries or print resolutions (depending strongly on additive manufacture technique), porosity, and print settings, such as temperature or printing velocity. Figure 10 compares the stress-strain rela-

Sample	Manufacturer	Measured at TU Berlin
E_{PLA}	2346 MPa (Ultimaker B.V.)	2200 MPa
E_{ER}	1600 - 2800 MPa (Formlabs, Inc.)	2100 MPa

Table 2: Comparison of elastic moduli of PLA (E_{PLA}) and ER (E_{ER}). Manufacturers' values are higher than the measured ones.

tions of samples **ER1** and **PLA1** during tension experiments with the numerical results by means of FEM based on the material parameters measured at TU Berlin. Obviously, the analysis based on classic CAUCHY-BOLTZMANN continuum is sufficient to model the isotropic deformation behavior of pantographic sheets for elongations up to 3 % in standard extension tests.

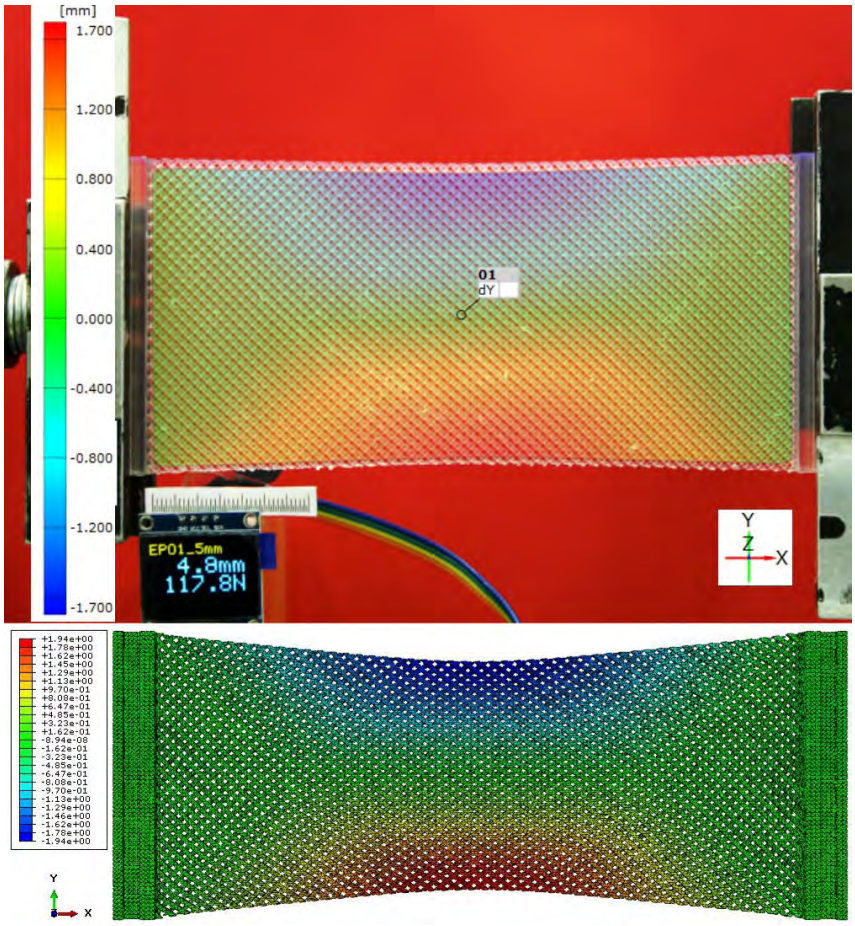

Figure 8: Vertical displacement (in y-direction) by means of DIC (top) and FEM (bottom) of sample **ER1** at about 3 % of axial elongation during extension test.

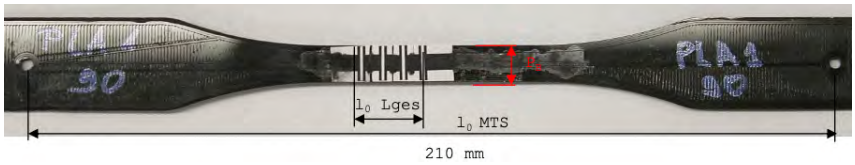

Figure 9: Example of a test specimen made out of PLA which was used to determine the material parameter (elastic modulus) by means of a laser extensometer is shown. Vertical lines are used as reference for the laser calculations in the region of interest L_{ges}.

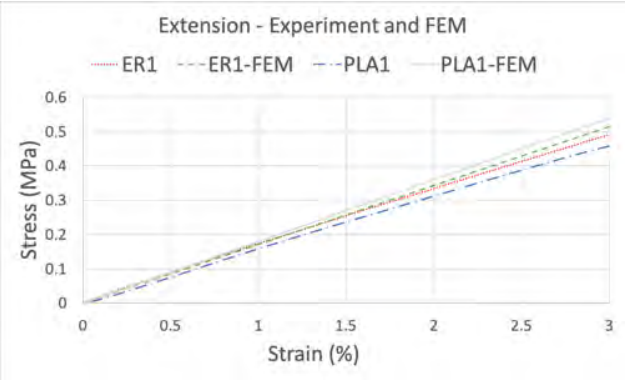

Figure 10: Comparison of stress-strain relations of biaxial extension tests of specimen **ER1, PLA1** obtained from real experiments and numerical analysis (classic linear elastic calculation based on CAUCHY-BOLTZMANN continuum using Abaqus by means of 430917 quadratic tetrahedral elements of type C3D10).

4 Results - Shearing

Fig. 11 shows results of samples **ER2, ER4, PLA2, PLA4** of shearing test in a shear-stress/shear-strain diagram. Samples **ER4, PLA4** show linear elastic shear deformations up to an elongation of about 7 %. In contrast to that the samples **ER2, PLA2** show non-linear deformation behavior. Sample **ER2** shows a significantly higher resistance to outer loads than sample **PLA2**. Because of the stiffnesses of the pivots, which connect the arrays of beams from the different planes, out-of-plane buckling occurs (see Fig. 6), being in good agreement with previous investigations reported in [7, 15, 17]. Furthermore, after leaving the elastic range, plastic rotation of the pivots becomes so high that the beams touch each others resulting in higher dissipation. One may say that the "shearing test becomes an elongation test" at this very point. Fig. 12 shows results of shear deformation of samples **ER4, PLA4** under large shearing loading conditions. Linear elastic deformation of sample **ER4** can be recognized up to an elongation of about $\Delta e_{yy} = 8.2$ %. Total failure occurs at about $\Delta e_{yy} = 55$ % of shear-elongation at almost 0.228 MPa. Linear elastic deformation of sample **PLA4** can be recognized up to an elongation of about $\Delta e_{yy} = 11.8$ %. The first rupture occurs at about $\Delta e_{yy} = 26.2$ % of shear-elongation at almost 0.115 MPa. The whole metamaterial is able to resist even further loading without leading to total failure resulting in a high resilient deformation behavior. Even after the second rupture at about $\Delta e_{yy} = 49$ % of shear-elongation, the whole structure does not fail and is able to resist further (lower) loads without leading to total failure.

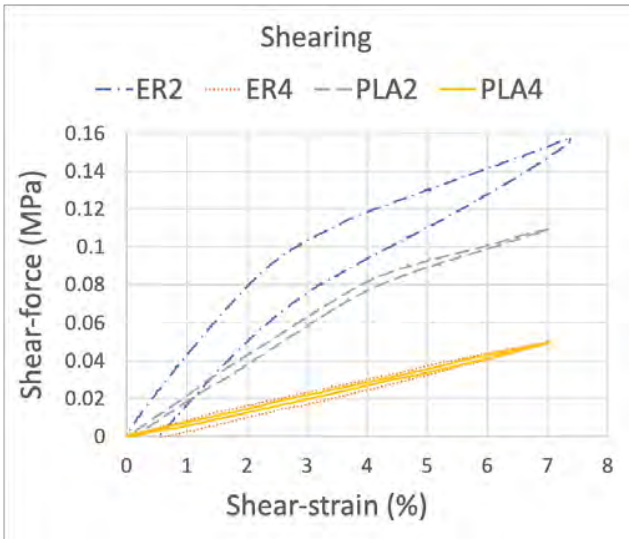

Figure 11: Shear-stress/shear-strain relations during shearing tests of specimen **ER2, ER4, PLA2, PLA4** performed on MTS Tytron 250 device.

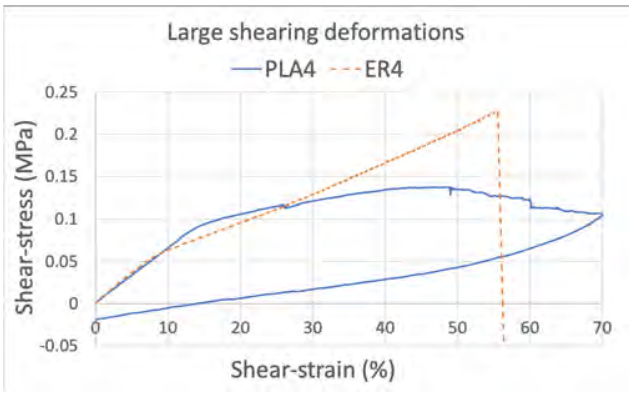

Figure 12: Shear-stress/shear-strain relations during shearing tests of specimen **ER4, PLA4** performed for large deformations on MTS Tytron 250 device.

5 Conclusions

Pantographic structures made out of two different materials were manufactured additively using two different types of additive manufacturing techniques - Fused Deposition Modeling (FDM) and StereoLithographic Addition (SLA). Polylactide Acid (PLA) was used as a raw material for 3D-printing of specimen **PLA** by means of FDM. Epoxy resin was used as a raw material for 3D-printing of specimen **ER** by means of SLA.

Extension tests were performed on specimens **PLA1, PLA3, ER1, ER3**, shearing tests on specimens **PLA2, PLA4, ER2, ER4**. In parallel, 2D image correlation was performed to validate the values for the deformations.

Specimens **PLA3, PLA4, ER3, ER4** (consisting of larger pivot-heights with 3 mm) deformed in a linear elastic way in all tests for small ($\Delta e_{yy} \leq 3$ %) as well as for large deformations ($\Delta e_{yy} \geq 3$ %). In extension tests, an-elastic deformation occurred for **PLA1, ER1** for small deformations. In shearing tests, viscoelastic as well as plastic phenomena occurred for samples **PLA2, ER2**, which was also reported in [4] for specimens made out of polyamide. Furthermore, strong resilient deformation behavior was observed for large deformations in shearing. This extraordinary property of pantographic metamaterials may be used in failure-safe systems in future applications to secure stability of mechanical systems, *e.g.*, in aircraft or automobile industries. In contrast to investigations that can be found in [16], out-of-plane buckling was observed during shearing tests applied to specimens **ER2, EP4, PLA2, PLA4** due to the non-perfect pivots/joints. Independently, the aforementioned resilient deformation behavior was also observed for extension tests with specimens made out of PLA, which is in good agreement with previous investigations reported in [14].

One may say that because of the ability of pantographic meta-materials to stay in the (linear) elastic range, even at large deformations, such structures will play a crucial role for different kind of industrial applications in the future. Its light weight in combination with its high resilient and elastic deformation behavior makes this kind of meta-material very attractive to serve as a specially tailored application in different branches of industry, (*e.g.*, for protection shields in civil industries, damping or mounting device in aircraft or automobile industries).

References

[1] dell'Isola, F. and Lekszycki, T. and Pawlikowski, M. and Grygoruk, R. and Greco, L.: Designing a light fabric metamaterial being highly macroscopically tough under directional extension: First experimental evidence. Zeitschrift für Angewandte Mathematik und Physik, 2015, 66(6), pp. 3473-3498.

[2] Barchiesi, E. and Spagnuolo, M. and Placidi, L.: Mechanical metamaterials: a state of the art. Mathematics and Mechanics of Solids, 2018, 24(1), pp. 212?234.

[3] Gibson, L.J. and Ashby, M.F.: Cellular solids: structure and properties. Structure and Properties. Cambridge Solid State Science Series, 1995, pp. 52-92.

[4] Yang, H. and Ganzosch, G. and Giorgio, I. and Abali, B.E.: Material characterization and computations of a polymeric metamaterial with a panto-

graphic substructure. Zeitschrift für angewandte Mathematik und Physik, 2018, 69(4), 105.

[5] Chen, C and Fleck, N.A.: Size effects in the constrained deformation of metallic foams. Journal of the Mechanics and Physics of Solids, 2002, 50(5), pp. 955-977.

[6] dell'Isola, F. and Cuomo, M. and Greco, L. and Della Corte, A.: Bias extension test for pantographic sheets: numerical simulations based on second gradient shear energies. Journal of Engineering Mathematics, 2017, 103(1).

[7] Ganzosch, G. and Hoschke, K. and Lekszycki, T. and Giorgio, I. and Turco, E. and Müller, W.H.: 3D-Measurements of 3D-Deformations of Pantographic Structures. Technische Mechanik, 2018, 38(3), pp. 233?245.

[8] Lam, D.C.C. and Yang, F. and Chong, A.C.M. and Wang, J. and Tong, P.: Experiments and theory in strain gradient elasticity. Journal of the Mechanics and Physics of Solids, 2003, 51(8), pp. 1477-1508.

[9] Liebold, C. and Müller, W.H.: Measuring Material Coefficients of Higher Gradient Elasticity by Using AFM Techniques and Raman-Spectroscopy. Advanced Structured Materials, 2013, 22, pp. 255?271.

[10] Wei, Y. and Wang, X. and Wu, X. and Bai, Y.: Theoretical and experimental researches of size effect in micro-indentation test. Science in China Series A: Mathematics, 2001, 44(1), pp. 1-74.

[11] Kong, S. and Zhou, S. and Nie, Z. and Wang, K.: Static and dynamic analysis of micro beams based on strain gradient elasticity theory. International Journal of Engineering Science, 2009, 47, pp. 487?498.

[12] Liebold, C. and Müller, W.H.: Applications of Higher-Order Continua to Size Effects in Bending: Theory and Recent Experimental Results. Advanced Structured Materials, 2016, 42, pp. 237?260.

[13] Turco, E. and dell'Isola, F. and Rizzi, N.L. and Grygoruk, R. and Müller, W.H. and Liebold, C.: Fiber rupture in sheared planar pantographic sheets: Numerical and experimental evidence. Mechanics Research Communications Elsevier, 2016, 76, pp 86-90.

[14] Juritza, A. and Yang, H. and Ganzosch, G.: Qualitative Investigations of Experiments Performed on 3D-FDM-printed Pantographic Structures Made out of PLA. New Achievements in Continuum Mechanics and Thermodynamics, Advanced Structured Materials, 2019, 108.

[15] Barchiesi, E. and Ganzosch, G. and Liebold, C. and Placidi, L. and Grygoruk, R. and Müller, W. H.: Out-of-plane buckling of pantographic fabrics in displacement-controlled shear tests: experimental results and model validation. Continuum Mechanics and Thermodynamics, 2018, 31, pp. 33?45.

[16] Spagnuolo, M. and Barcz, K. and Pfaff, A. and dell'Isola, F. and Franciosi, P.: Qualitative pivot damage analysis in aluminum printed pantographic sheets: numerics and experiments. Mechanics Research Communications, 2017, 83, pp. 47-52.

[17] Ganzosch, G. and dell'Isola, F. and Turco, E. and Lekszycki, T. and Müller, W.H.: Shearing tests applied to Pantographic Structures. Acta Polytechnica CTU Proceedings, 2017, 7, pp.1-6.

[18] Misra, A. and Lekszycki, T. and Giorgio, I. and Ganzosch, G. and Müller, W.H. and dell'Isola, F.: Pantographic metamaterials show atypical Poynting effect reversal. Mechanics Research Communications, 2018, 89, pp. 6-10.

[19] Dell'Isola, F., Corte, A. D., and Giorgio, I.: Higher-gradient continua: The legacy of Piola, Mindlin, Sedov and Toupin and some future research perspectives. Mathematics and Mechanics of Solids, 2017, 22(4), pp. 852-872.

[20] dell'Isola, F., Seppecher, P., Spagnuolo, M., Barchiesi, E., Hild, F., Lekszycki, T., ... and Eugster, S.R.: Advances in pantographic structures: design, manufacturing, models, experiments and image analyses. Continuum Mechanics and Thermodynamics, 2019, 31(4), pp. 1231-1282.

[21] dell'Isola, F., Seppecher, P., Alibert, J. J., Lekszycki, T., Grygoruk, R., Pawlikowski, M., ... and Golaszewski, M.: Pantographic metamaterials: an example of mathematically driven design and of its technological challenges. Continuum Mechanics and Thermodynamics, 2019, 31(4), pp. 851-884.

[22] Barchiesi, E., and Khakalo, S.: Variational asymptotic homogenization of beam-like square lattice structures. Mathematics and Mechanics of Solids, 2019, 24(10), pp. 3295-3318.

[23] dell'Isola, F., and Eremeyev, V.A.: Some Introductory and Historical Remarks on Mechanics of Microstructured Materials. Advanced Structured Materials, 2018, 87, pp. 1-20.

[24] Giorgio, I., Rizzi, N. L., and Turco, E.: Continuum modelling of pantographic sheets for out-of-plane bifurcation and vibrational analysis. Proceedings of the Royal Society A: Mathematical, Physical and Engineering Sciences, 2017, 473(2207).

[25] Turco, E.: How the properties of pantographic elementary lattices determine the properties of pantographic metamaterials. Advanced Structured Materials, 2019, 108, pp. 489-506.

[26] Barchiesi, E., Dell'Isola, F., Laudato, M., Placidi, L., and Seppecher, P.: A 1D continuum model for beams with pantographic microstructure: asymptotic micro-macro identification and numerical results. Advanced Structured Materials, 2018, 87, pp. 43-74.

[27] Boutin, C., Giorgio, I., and Placidi, L.: Linear pantographic sheets: asymptotic micro-macro models identification. Mathematics and Mechanics of Complex Systems, 2017, 5(2), pp. 127-162.

[28] Dell'Isola, F., and Placidi, L.: Variational principles are a powerful tool also for formulating field theories. CISM, 2011, 535, pp. 1-15.

[29] Auffray, N., Dirrenberger, J., and Rosi, G.: A complete description of bi-dimensional anisotropic strain-gradient elasticity. International Journal of Solids and Structures, 2015, 69, pp. 195-206.

[30] Auffray, N., Dell'Isola, F., Eremeyev, V., Madeo, A., Placidi, L., and Rosi, G: Least action principle for second gradient continua and capillary fluids: a Lagrangian approach following Piola's point of view. Advanced Structured Materials, 2014, 38.

[31] dell'Isola, F., Andreaus, U., and Placidi, L.: At the origins and in the vanguard of peridynamics, non-local and higher-gradient continuum mechanics: an underestimated and still topical contribution of Gabrio Piola. Mathematics and Mechanics of Solids, 2015, 20(8), pp. 887-928.

[32] dell'Isola, F., Seppecher, P., and Madeo, A.: Beyond Euler-Cauchy Continua: The structure of contact actions in N-th gradient generalized continua: a generalization of the Cauchy tetrahedron argument. CISM, 2011, 535, pp. 17-106.

[33] dell'Isola, F., and Seppecher, P.: Edge contact forces and quasi-balanced power. Meccanica, 1997, 32(1), pp. 33-52.

[34] dell'Isola, F., and Seppecher, P.: The relationship between edge contact forces, double forces and interstitial working allowed by the principle of virtual power. Comptes rendus de l?Acade?mie des sciences, Serie IIb, 1995, pp. 7.

[35] del Vescovo, D., and Giorgio, I.: Dynamic problems for metamaterials: review of existing models and ideas for further research. International Journal of Engineering Science, 2014, 80, pp. 153-172.

[36] Eugster, S., dell'Isola, F., and Steigmann, D.: Continuum theory for mechanical metamaterials with a cubic lattice substructure. Mathematics and Mechanics of Complex Systems, 2019, 7(1), 75-98.

[37] Abali, B. E., Müller, W. H., and dell'Isola, F.: Theory and computation of higher gradient elasticity theories based on action principles. Archive of Applied Mechanics, 2017, 87(9), pp. 1495-1510.

[38] Seppecher, P., Alibert, J. J., and Isola, F.D.: Linear elastic trusses leading to continua with exotic mechanical interactions. Journal of Physics: Conference Series, 2011, 319(1), pp. 12-18).

[39] Turco, E., dell'Isola, F., Cazzani, A., and Rizzi, N.L.: Hencky-type discrete model for pantographic structures: numerical comparison with second gradient continuum models. Zeitschrift für angewandte Mathematik und Physik, 2016, 67(4), 85, pp. 28.

[40] Placidi, L., Andreaus, U., Della Corte, A., and Lekszycki, T.: Gedanken experiments for the determination of two-dimensional linear second gradient elasticity coefficients. Zeitschrift für angewandte Mathematik und Physik, 2015, 66(6), pp. 3699-3725.

[41] Placidi, L., Andreaus, U., and Giorgio, I.: Identification of two-dimensional pantographic structure via a linear D4 orthotropic second gradient elastic model. Journal of Engineering Mathematics, 2017, 103(1), pp. 1-21.

[42] Placidi, L., Barchiesi, E., and Della Corte, A.: Identification of two-dimensional pantographic structures with a linear d4 orthotropic second gradient elastic model accounting for external bulk double forces. Advanced Structured Materials, 2015, 69, pp. 211-232.

[43] dell'Isola, F., Giorgio, I., Pawlikowski, M., and Rizzi, N.L.: Large deformations of planar extensible beams and pantographic lattices: heuristic homogenization, experimental and numerical examples of equilibrium. Proceedings of the Royal Society A: Mathematical, Physical and Engineering Sciences, 2016, 472(2185).

[44] Yildizdag, M.E., Tran, C. A., Barchiesi, E., Spagnuolo, M., dell'Isola, F., and Hild, F.: A Multi-disciplinary Approach for Mechanical Metamaterial Synthesis: A Hierarchical Modular Multiscale Cellular Structure Paradigm. Advanced Structured Materials, 2019, 100, pp. 485-505.

5 Discussion

The main goal of this work was to establish new experimental set-ups in order to measure out-of-plane movements of (*inter alia* self-manufactured) pantographic sheets with the aim to determine new (higher) material parameters by means of an inverse analysis. Additionally, an adapted higher continuum model from [44] was slightly modified and evaluated with the help of the determined parameters.

In the first publication [1], published as **"Gregor Ganzosch, Francesco dell'Isola, Emilio Turco, Tomasz Lekszycki, and Wolfgang H. Müller: Shearing tests applied to pantographic structures. *Acta Polytechnica CTU Proceedings*, 7:1–6, 2017"**, five differently sized specimen made of polyamide were subjected to shear-like loading while their mechanical deformation behavior was analyzed. It was shown that the variation of the inner parameters on the substructure, *i.e.*, beams and pivots, have a deep impact on the global deformation behavior of the entire metamaterial. By enlarging the width a of the beam and therefore the area moment of inertia which results in a higher bending rigidity of the fibers, the resistance against failure increases. Nevertheless, an upper limit value j between 1.60 mm $\leq j \leq$ 2.25 mm was measured and indicates that some intermediate effects minimize the influence of the higher area moment of inertia. Notice that all investigated samples were able to resist at least shear elongations of about 270% before total failure of the entire metamaterial occurred. Hence, all samples were capable to resist large shear loads with a strong non-linear response without leading to complete failure. Because of the complex substructure, the beams interconnected by the pivots reorganize themselves resulting in a high resilience being able to carry out even higher shear loads after local failures have occurred. These observations are in good agreement with investigations performed on extended PA-samples in [6]. Interestingly, during shearing tests buckling-like out-of-plane deformations with locally movements up to about 19 mm were estimated. Because of lack of measurement devices which are able to determine displacements in the third spatial direction, here not possible with 2D-DIC, this qualitatively observed phenomena could only be estimated and not determined quantitatively.

To overcome these limits, three-dimensional digital image correlation is introduced in the second publication [2], which is published as **"Gregor Ganzosch, Klaus Hoschke, Tomasz Lekszycki, Ivan Giorgio, Emilio Turco, and Wolfgang H. Müller. 3D-measurements of 3D-deformations of pantographic structures. *Technische Mechanik,* 38(3):233–245, 2018"**. This non-contact technique is able

to detect and to measure an entire three-dimensional deformation field on the surface in real time. Indeed, for the first time to the knowledge of the author, the full displacement field of an entire pantographic surface was measured quantitatively during shearing (and torsion tests) applied to PSs made of PA and ALU-H with maximal out-of-plane displacements of 20.31 mm for the PA sample and 23.29 mm for the ALU-H sample. This is in good accordance to the estimated out-of-plane displacement of about 19 mm for the PA sample assessed in the first publication [1]. Furthermore, the presumed non-linear material behavior, which was also measured before in the first publication [1], was confirmed. Indeed, the buckling-like deformation was observed in all experiments and is probably caused by two local mechanisms: First, the geodesic bending deformation of fibers, *i.e.*, bending along the plane tangent to the equivalent deformed surface representing the deformed 3D sample. Second, the bending of fibers out of the plane tangent to the equivalent deformed surface and their twisting. Whether the stiffness to in-plane bending of beams is relatively larger than the one to out-of-plane bending or not, the first or the second aforementioned behavior is observed. Notice that the stiffness of fibers is strongly dependent on their dimensions and therefore on their geometries as well.

In addition to measurements performed on shearing tests, novel 3D-DIC measurements of PSs during torsion tests have been performed as well in this publication. The extraordinary material behavior was also observed in the quasi-static, angle-controlled torsion test, in which a strong non-linear dependence of angle and measured moment was observed. Because of the much stiffer material parameters of the heat-treated aluminum, its maximal torsion load is about seventeen times higher than the one measured for the polyamide sample. Indeed, further investigations of twisted pantographic metamaterials made of PA, ALU and ALU-H in [17] and [52] confirmed the exotic, non-linear mechanical response. Notice that the untreated ALU sample was able to carry 16% higher rotational loads during torsion tests than the heat-treated ALU-H sample [52]. Nevertheless, the ALU sample failed after about one total rotation in contrast to the ALU-H sample, which was able to resist total failure during the whole experiment ending after about 5.7 total rotations [52], see Fig. 25. Heat-treatment of sample ALU-H leads to a ductile metamaterial. Furthermore, this post process reduces the internal stresses caused by the high laser exposure and hence decreases the number of imperfections, *e.g.*, voids, see Fig. 16. This is in contrast to the untreated ALU sample, where a rough profile on the surface indicates an inhomogeneous material deviation, see Fig. 15.

Furthermore, a highly non-linear Poynting effect, including its reversal from positive to negative direction (elongation to compression) during torsion was monitored in [17, 2]. It was observed that for PSs consisting of relatively soft beams but stiff pivots, a standard (positive) Poynting effect dominates resulting in a larger helix angle, which is exemplary shown in Figs. 26(c)-(d). Softer beams bend easily because the relative rotation of stiff pivots is suppressed. In contrast, PSs with stiff beams and soft pivots lead to a shortening of the sample resulting in a negative Poynting effect. Stiffer beams resist bending while the rotation of the pivots is dominating and therefore are increasingly sheared resulting in a smaller helix angle. Interestingly, intermediate cases were observed as well in [17] where the elongation of the entire sample switches to compression. At first the flexural deformation energy of beams dominates while as the twist angle increases, the shear energy of pivots dominates. As a result the positive Poynting effect reduces, then reverses and finally becomes negative. As mentioned before in Subsect. 2.4.2, for this metamaterial the classical Cauchy-Boltzmann continuum model mostly fails and a 2nd gradient continuum model is necessary to describe many of its deformation behaviors [28, 6].

Due to this fact the third publication [3], which was published as **"Emilio Barchiesi, Gregor Ganzosch, Christian Liebold, Luca Placidi, Roman Grygoruk, and Wolfgang H. Müller. Out-of-plane buckling of pantographic fabrics in displacement-controlled shear tests: experimental results and model validation.** ***Continuum Mechanics and Thermodynamics,*** **31(1):33–45, 2019"**, is quite involved. Based on the preliminary work in [25, 7], colleagues from Italy developed an analytical model to investigate the extraordinary behavior by means of a 2D continuum model embedded in a 3D space in [44]. The main challenge in the third publication [3] was to measure and hence to determine the new higher stiffness parameters listed in Eq. (07) and in Table 7 by means of an inverse analysis in order to obtain predictive simulations of the adopted model from [44]. It should also be mentioned that this model can be considered as a kind of extended second gradient continuum model with respect to the classic Kirchhoff-Love plate theory, as the deformed surface can undergo in-plane bending, and additionally out-of-plane bending and twisting is considered.

As seen in the third publication [3], Fig. 12 (out-of-plane displacement / shear displacement diagram), and in [3], Fig. 13 (shear force / shear displacement diagram), measured results and theoretical predictions for the herein investigated PA specimen

are in good agreement. Note that the low horizontal measurement errors in [3], Fig. 12 (out-of-plane displacement / shear displacement diagram), are caused by the recorded picture sequence, *i.e.*, a picture was taken every two seconds, see Subsects. 2.3.1/2.3.2. The high vertical measurement errors in [3], Fig. 12 (out-of-plane displacement / shear displacement diagram), exist due to the relative difference of the two planes defined by the periodically aligned arrays of beams, *i.e.*, different family of fibers. Therefore, it is not clear, wether the plane of fibers in the front or the plane of fibers in the back relative to the camera system is inside the focus and therefore considered in the correlation process. Furthermore, this depends also strongly on two other main points: firstly, on the quality of the intrinsic and extrinsic correlation parameters, *i.e.*, g_i, a_i listed in Eqs. (1)–(3), which have been elaborated during the cumbersome calibration procedure, and secondly, on the quality of the testing set-up, to be more precise on the parallelism of the mounting jaws of the testing device. Because of the offset of the two families of fibers, which results in a symmetry break of the complex system with respect to the lateral plane of the pantographic sheet and is also in good agreement with measurements from [40], a little perturbation was considered at the long edges of the sample (coupling) to avoid buckling in one direction. Small measurement errors in [3], Fig. 13 (force / shear displacement diagram), are due to the calibration noise of the device integrated load cell (vertical error) and the device integrated displacement encoder (horizontal error).

Results of 3D-DIC measurements of five sheared PA-samples with different inner geometries strengthens the assumption that the global deformation behavior of a metamaterial with a pantographic substructure is strongly influenced by the inner parameters on the microscale. Indeed, results also verify non-linear deformation behavior and a very resilient material/structure, which was already shown in the first two publications [1] and [2]. Furthermore, the assumption stated in [2], that the buckling in shearing tests is due to the complex interplay of two different local mechanism phenomena, namely in-plane and out-of-plane bending of fibers, could be proven by means of a theoretical model adapted from [44]. It is able to simulate in-plane, out-of-plane, and twisting of fibers simultaneous. By deploying the determined material parameters in the aforementioned model and comparing the results with the measurement results, the correctness of the assumption could be proofed as seen in [3], Figs. 12/13).

Note that investigations with different inner geometries on the substructure of PSs are quite involved in the first three publications [1, 2, 3]. Nevertheless, the influence of the

outer dimensions, *i.e.*, the length L, see Table 1, Fig. 3, or Fig. 2, respectively, on the deformation behavior has not been taken into account, neither extension tests have been discussed. Moreover, samples made of two different materials, *i.e.*, PA and ALU, which show an inhomogeneous material deviation caused by the manufacturing process as seen in Figs. 13/15, have been considered so far. Due to these reasons the last publication [4], published as the fourth publication **"Gregor Ganzosch, Christina Völlmecke, Emilio Barchiesi, and Wolfgang H. Müller. The making and testing of FDM and SLA printed pantographic sheets. *Elasticity and Anelasticity,* Moscow State Univ. Publ., 57—66, 2021"**, was added to this work. Shorter samples made of PLA and EPO have been manufactured by means of two different 3D-printers using FDM and SLA with the aim to test these samples in quasi-static extension and shearing tests, validated by 2D-DIC.

Results of shear experiments performed on PLA samples indicate a strong resilient deformation behavior and hence are in good agreement with the quasi-static investigations from [40]. But this is in total contrast to the sheared ER sample, in which the total structure broke right after a first failure, see [4], Fig. 12. The stiff material property of the cured epoxy hardener resin leads to a brittle deformation characteristic, which was also observed on the microstructure of another ER sample, see Fig. 9. Nevertheless, as stated in [1, 3], a variation of the inner parameters on the substructure has a huge influence on the global deformation behavior of the entire metamaterial: PLA and ER specimens consisting of smaller pivot heights ($h = 1$ mm) showed a much stiffer deformation behavior against shear and extension load than the specimens with larger pivot heights ($h = 3$ mm), see [4], Fig. 7, and [4], Fig. 11, respectively. This can be explained by the flexibility of the pivots. Stiffer beams resist bending while the pivots are torqued and also bended and therefore are sheared resulting in a larger (elastic) global deformation of the specimen.

It should be mentioned that out-of-plane buckling was observed during all shearing tests applied to ER and PLA samples due to the fact that the imperfect pivots, *i.e.*, pivots which can not be treated as joints/hinges, dissipate energy while rotating [55]. This was also observed for PA, ALU, and ALU-HT samples in [1, 2, 3]. To overcome these limits, perfect pivots, which can be treated as joints, have been firstly introduced by the Polish and Italian Colleagues and have been further taken into account in [55]. Nevertheless, in order to avoid floppy modes caused by the perfect pivots (almost frictionless), so-called Bi-Pantographic beams [56, 57] and Bi-Pantographic Structures (Bi-PS), which

are shown in Fig. 31(a) during a point-force test, have been manufactured and tested as well [53, 58, 57]. Still, out-of-plane movements have been measured as shown in Fig. 31(b) during shearing tests and are still topic of an ongoing research project.

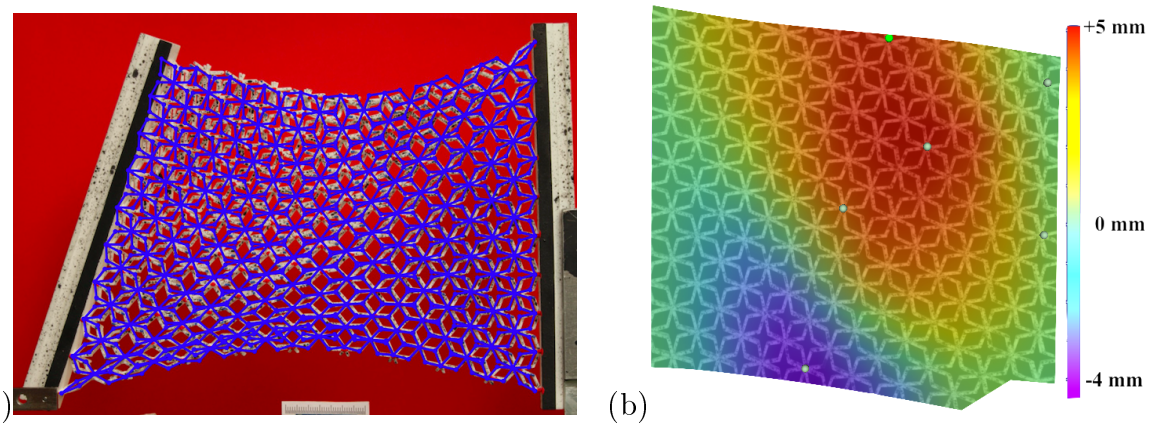

Figure 31: (a) Overlay of a Bi-Pantographic Structure (Bi-PS) and a discrete calculated deformation grid during point-force experiment from [58]; (b) Overlay of a Bi-PS made of PA and its out-of-plane movements during a shearing test.

As examined in [1, 2, 3] for ALU and PA samples, PLA and ER samples show an almost linear deformation behavior in shearing tests for small deformations (shear strain smaller than 3%). Indeed, a non-linear deformation behavior could only be recognized for one ER sample starting at an elongation of about 2%. Note, all PLA and ER samples with larger pivot heights, which were tested in extension experiments, show an almost linear elastic deformation behavior for small deformations (less than 3% axial elongation), see [4], Fig. 7. Due to this reason, the results of a classic FEM calculation based on linear elasticity are in good agreement with the experimental results obtained from extension tests, see Table 6 and [4], Fig. 10. Note that material parameters for the input in FEM have been determined separately by means of standardized dog bone specimens validated by a laser extensometer following Eq. 6 in order to represent the effect of the slicing strategy and hence the print direction on the deformation behavior more accurate as also described in more detail in [41, 42, 43].

It should also be mentioned that the length-shortening of the PLA and ER samples, *i.e.*, $L/l = 2$, see Fig. 2, are reflected in smaller shear elongations until first rupture. In contrast to PA specimens with a length-to-height ratio of $L/l = 3$ investigated in [1, 2, 3, 52], where maximal shear strains above 100% could be reached easily, the ER sample was able to resist about 55% of shear elongation and the PLA sample was able

to resist about 48% until a first rupture in shearing tests occurred. This may be due to the fact that the boundary conditions changed. For the shorter samples, the declining number of "free-hanging" beams decreases the capability to deform in an elastic way, because the number of fixed beams increases relatively compared to the total number of beams. Of course, the brittle material behavior of ER, as shown in Fig. 13, and the printing directions of additively FDM manufactured PLA specimens, see [43] and Fig. 5, can not be neglected with regards to the much smaller shear elongations of ER and PLA specimens.

6 Conclusion and outlook

Metamaterials with a pantographic substructure have been designed, manufactured, tested, modeled and evaluated. A parametrized CAD model was developed and used to manufacture differently sized PSs made of at least four different materials, *i.e.*, PLA, EPO, PA, and ALU (ALU-HT), by means of additive manufacturing techniques, *i.e.*, fused deposition modeling, stereolithography, selective laser melting, and direct metal laser sintering. Samples have been tested in extension, shearing, and torsion tests and results have been evaluated by DIC. Furthermore, out-of-plane movements have been determined quantitatively by means of 3D-DIC. Based on these results, new (higher) material parameters have been determined by means of an inverse analysis. These material parameters have been used to evaluate a classical and a 2nd order gradient model.

Large, non-linear deformations and highly resilient material behaviors have been measured in PSs and indicate a wide range of their technical applications in the field of engineering: their lightweight and their capability to deform in a high (elastic) range makes PSs very attractive for lightweight industries, *e.g.*, in air craft industries and in the automotive sector, or to serve as stents or bone replacements in the field of medical devices. Furthermore, the combination of the resilient deformation behavior, *i.e.*, the capability to resist outer external loads without leading to total failure, and the capability to deform in a large (elastic) regime could also be exploited in the security industry, *e.g.*, as an early warning mechanism in a critical component. Of course, the two-dimensional pantographic sheet should be expanded in a third dimension, *e.g.*, a sandwich structure could serve in a damper system or a pantograph formed to a cylinder could imitate a vein or a blood vessel as an artificial device. Other shapes of the fabrics and different geometries or designs, *e.g.,* parabolic structures shown in Fig. 32(a), could be pictured in order to explore new areas of applications of higher gradient materials: first investigations on parabolic structures indicate a resilient and predictable deformation behavior, see Fig. 32(b), and could be used as an impact damper in a security shield for example.

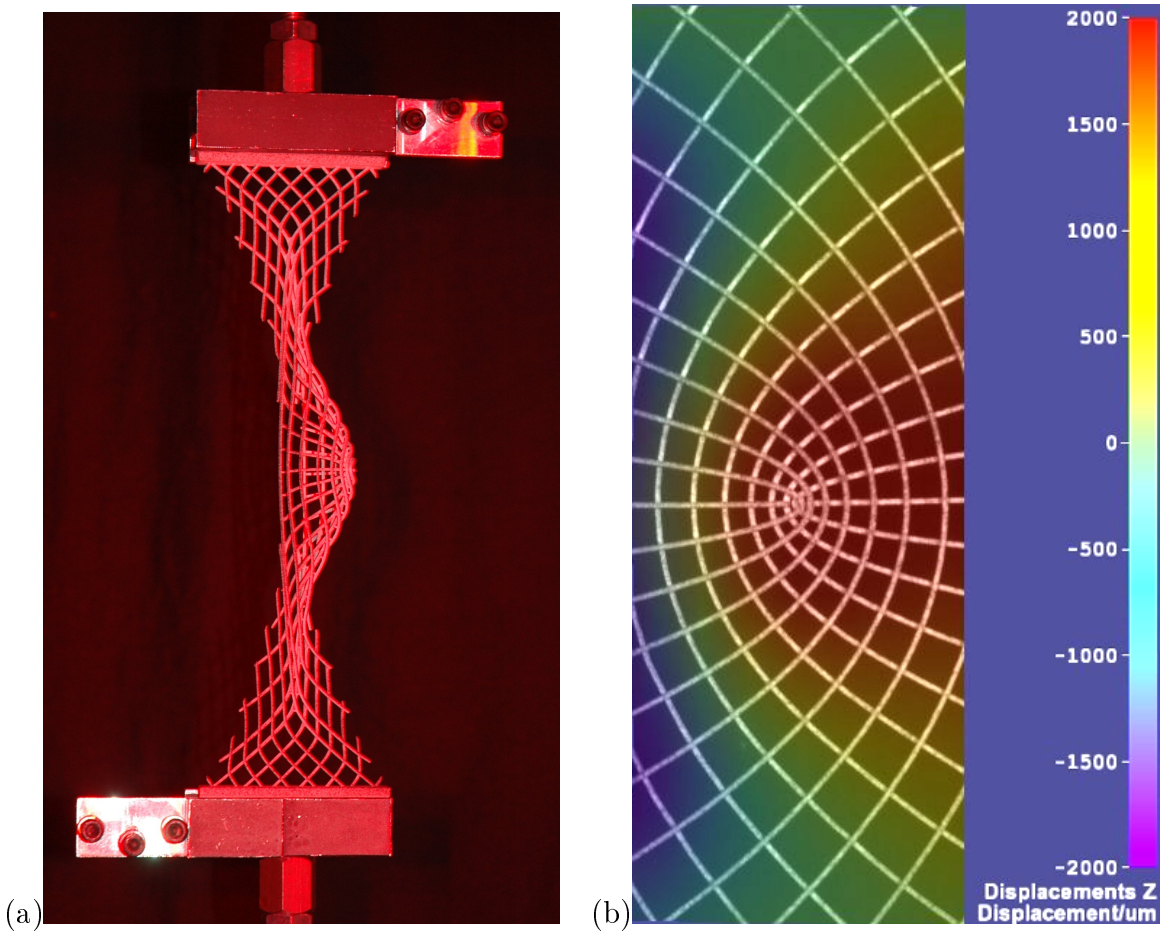

Figure 32: (a) Metamaterial with a parabolic (sub)structure made of PA during extension test; (b) 3D-DIC measurement of the deformation field of a parabolic structure.

Another area of application could arise from auxetic, pantographic materials. One may imagine that such an mechanically controlled mechanism could be very interesting in the field of fluid mechanics, *e.g.*, to serve as a valve or in general as a kind of suspension that is able to lift pipes on construction sites. Furthermore, a classification of all tested metamaterials with a pantographic substructure and a comparison with the so-called "Ashby-Charts" [45, 46, 47] could introduce and then improve the acceptance of PSs in the field of industrial applications.

As mentioned before, DIC was quiet involved and was able to provide exceptional results, which could be used to evaluate simulation models. Nevertheless, DIC has the restriction that the calculated strains are limited to the outer surface. Indeed, to measure directly the deformation of an inner geometry like a pivot, digital volume

correlation should be considered in further investigations. One advantage is that the simulation models could be evaluated based on 3D imaging data, *e.g.*, μCT, with a better quality. Nevertheless, imaging is not instantaneous and hence real time observations are still best identified by optical DIC. In addition, the calibration procedure of the cameras should be developed further in order to increase the measurement's quality and to find the right balance between illumination settings and contrast of the speckle pattern. Another source of error is the manufacturing process of the specimen. Process parameters of all printing machines should be optimized in a way that more homogeneous specimens could be printed, see [41, 42, 43].

Figure 33: PSs and standardized dog-bone specimens including support structures made from a ceramic epoxid resin right after manufacturing by means of SLA at the Institute of Mechanics, Technische Universität Berlin, Germany.

Depending on the engineering application, a brittle material property may be of great interest. In order to switch from a ductile behavior to a more brittle material behavior for a metamaterial with a pantographic substructure, other raw materials, *e.g.*, glass, porcelain, or ceramics, see prototypes from pre-investigations in Fig. 33, should be investigated further. Moreover, in order to relieve the environment, preference should be given to reusable materials that can be recycled in an environmentally compatible

way, *e.g.*, by making use of filaments made from wood in FDM. Both projects are currently parts of ongoing research studies.

Another future development concerns the ability to describe possible interactions between beams in the cases in which these come into contact (see [59, 60, 17]). PSs, which behave like a 2nd gradient material, can exhibit some sort of phase transition behavior on the border regions of the beams behaving like a first gradient material [61, 62, 63]. Furthermore, damage evolution and plasticity should also be taken into account for modeling of PSs in future research as proposed in [64] and firstly evaluated in [38]. As seen in [18, 11, 65, 58, 57] and described for other materials in [10], results obtained from higher gradient simulations will be compared with the real experiments performed in this work and investigated further.

Note that higher modes of out-of-plane movements have been measured in shearing tests, see Fig. 34. This exceptional deformation behavior is an ongoing field of research and will be investigated further with the colleagues from Italy. Furthermore, the exotic deformation behaviors of Bi-PSs, which have been introduced in Figs. 31(a)/(b), and their discrete modeling, see [58], should also be carefully studied in the future in order to find technical applications for Bi-PS.

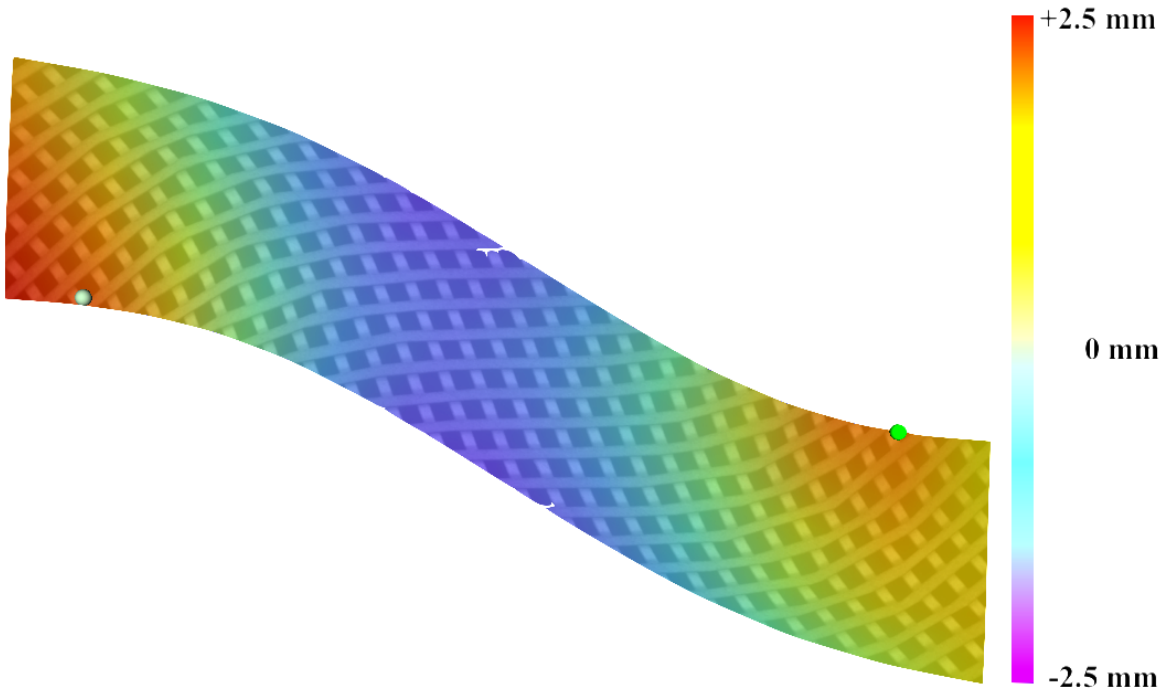

Figure 34: A PS made of PA showing an 2nd order mode of out-of-plane movements during quasi-static shearing tests.

References

[1] Gregor Ganzosch, Francesco dell'Isola, Emilio Turco, Tomasz. Lekszycki, and Wolfgang H. Müller. Shearing tests applied to pantographic structures. *Acta Polytechnica CTU Proceedings*, 7:1–6, 2017.

[2] Gregor Ganzosch, Klaus Hoschke, Tomasz Lekszycki, Ivan Giorgio, Emilio Turco, and Wolfgang H. Müller. 3d-measurements of 3d-deformations of pantographic structures. *Technische Mechanik*, 38(3):233–245, 2018.

[3] Emilio Barchiesi, Gregor Ganzosch, Christian Liebold, Luca Placidi, Roman Grygoruk, and Wolfgang H. Müller. Out-of-plane buckling of pantographic fabrics in displacement-controlled shear tests: experimental results and model validation. *Continuum Mechanics and Thermodynamics*, 31(1):33–45, 2019.

[4] Gregor Ganzosch, Christina Völlmecke, Emilio Barchiesi, and Wolfgang H. Müller. The making and testing of fdm and sla printed pantographic sheets. In *Elasticity and Anelasticity*, pages 57–66. Moscow State Univ. Publ., 2021.

[5] Francesco dell'Isola, David Steigmann, and Alessandro Della Corte. Synthesis of fibrous complex structures: designing microstructure to deliver targeted macroscale response. *Applied Mechanics Reviews*, 67(6):21–pages, 2016.

[6] Francesco dell'Isola, Tomasz Lekszycki, Marek Pawlikowski, Roman Grygoruk, and Leopoldo Greco. Designing a light fabric metamaterial being highly macroscopically tough under directional extension: First experimental evidence. *Zeitschrift für angewandte Mathematik und Physik*, 66(6):3473–3498, 2015.

[7] Luca Placidi, Ugo Andreaus, Alessandro Della Corte, and Tomasz Lekszycki. Gedanken experiments for the determination of two-dimensional linear second gradient elasticity coefficients. *Zeitschrift für angewandte Mathematik und Physik*, 66(6):3699–3725, 2015.

[8] Emilio Turco, Ivan Giorgio, Anil Misra, and Francesco dell'Isola. King post truss as a motif for internal structure of (meta)material with controlled elastic properties. *Royal Society Open Science*, 4(10):171153, 2017.

[9] Francesco dell'Isola, Emilio Turco, Anil Misra, Zacharias Vangelatos, Costas Grigoropoulos, Vasileia Melissinaki, and Maria Farsari. Force–displacement relationship in micro-metric pantographs: Experiments and numerical simulations. *Comptes Rendus Mécanique*, 347(5):397–405, 2019.

[10] Gregor Ganzosch and Wolfgang H. Müller. Experimental techniques applied to generalized continuum theories-a state-of-the-art report. In *Proceedings of the XLIV Summer School-Conference, Advanced Problems in Mechanics*, volume 44, pages 149–161, 2016.

[11] Emilio Barchiesi, Mario Spagnuolo, and Luca Placidi. Mechanical metamaterials: a state of the art. *Mathematics and Mechanics of Solids*, 24(1):212–234, 2018.

[12] Francesco dell'Isola, Pierre Seppecher, Mario Spagnuolo, Emilio Barchiesi, François Hild, Tomasz Lekszycki, Ivan Giorgio, Luca Placidi, Ugo Andreaus, Massimo Cuomo, et al. Advances in pantographic structures: design, manufacturing, models, experiments and image analyses. *Continuum Mechanics and Thermodynamics*, 31(4):1231–1282, 2019.

[13] Francesco dell'Isola, Pierre Seppecher, Jean Jacques Alibert, Tomasz Lekszycki, Roman Grygoruk, Marek Pawlikowski, David Steigmann, Ivan Giorgio, Ugo Andreaus, Emilio Turco, et al. Pantographic metamaterials: an example of mathematically driven design and of its technological challenges. *Continuum Mechanics and Thermodynamics*, 31(4):851–884, 2019.

[14] Francesco dell'Isola, Ivan Giorgio, Marek Pawlikowski, and Nicola Luigi Rizzi. Large deformations of planar extensible beams and pantographic lattices: heuristic homogenization, experimental and numerical examples of equilibrium. *Proceedings of the Royal Society A: Mathematical, Physical and Engineering Sciences*, 472(2185), 2016.

[15] Francesco dell'Isola, Alessandro Della Corte, Leopoldo Greco, and Angelo Luongo. Plane bias extension test for a continuum with two inextensible families of fibers: A variational treatment with lagrange multipliers and a perturbation solution. *International Journal of Solids and Structures*, 81:1–12, 2016.

[16] Albrecht Bertram and Rainer Glüge. Gradient materials with internal constraints. *Mathematics and Mechanics of Complex Systems*, 4(1):1–15, 2016.

[17] Anil Misra, Tomasz Lekszycki, Ivan Giorgio, Gregor Ganzosch, Wolfgang H. Müller, and Francesco dell'Isola. Pantographic metamaterials show atypical poynting effect reversal. *Mechanics Research Communications*, 89:6–10, 2018.

[18] Hua Yang, Gregor Ganzosch, Ivan Giorgio, and Bilen E. Abali. Material characterization and computations of a polymeric metamaterial with a pantographic substructure. *Zeitschrift für angewandte Mathematik und Physik*, 69(4):105, 2018.

[19] Gregor Ganzosch, Melanie Todt, Anton Köllner, and Christina Völlmecke. Experimental investigations on pre-stressed stayed columns on smaller length scales. *Proceedings of the Eight International Conference on Thin-Walled Structures*, pages 24–27, July 2018.

[20] Ciprian Borcea and Ileana Streinu. Geometric auxetics. *Proceedings of the Royal Society A: Mathematical, Physical and Engineering Sciences*, 471(2184):20150033, 2015.

[21] Hyeonho Cho, Dongsik Seo, and Do-Nyun Kim. *Mechanics of Auxetic Materials*, pages 733–757. Springer Singapore, Singapore, 2019.

[22] Pierre Seppecher, Jean-Jacques Alibert, and Francesco dell'Isola. Linear elastic trusses leading to continua with exotic mechanical interactions. *Journal of Physics: Conference Series*, 319(1):012018, 2011.

[23] Francesco dell'Isola and Luca Placidi. *Variational principles are a powerful tool also for formulating field theories*, pages 1–15. Springer Vienna, Vienna, 2011.

[24] Francesco dell'Isola and David Steigmann. A two-dimensional gradient-elasticity theory for woven fabrics. *Journal of Elasticity*, 118(1):113–125, 2015.

[25] Francesco dell'Isola, Alessandro Della Corte, Ivan Giorgio, and Daria Scerrato. Pantographic 2D sheets: Discussion of some numerical investigations and potential applications. *International Journal of Non-Linear Mechanics*, 80:200–208, 2016.

[26] Eugene Cosserat and François Cosserat. Sur la théorie de l'élasticité. premier mémoire. In *Annales de la Faculté des sciences de Toulouse: Mathématiques*, volume 10, pages I1–I116. Gauthier-Villars et Fils, Imprimeurs-Libraires, 1896.

[27] Eugene Cosserat, François Cosserat, et al. *Théorie des corps déformables*. A. Hermann et fils, 1909.

[28] Catherine Pideri and Pierre Seppecher. A second gradient material resulting from the homogenization of an heterogeneous linear elastic medium. *Continuum Mechanics and Thermodynamics*, 9(5):241–257, 1997.

[29] Jean-Jacques Alibert, Pierre Seppecher, and Francesco dell'Isola. Truss modular beams with deformation energy depending on higher displacement gradients. *Mathematics and Mechanics of Solids*, 8(1):51–73, 2003.

[30] Francesco dell'Isola, Ugo Andreaus, and Luca Placidi. At the origins and in the vanguard of peridynamics, non-local and higher-gradient continuum mechanics:

An underestimated and still topical contribution of Gabrio Piola. *Mathematics and Mechanics of Solids*, 20(8):887–928, 2015.

[31] Francesco dell'Isola, Pierre Seppecher, and Alessandro Della Corte. The postulations á la d'alembert and á la cauchy for higher gradient continuum theories are equivalent: a review of existing results. In *Proceedings of the Royal Society A: Mathematical, Physical and Engineering Sciences*, volume 471, page 20150415. The Royal Society, 2015.

[32] Francesco dell'Isola, Alessandro Della Corte, and Ivan Giorgio. Higher-gradient continua: The legacy of piola, mindlin, sedov and toupin and some future research perspectives. *Mathematics and Mechanics of Solids*, 22(4):852–872, 2017.

[33] David C.C. Lam, Fan Yang, Arthur C.M. Chong, Jun Wang, and Pin Tong. Experiments and theory in strain gradient elasticity. *Journal of the Mechanics and Physics of Solids*, 51(8):1477–1508, 2003.

[34] Roderic S. Lakes. Experimental microelasticity of two porous solids. *International Journal of Solids and Structures*, 22(1):55–63, 1986.

[35] Christian Liebold and Wolfgang H. Müller. Measuring material coefficients of higher gradient elasticity by using afm techniques and raman-spectroscopy. In Holm Altenbach, Samuel Forest, and Anton Krivtsov, editors, *Generalized Continua as Models for Materials: with Multi-scale Effects or Under Multi-field Actions*, pages 255–271. Springer Berlin Heidelberg, Berlin, Heidelberg, 2013.

[36] Roderic S. Lakes and Walter J. Drugan. Bending of a cosserat elastic bar of square cross section: Theory and experiment. *Journal of Applied Mechanics*, 82(9), 2015.

[37] Christian Liebold. *Größeneffekt in der Elastizität*. PhD thesis, Technische Universität Berlin, 2015.

[38] Emilio Turco, Francesco dell'Isola, Nicola L. Rizzi, Roman Grygoruk, Wolfgang H. Müller, and Christian Liebold. Fiber rupture in sheared planar pantographic sheets: Numerical and experimental evidence. *Mechanics Research Communications*, 76:86–90, 2016.

[39] Christian Liebold and Wolfgang H. Müller. Applications of higher-order continua to size effects in bending: Theory and recent experimental results. In Holm Altenbach and Samuel Forest, editors, *Generalized Continua as Models for Classical and Advanced Materials*, pages 237–260. Springer International Publishing, Cham, 2016.

[40] Arion Juritza, Hua Yang, and Gregor Ganzosch. Qualitative investigations of experiments performed on 3d-fdm-printed pantographic structures made out of pla. In Bilen Emek Abali, Holm Altenbach, Francesco dell'Isola, Victor A. Eremeyev, and Andreas Öchsner, editors, *New Achievements in Continuum Mechanics and Thermodynamics: A Tribute to Wolfgang H. Müller*, pages 197–209. Springer International Publishing, Cham, 2019.

[41] Josef Kiendl and Chao Gao. Controlling toughness and strength of fdm 3d-printed pla components through the raster layup. *Composites Part B: Engineering*, 180:107562, 2020.

[42] Arda Özen, Dietmar W. Auhl, Christina Völlmecke, Josef Kiendl, and Bilen E. Abali. Optimization of manufacturing parameters and tensile specimen geometry for fused deposition modeling (fdm) 3d-printed petg. *Materials*, 14(10), 2021.

[43] Arda Özen, Gregor Ganzosch, Emilio Barchiesi, Dietmar W. Auhl, and Wolfgang H. Müller. Investigation of deformation behavior of petg-fdm-printed metamaterials with pantographic substructures based on different slicing strategies. *Composites and Advanced Materials*, 30:26349833211016477, 2021.

[44] Ivan Giorgio, Nicola L. Rizzi, and Emilio Turco. Continuum modelling of pantographic sheets for out-of-plane bifurcation and vibrational analysis. *Proceedings of the Royal Society A: Mathematical, Physical and Engineering Sciences*, 473(2207):20170636, 2017.

[45] Lorna J. Gibson and Michael F. Ashby. *Cellular solids: structure and properties.* Cambridge University Press, 2 edition, 1999.

[46] Michael F. Ashby and David Cebon. Materials selection in mechanical design. *Le Journal de Physique IV*, 3(C7):C7–1, 1993.

[47] Hugh R. Shercliff and Michael F. Ashby. Elastic structures in design. In *Reference Module in Materials Science and Materials Engineering.* Elsevier, 2016.

[48] François Hild and Stephane Roux. Digital image correlation: from displacement measurement to identification of elastic properties - a review. *Strain*, 42(2):69–80, 2006.

[49] Gregor Ganzosch. Small scale bone deformation: A study of compression testing by simulation, validated by digital image correlation. mathesis, Rhein-Westfälische Technische Hochschule Aachen, Institut für Angewandte Medizintechnik, Lehr- und Forschungsgebiet Kardiovaskuläre Technik, RWTH Aachen, August 2015.

[50] Claudia Fleck, Martin Burke, Gregor Ganzosch, Cecilia Müller, John D. Currey, and Paul Zaslansky. Breaking crown dentine in whole teeth: 3d observations of prevalent fracture patterns following overload. *Bone*, 132:115178, 2020.

[51] Michael A. Sutton, Jean J. Orteu, and Hubert Schreier. *Image Correlation for Shape, Motion and Deformation Measurements*, volume 1. Springer, Boston, MA, 1 edition, 2009.

[52] Gregor Ganzosch, Emilio Barchiesi, Rafal Drobnicki, Aron Pfaff, and Wolfgang H Müller. Experimental investigations of 3d-deformations in additively manufactured pantographic structures. In *International Summer School-Conference, Advanced Problems in Mechanics*, pages 101–114. Springer, 2019.

[53] Wolfgang Müller and Gregor Ganzosch. Making, testing, and modeling of pantographic structures. *Mechanics of Materials: Towards Predictive Methods for Kinetics in Plasticity, Fracture, and Damage - Oberwolfach Workshop Reports*, 2011-74:45–48, 2020.

[54] Ivan Giorgio, Nicola L. Rizzi, Ugo Andreaus, and David J. Steigmann. A two-dimensional continuum model of pantographic sheets moving in a 3d space and accounting for the offset and relative rotations of the fibers. *Mathematics and Mechanics of Complex Systems*, 7(4):311–325, 2019.

[55] Ivan Giorgio, Valerio Varano, Francesco dell'Isola, and Nicola L. Rizzi. Two layers pantographs: A 2d continuum model accounting for the beams' offset and relative rotations as averages in so(3) lie groups. *International Journal of Solids and Structures*, 216:43–58, 2021.

[56] Emilio Barchiesi, Francesco dell'Isola, François Hild, and Pierre Seppecher. Two-dimensional continua capable of large elastic extension in two independent directions: Asymptotic homogenization, numerical simulations and experimental evidence. *Mechanics Research Communications*, 103:103466, 2020.

[57] Emilio Barchiesi, Francesco dell'Isola, and François Hild. On the validation of homogenized modeling for bi-pantographic metamaterials via digital image correlation. *International Journal of Solids and Structures*, 208:49–62, 2021.

[58] Emil Barchiesi, Jonas Harsch, Gregor Ganzosch, and Simon R. Eugster. Discrete versus homogenized continuum modeling in finite deformation bias extension test of bi-pantographic fabrics. *Continuum Mechanics and Thermodynamics*, pages 01–14, 2020.

[59] Anil Misra and Shiping Huang. Micromechanical stress–displacement model for rough interfaces: Effect of asperity contact orientation on closure and shear behavior. *International Journal of Solids and Structures*, 49(1):111–120, 2012.

[60] Ugo Andreaus, Paolo Baragatti, and Luca Placidi. Experimental and numerical investigations of the responses of a cantilever beam possibly contacting a deformable and dissipative obstacle under harmonic excitation. *International Journal of Non-Linear Mechanics*, 80:96–106, 2016.

[61] Anna De Masi, Nicolas Dirr, and Errico Presutti. Interface instability under forced displacements. In *Annales Henri Poincaré*, volume 7, pages 471–511. Springer, 2006.

[62] Anna De Masi, Errico Presutti, and Dimitrios Tsagkarogiannis. Fourier law, phase transitions and the stationary stefan problem. *Archive for rational mechanics and analysis*, 201(2):681–725, 2011.

[63] George Chatzigeorgiou, Ali Javili, and Paul Steinmann. Multiscale modelling for composites with energetic interfaces at the micro-or nanoscale. *Mathematics and Mechanics of Solids*, 20(9):1130–1145, 2015.

[64] Luca Placidi, Emilio Barchiesi, Emilio Turco, and Nicola Luigi Rizzi. A review on 2D models for the description of pantographic fabrics. *Zeitschrift für angewandte Mathematik und Physik*, 67(5):121, 2016.

[65] Hua Yang and Wolfgang H. Müller. Computation and experimental comparison of the deformation behavior of pantographic structures with different micro-geometry under shear and torsion. *Journal of Theoretical and Applied Mechanics*, 57(2):421–434, 2019.